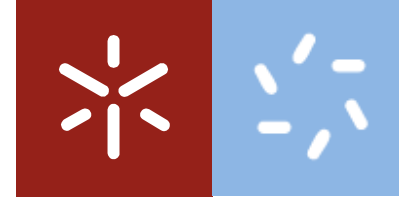




Search for  $t\bar{Z}$  production via Flavour Changing Neutral Currents  
with the ATLAS experiment at the LHC

Ana Paula Pereira Peixoto

Uminho | 2016



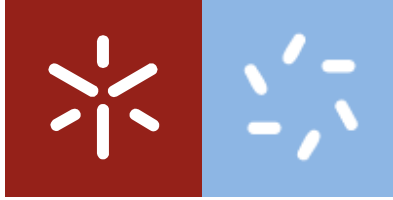
**Universidade do Minho**  
Escola de Ciências

Ana Paula Pereira Peixoto

**Search for  $t\bar{Z}$  production via Flavour Changing  
Neutral Currents with the ATLAS experiment  
at the LHC**

Agosto de 2016





**Universidade do Minho**

Escola de Ciências

Ana Paula Pereira Peixoto

**Search for  $t\bar{Z}$  production via Flavour Changing  
Neutral Currents with the ATLAS experiment  
at the LHC**

Dissertação de Mestrado  
Mestrado em Física - Física Aplicada

Trabalho efetuado sob a orientação do  
**Professor Doutor Nuno Filipe da Silva Fernandes de Castro**

## DECLARAÇÃO

Nome: Ana Paula Pereira Peixoto

E-mail: ana.paula.pereira.peixoto@cern.ch

Telefone: +351969233066

Número de Cartão de Cidadão: 13630865

Título da Tese: Search for  $tZ$  production via Flavour Changing Neutral Currents with the ATLAS experiment at the LHC

Orientador: Doutor Nuno Filipe da Silva Fernandes de Castro

Ano de Conclusão: 2016

Designação do Mestrado: Mestrado em Física Aplicada

É AUTORIZADA A REPRODUÇÃO INTEGRAL DESTA TESE APENAS PARA EFEITOS DE INVESTIGAÇÃO, MEDIANTE DECLARAÇÃO ESCRITA DO INTERESSADO, QUE A TAL SE COMPROMETE;

Universidade do Minho, 29/08/2016

Assinatura:

Ana Paula Pereira Peixoto

**Search for  $tZ$  production via Flavour Changing  
Neutral Currents with the ATLAS experiment  
at the LHC**

**Tese de Mestrado**  
Mestrado em Física - Física Aplicada

Trabalho efectuado sob orientação do  
**Professor Doutor Nuno Filipe da Silva Fernandes de Castro**

Agosto de 2016



# Acknowledgments

This thesis would not be possible without the support of many people. I would like to gratefully acknowledge all of them, in particular the people that supervised my work, those with whom I have worked and those who shared their knowledge with me.

First of all, I would like to express my gratitude to Dr. Nuno Castro for many reasons but more importantly for being a very supportive and, at same time, exigent advisor. Thanks for all you taught me and for the opportunities you gave me.

I also have to thank the Humboldt University (Berlin, Germany) for letting me use their analysis code as well as the cluster to run the analysis presented in this thesis. A special thanks to the Humboldt University group involved in this work composed by Oliver Kind, Thomas Lohse, Sebastian Mergelmeyer and Soren Stamm. They made possible a big part of the work presented here through their expert advices and their support from the first minute of our collaboration. I would like to also thank for their hospitality during my stay in Berlin. I have to acknowledge, in particular, Oliver Kind and Sebastian Mergelmeyer for always being available to help me and for everything I learned with them.

I thank the LIP-Minho team, specially my close colleagues Juan Pedro Araque, Tiago Vale and José Correia for all the help they gave me and for the moments we spent during the last year.

I would like to thank the whole LIP team for their support with a special thanks to the Portuguese ATLAS group. I also have to thank all the people in the Single Top subgroup in ATLAS for all the important advices to the development of this

analysis.

A special word of gratitude goes to my Physics and Chemistry teacher Sónia Torres for introducing me to the physics world and for made me believe in my dream of being a physicist.

The most important thanks go to all my family specially to my mother Manuela and my father Carlos for all their patience and emotional support. Thanks for the motivation and love you give me every day. Finally, I want to thank Tiago who always understands and helps me no matter what. Thank you for being always by my side.

I thank LIP (Laboratório de Instrumentação e Física Experimental de Partículas), FCT/MEC (Fundação Ciência e Tecnologia / Ministério da Educação e da Ciência), FEDER (Fundo Europeu de Desenvolvimento Regional) for funding my activities this past year, as established by the partnership PT2020 partnership with COMPETE2020 (Autoridade de Gestão do Programa Operacional Competitividade e Internacionalização), by providing me with a research scholarship (Reference LIP/BI-26/2015).





# Resumo

A presente dissertação tem como objectivo a pesquisa da produção de eventos  $tZ$  através de processos de mudança de sabor por correntes neutras recorrendo a uma análise de dados colectados pelo detector ATLAS do Large Hadron Collider localizado no CERN. Os processos de mudança de sabor por correntes neutras são muito raros no Modelo Padrão da Física de Partículas, sendo ausentes a *tree-level* e extremamente suprimidos a *loop-level*. No entanto, estes processos têm uma maior probabilidade de ocorrer em vários modelos para além do Modelo Padrão.

Neste trabalho é estudada a produção de um quark top e de um bóson  $Z$  através de processos de mudança de sabor por correntes neutras numa topologia trileptónica. O estado final desta pesquisa consiste num par de leptões de carga oposta e sabor idêntico com uma massa compatível com o decaimento de um bóson  $Z$ , um leptão carregado em conjunto com um leptão neutro provenientes do decaimento de um quark top e finalmente um jacto proveniente de um quark bottom (*b-tagged jet*). Os dados analisados, relativos a colisões próton-próton a uma energia de centro de massa de  $\sqrt{s} = 13$  TeV, foram obtidos no período de Julho a Novembro de 2015 correspondendo a uma luminosidade integrada de  $3.21 \text{ fb}^{-1}$ .

Um estudo complementar de possíveis variáveis discriminantes é apresentado. Através deste estudo, são obtidos limites superiores esperados com um nível de confiança de 95% na secção eficaz de produção deste processo. Estes limites são interpretados em termos do acoplamento  $tZq$  e da fracção de decaimento  $t \rightarrow qZ$ .



# Abstract

The subject of the present dissertation is the search for  $tZ$  event production by Flavour Changing Neutral Currents (FCNC) through the analysis of data collected by the ATLAS detector of the Large Hadron Collider located in CERN. The FCNC processes are very rare in the Standard Model of Particle Physics since they are not allowed at tree-level and extremely suppressed at loop-level. However, these processes have a higher probability to occur in several models beyond the Standard Model.

In this thesis, a search for the production of a top quark and a boson  $Z$  via FCNC in a trileptonic topology is discussed. The final state of the  $tZ$  production consists in a pair of leptons with opposite sign and same flavour having a mass compatible with the decay of a  $Z$  boson, a charged lepton and a neutral lepton classified as coming from the decay of a top quark and finally a jet coming from a bottom quark ( $b$ -tagged jet). The analyzed data coming from proton-proton collisions at the centre-of-mass energy of  $\sqrt{s} = 13$  TeV was collected in the data-taking period between July and November of 2015 corresponding to an integrated luminosity of  $3.21 \text{ fb}^{-1}$ .

A complementary study of possible discriminant variables is presented. Through this study, expected upper limits at 95% confidence level on the cross-section of  $tZ$  production via FCNC were obtained. An interpretation of these limits in terms of branching ratios for  $t \rightarrow qZ$  and the  $tZq$  coupling is also presented.



# Contents

<b>1</b>	<b>Introduction</b>	<b>1</b>
<b>2</b>	<b>The Standard Model of particle physics and beyond</b>	<b>3</b>
2.1	The Standard Model of particle physics . . . . .	3
2.1.1	Quantum electrodynamics . . . . .	6
2.1.2	Quantum chromodynamics . . . . .	7
2.1.3	Electroweak theory . . . . .	9
2.1.4	The Brout-Englert-Higgs mechanism . . . . .	10
2.2	Top quark physics . . . . .	13
2.3	Top quark FCNC interactions . . . . .	15
<b>3</b>	<b>Experimental Setup</b>	<b>19</b>
3.1	CERN . . . . .	19
3.2	The Large Hadron Collider . . . . .	20
3.3	The ATLAS detector . . . . .	22
3.3.1	Inner detector . . . . .	23
3.3.2	Calorimeters . . . . .	25
3.3.3	Muon spectrometer . . . . .	26
3.3.4	Magnet system . . . . .	28
3.3.5	Trigger and data acquisition system . . . . .	28
3.3.6	Worldwide LHC Computer GRID . . . . .	29
<b>4</b>	<b>Event analysis</b>	<b>33</b>
4.1	Data sample and triggers . . . . .	33

4.2	Objects definition . . . . .	34
4.3	Analysis strategy . . . . .	37
4.4	Signal modeling . . . . .	40
4.5	Background modeling . . . . .	40
4.6	Signal region definition . . . . .	42
4.7	Comparison between data and prediction . . . . .	46
4.7.1	Validation regions . . . . .	46
4.8	Systematic uncertainties . . . . .	61
4.9	Discriminant variables . . . . .	62
<b>5</b>	<b>Limits</b>	<b>71</b>
5.1	The $CL_s$ method . . . . .	71
5.2	Limits on the $tZ$ production . . . . .	73
<b>6</b>	<b>Conclusions</b>	<b>77</b>

# List of Figures

2.2.1	Leading order Feynman diagrams corresponding to the top quark pair production through quark anti-quark annihilation and gluon fusion [22]. . . . .	14
2.2.2	Feynman diagrams for the single top quark production at leading order. . . . .	14
2.2.3	Summary of ATLAS and CMS measurements of the single top production cross-sections in various channels as a function of the center of mass energy [24, 25, 26, 27, 28, 29, 30, 31, 32, 33, 34, 35, 36, 37, 38, 39, 40, 41, 42, 43, 44]. . . . .	15
2.3.1	Summary of the current 95% CL observed limits on the branching ratios of the top quark decays via FCNC to a charm quark (left) and to an up quark (right) along with a neutral boson [59]. . . . .	18
3.1.1	Schematic view of the CERN accelerator complex.[62] . . . . .	20
3.3.1	Representation of the ATLAS detector showing the different subsystems.[61]	22
3.3.2	Representation of the ATLAS inner detector. The pixel detectors refers to the Insertable B-Layer and the Pixel Detector. [73] . . . . .	24
3.3.3	Open view of the ATLAS calorimeter system.[74] . . . . .	26
3.3.4	Representation of the ATLAS muon spectrometer.[75] . . . . .	27
3.3.5	The total integrated luminosity delivered in the year of 2015 as a function of time [76]. . . . .	29

---

3.3.6 Representation of the structure of the tiers 0, 1 and 2. The various locations of the thirteen computer centres of tier 1 can also be found [78]. . . . .	31
4.2.1 The efficiency to tag $b$ , $c$ and light-flavour jets for the MV2c20 tagger with the 77% working point. Efficiencies are shown as a function of the jet $p_T$ and $ \eta $ [92, 93]. . . . .	36
4.3.1 Distributions concerning the leptons after require events containing exactly one jet. . . . .	38
4.3.2 Distributions of relevant variables after require exactly one jet and three leptons. . . . .	39
4.6.1 Signal region distributions before and after the $b$ -tagged jet requirement. . . . .	43
4.6.2 Signal region distributions before and after the $b$ -tagged jet requirement. . . . .	44
4.7.1 $Z$ +jets dilepton control region distributions before and after the $b$ -tagged jet requirement. . . . .	48
4.7.2 $Z$ +jets dilepton control region distributions of $b$ -tagged jet multiplicity before and after the final requirement. . . . .	49
4.7.3 $Z$ +jets trilepton control region relevant distributions before and after the $b$ -tagged jet requirement. . . . .	51
4.7.4 $Z$ +jets trilepton control region distributions of $b$ -tagged jet multiplicity before and after the $b$ -tagged jet requirement. . . . .	52
4.7.5 $t\bar{t}$ control region distributions before and after the $b$ -tagged jet requirement. . . . .	53
4.7.6 $WZ$ Diboson control region distributions after the selection criteria. . . . .	57
4.7.7 $tZj$ control region distributions before and after the $b$ -tagged jet requirement. . . . .	59
4.9.1 Two dimensional distributions for different backgrounds shown as a function of the $Z$ boson candidate $p_T$ and the reconstructed top quark mass and the transverse mass of the $W$ boson. . . . .	63



4.9.2	Two dimensional distributions for the $Z$ +jets background and signal, shown as function of the $Z$ boson candidate $p_T$ and the reconstructed top quark mass and the transverse mass of the $W$ boson. . . . .	64
4.9.3	Relevant distributions for the signal region with the added cut on the transverse mass of the $W$ boson. . . . .	66
4.9.4	Relevant distributions of the signal region with the added cut on the reconstructed top quark mass. . . . .	69
5.2.1	The pull plot for the systematics studied in this analysis and their correlation with the signal. . . . .	75
5.2.2	Expected upper limits at 95% CL for the anomalous coupling $K_{Lut}/\Lambda$ considering the expected upper limits of the cross-sections for a luminosity of $3.21 \text{ fb}^{-1}$ and $30 \text{ fb}^{-1}$ and the theoretical prediction. . . . .	76
6.0.1	Luminosity per year for the different centre-of-mass energy at the LHC [100]. . . . .	78



# List of Tables

2.1.1 The fundamental fermions of the Standard Model and their mass and charge according to the Particle data Group [5]. . . . .	5
2.1.2 The interactions in the Standard Model and their mediating gauge bosons with the mass and charge according to the Particle data Group [5]. . . . .	6
2.3.1 The theoretical values for the branching ratios of FCNC top decays predicted by the Standard Model, the quark-singlet model (QS), the two Higgs doublet model (2HDM), the flavour-conserving two Higgs doublet model (FC 2HDM), the minimal supersymmetric model (MSSM) and SUSY with R parity violation ( $\mathcal{R}$ SUSY) [50]. . . . .	16
2.3.2 Summary of the 95% CL observed limits on the branching ratios along with the production mode, the luminosity and the centre-of-mass energy for the different searches performed by the ATLAS and the CMS collaboration. . . . .	17
4.2.1 Operating points for the MV2c20 $b$ -tagging algorithm including the $c$ -jet and light-jets rejection rates [91]. . . . .	36
4.5.1 Background MC samples with the corresponding cross-sections and generators used in the analysis presented in this thesis. . . . .	41
4.6.1 Signal region event yields after the selection criteria. The uncertainties presented corresponds only to the statistical errors. . . . .	45
4.7.1 Selection criteria used to define the considered control regions. . . . .	46

---

4.7.2 $Z$ +jets dilepton control region event yields after the selection criteria. The uncertainties presented corresponds only to the statistical errors. . . . .	49
4.7.3 $Z$ +jets trilepton control region event yields after the selection criteria. The uncertainties presented corresponds only to the statistical errors. . . . .	52
4.7.4 $t\bar{t}$ control region event yields after the selection criteria. The uncertainties presented corresponds only to the statistical errors. . . . .	55
4.7.5 $WZ$ Diboson control region event yields after the selection criteria. The uncertainties presented corresponds only to the statistical errors. . . . .	58
4.7.6 $tZj$ control region event yields after the selection criteria. The uncertainties presented corresponds only to the statistical errors. . . . .	60
4.9.1 Definition of distinct signal region selections in order to separate background for signal. A cut on the transverse mass of $W$ boson or in the reconstructed top quark mass are added to the signal region selection. . . . .	65
4.9.2 Event yields for the signal region selection with a cut on the transverse mass of the reconstructed $W$ boson. The uncertainties presented corresponds only to the statistical errors. . . . .	68
4.9.3 Event yields for the signal region selection with a cut on the reconstructed top quark mass. The uncertainties presented corresponds only to the statistical errors. . . . .	70

# List of Acronyms

**ALICE** A Large Ion Collider Experiment

**ATLAS** A Toroidal LHC ApparatuS

**BSM** Beyond the Standard Model

**CKM** Cabibbo-Kobayashi-Maskawa

**CL** Confidence Level

**CMS** Compact Muon Solenoid

**CERN** *Conseil Européen pour la Recherche Nucléaire*

**FCNC** Flavour Changing Neutral Currents

**LHC** Large Hadron Collider

**LO** Leading Order

**MC** Monte Carlo

**OSSF** Opposite-Sign Same-Flavour

**SM** Standard Model of Particle Physics

**SPS** Super Proton Synchrotron

**PS** Proton Synchrotron

**QCD** Quantum Chromodynamics

**QED** Quantum Electrodynamics

**WLCG** Worldwide LHC Computer GRID

# Chapter 1

## Introduction

The Standard Model of particle physics (SM), developed in the 1960's [1], is the theoretical framework that so far best describes the nature of the subatomic world. This model has been severely tested and has been very successful in the description of the experimental observations. However, this theory cannot explain phenomena like the neutrinos masses or the dark matter and dark energy. Several models were presented to extend the SM since it is thought that it is not the most complete theory of particle physics.

Discovered in 1995 [2, 3], the top quark is the heaviest particle in the SM and decays almost all the times to a  $W$  boson and a  $b$ -quark. The top quark can decay also through a neutral current. Within the SM, the Flavour Changing Neutral Currents (FCNC) processes are forbidden at tree level due to the GIM mechanism [4] and is suppressed at higher orders because of unitarity of the CKM matrix. In extensions of the SM it is possible having FCNC processes at tree level and loop level where enhancements of the FCNC branching ratios were predicted. The study of the top FCNCs interactions can be performed in two modes: one in the  $t$  production along with a  $Z$  boson, Higgs boson or a photon ( $\gamma$ ) and another in the  $t\bar{t}$  decays.

In this thesis, a search for the production of a single top quark in association with a  $Z$  boson is considered. The goal of this thesis is to perform an analysis comparing data events with an integrated luminosity of  $3.21 \text{ fb}^{-1}$  recorded with

---

a centre-of-mass energy of  $\sqrt{s}= 13$  TeV at the ATLAS detector with simulated events for the signal region and for the different control regions. The study of possible discriminant variables for the signal region is also performed, presenting expected limits for the branching ratio of the  $tZ$  production via FCNC processes. In Chapter 2 a review of the SM and an introduction to the FCNC processes are presented. Chapter 3 is composed by a presentation of the CERN and a review of the LHC and of the ATLAS detector. A description of the analysis used to study the signal region and the different control regions is made in Chapter 4. Expected upper limits at 95% confidence level (CL) on the cross-section for the process  $pp \rightarrow tZ$  were obtained in the Run-2 of the LHC at  $\sqrt{s}= 13$  TeV with an integrated luminosity of  $3.21 \text{ fb}^{-1}$  and  $30 \text{ fb}^{-1}$  are presented in Chapter 5. These limits were also interpreted as limits on the coupling  $tZq$  and the branching ratio of the decay  $t \rightarrow qZ$ .



# Chapter 2

## The Standard Model of particle physics and beyond

The SM is the theoretical framework that so far better describes the subatomic world. Developed in the 1960's [1], it has been tested and successful in describing the experimental observations. This chapter briefly introduces the structure of the SM and the FCNC interactions.

### 2.1 The Standard Model of particle physics

The matter is made from atoms which are made from electrons and nuclei. The atomic nucleus is made of neutrons and protons and both of them are made of elementary particles named quarks. The elementary particles interact via four fundamental forces in nature: strong force, weak force, electromagnetic force and gravitational force.

The strong interaction is responsible for the stability of the atomic nuclei by preventing them from fragmenting as a result of the electric repulsion of the protons and is a very short range force (typically around  $10^{-15}$  m). The weak force is responsible for the beta decay of unstable atoms and acts at very short distances (typically around  $10^{-18}$  m). The electromagnetic interaction acts over an infinite range and is responsible for the interaction between electric charged particles. The

electromagnetic force is well defined through the Maxwell equations. The gravitational force is an interaction between massive objects with an infinite range. The strong, weak and electromagnetic forces are the interactions included in the SM of particle physics.

Based on relativistic quantum field theory, the SM describes the interactions between the elementary particles. This model assumes that matter is made from elementary point-like particles with spin 1/2 called fermions. The interactions between the fermions are mediated by spin 1 particles called bosons. There are two types of fermions: quarks and leptons. The leptons are divided in the electrically charged with the fundamental charge of  $e = -1.6 \times 10^{-19}$  C and the electrically neutral particles called neutrinos ( $\nu$ ). In the other hand, the quarks carry fractional charge which can be  $+2/3 |e|$  or  $-1/3 |e|$ . The quarks carry also another quantum number which is the colour charge. This charge is of three different types: red, green or blue. Another characteristic of the fermions is that every particle has an associated antiparticle with the same mass but carrying the opposite charge to its corresponding particle.

The fermions are grouped into three generations. The difference between the generations is the flavour, *i.e.* the fermion type, and the mass of the particles, remaining the other corresponding quantum numbers. Each generation is defined by two doublets, one in the lepton family and one in the quark family. The doublet from the lepton family contains a charged lepton and his partner neutrino. The doublet from the quark family contains a quark with a charge of  $+2/3 |e|$  and a quark with a charge of  $-1/3 |e|$ . There are three lepton doublets: the electron ( $e$ ) with his partner electron neutrino ( $\nu_e$ ), the muon ( $\mu$ ) with his partner muon neutrino ( $\nu_\mu$ ) and the tau ( $\tau$ ) with his partner tau neutrino ( $\nu_\tau$ ). The electron doublet, the muon doublet and the tau doublet correspond to the first, second and third generation of leptons, respectively.

There are three quark doublets: the up quark ( $u$ ) with the down quark ( $d$ ), the charm quark ( $c$ ) with the strange quark ( $s$ ) and the top quark ( $t$ ) with the bottom quark ( $b$ ). The up doublet, the charm doublet and the top doublet correspond to the first, second and third generation of quarks, respectively. The elementary

particles in the SM are listed in Table 2.1.1.

Generation	Symbol	Name	Mass	Electric charge ( $ e $ )
<b>Quarks</b>				
$1^{st}$	$u$	Up	2.3 MeV	+2/3
	$d$	Down	4.8 MeV	-1/3
$2^{nd}$	$c$	Charm	1.3 GeV	+2/3
	$s$	Strange	95 MeV	-1/3
$3^{rd}$	$t$	Top	173.5 GeV	+2/3
	$b$	Bottom	4.6 GeV	-1/3
<b>Leptons</b>				
$1^{st}$	$e$	Electron	0.5 MeV	-1
	$\nu_e$	Electron Neutrino	< 2 eV	0
$2^{nd}$	$\mu$	Muon	105.7 MeV	-1
	$\nu_\mu$	Muon Neutrino	< 2 eV	0
$3^{rd}$	$\tau$	Tau	1.8 GeV	-1
	$\nu_\tau$	Tau Neutrino	< 2 eV	0

Table 2.1.1: The fundamental fermions of the Standard Model and their mass and charge according to the Particle data Group [5].

The bosonic sector is responsible for the interactions described in the SM. The electromagnetic force carrier is the photon ( $\gamma$ ). The photon is a massless particle and electrically neutral. The weak force carriers are the  $W^\pm$  and  $Z$  bosons. Before their discovery, the theory predicted that they should be massive. The  $Z$  boson is electrically neutral and the  $W^\pm$  bosons have positive and negative electric

charge, respectively. The strong force carriers are the gluons ( $g$ ) which are massless particles with no electric charge. Since gluons carry colour charge with eight combinations, they interact among themselves and only couple to the strong charged particles. Consequently, only quarks can participate in the strong interaction. The gauge bosons of the three forces and their characteristics are summarized in Table 2.1.2.

Beside this twelve gauge bosons, the SM contains one scalar boson, the Higgs boson.

Interaction	Mediator	Mass (GeV)	Electric Charge ( $ e $ )
Strong	Gluon $\times 8$ ( $g$ )	0	0
Electromagnetic	Photon ( $\gamma$ )	0	0
Weak	$Z$	91.19	0
	$W^\pm$	80.39	$\pm 1$

Table 2.1.2: The interactions in the Standard Model and their mediating gauge bosons with the mass and charge according to the Particle data Group [5].

### 2.1.1 Quantum electrodynamics

The classical theory of electromagnetic interactions is well known through the Maxwell equations of the nineteenth century. The theory of Quantum Electrodynamics (QED) unified electrodynamics and quantum mechanics providing a quantum field theory based on the gauge invariance of electrodynamics. The QED theory describes the interactions between electrically charged particles mediated by a quantized electromagnetic field.

The free spin 1/2 particles are described in the Dirac Lagrangian

$$\mathcal{L}_{Dirac} = \bar{\psi}(i\gamma^\mu\partial_\mu - m)\psi \quad (2.1.1)$$

where  $\bar{\psi}$  corresponds to  $\gamma^0\psi^\dagger$ ,  $\gamma^\mu$  ( $\mu=1,2,3,4$ ) corresponds to the Dirac matrices,  $m$  is the fermion mass and  $\psi$  is the Dirac field. The Dirac matrices satisfy the

following relations

$$\begin{aligned}\gamma^\mu, \gamma^\nu &= \gamma^\mu \gamma^\nu + \gamma^\nu \gamma^\mu = 2g^{\mu\nu} \text{ where } g^{\mu\nu} \equiv \text{Metric tensor,} \\ \gamma_5 &= \gamma^5 = i\gamma^1 \gamma^2 \gamma^3 \gamma^4, \\ \sigma^{\mu\nu} &= \frac{i}{2}[\gamma^\mu, \gamma^\nu] = \frac{i}{2}(\gamma^\mu \gamma^\nu - \gamma^\nu \gamma^\mu).\end{aligned}\tag{2.1.2}$$

However, this Lagrangian is not invariant under a local  $U(1)$  gauge transformation of the form

$$\psi \longrightarrow e^{-ie\alpha(x)}\psi \text{ and } \bar{\psi} \longrightarrow e^{ie\alpha(x)}\bar{\psi}\tag{2.1.3}$$

where  $e$  is in units of the electric charge of the proton and  $\alpha$  is a real number. With this transformation the Dirac Lagrangian acquires an additional term of  $\bar{\psi}e\gamma^\mu\partial_\mu\psi$ . To obtain a  $U(1)$  invariant Lagrangian, another term with the expression  $\bar{\psi}e\gamma^\mu A_\mu\psi$  is added, where  $A_\mu$  is the four-potential of the electromagnetic field.

Adding this term and the free field dynamics, described by the Maxwell equation, the QED Lagrangian can be obtained:

$$\mathcal{L}_{QED} = -\frac{1}{4}F^{\mu\nu}F_{\mu\nu} + \bar{\psi}[i\gamma^\mu(\partial_\mu - eA_\mu) + m]\psi\tag{2.1.4}$$

where  $F^{\mu\nu} = \partial_\mu A_\nu - \partial_\nu A_\mu$  is the electromagnetic field tensor. Requiring local phase invariance under  $U(1)$  applied to free Dirac Lagrangian, it is generated all of electrodynamics and introduced a massless field which can be interpreted as the photon.

### 2.1.2 Quantum chromodynamics

The interactions between quarks and gluons are described by a quantum field theory called Quantum Chromodynamics (QCD) [6]. Analogous to the electric charge in QED, each quark has an internal degree of freedom known as colour. This new quantum number was introduced to explain how bound states of three identical quarks can exist and not violate the Pauli exclusion principle. The quark colour state could be red (R), green (G) or blue (B). In this theory, the quarks interact with each other through a gluon exchange. The gluon exchange changes the colour state of the interacting quarks. The gluons also interact with each other implying that the gluons are also colour carriers.

The QCD theory is based on the gauge group  $SU(3)$  where exists three dimensions and each dimension is a colour (R, G and B). The number of gluons is eight since  $SU(3)$  has eight generators where each generator represents a colour exchange and a gauge boson (gluon) in colour space. The generators of  $SU(3)$  are written as

$$t^a = \frac{1}{2}\lambda_a \quad (2.1.5)$$

where  $\lambda_a$  with  $a = 1, 2, \dots, 8$  corresponds to the Gell-Mann matrices. Each quark flavour consists in a triplet of fields represented as

$$q = \begin{pmatrix} q_R \\ q_G \\ q_B \end{pmatrix} \quad (2.1.6)$$

where each of this fields is a Dirac spinor associated to a colour state.

The QCD Lagrangian is

$$\mathcal{L}_{QCD} = \bar{q}(i\gamma^\mu D_\mu - m)q - \frac{1}{4}G_{\mu\nu}^a G_a^{\mu\nu} \quad (2.1.7)$$

with the covariant derivative  $D_\mu = \partial_\mu + ig_s t_a G_\mu^a$  and the strength field tensor defined by

$$G_{\mu\nu}^a = \partial_\mu G_\nu^a - \partial_\nu G_\mu^a - g_s f^{abc} G_\mu^b G_\nu^c \quad (2.1.8)$$

where  $G_\mu^a$  are the gluon fields,  $g_s$  is the QCD gauge coupling constant and  $f^{abc}$  are the structure constant of  $SU(3)_c$  defined by the commutation relation  $[t^a, t^b] = i f^{abc} t^c$ .

The QCD theory has been very successful in the description of the interactions binding quarks to hadrons. However, there are two important characteristics of this theory: asymptotic freedom and confinement [7, 8]. Asymptotic freedom means that at very high energies and short distances quarks and gluons interact weakly with each other allowing the computation of observables using the perturbation theory. Confinement means that at very low energy scales which corresponds to large distances, when we try to separate quarks, the energy of the gluon field increases, creating quark and anti-quark pairs and, consequently, free quarks cannot exist.

### 2.1.3 Electroweak theory

Proposed by Glashow, Salam and Weinberg [9, 10, 11], the electroweak theory is a unified theory of electroweak interactions which describe the weak and electromagnetic forces from a single gauge group  $SU(2)_L \otimes U(1)_Y$  where  $Y$  corresponds to the weak hypercharge. The weak hypercharge is given by the Gell-Mann-Nishijima relation  $Y = 2(Q - T_3)$  where  $T_3$  is the third component of the weak isospin operator  $\hat{T} = \sigma_i/2$  ( $i=1,2,3$ ) with  $\sigma_i$  corresponding to the three Pauli matrices and  $Q$  is the fermion electric charge (in units of  $|e|$ ). The subscript in  $SU(2)_L$  refers to the fact that only left-handed fermions interact through the weak force. The electroweak interaction is the interaction responsible for the change of flavour of leptons and quarks.

The left-handed and right-handed components of the fermions fields can be obtained via the operators of the weak symmetry group

$$\begin{aligned}\psi_L &= \frac{1}{2}(1 - \gamma^5)\psi, \\ \psi_R &= \frac{1}{2}(1 + \gamma^5)\psi.\end{aligned}\tag{2.1.9}$$

Right-handed fermions transform as singlets and left-handed fermions transform as doublets

$$\begin{aligned}f_R^i &= l_R^i, u_R^i, d_R^i, \\ f_L^i &= \begin{pmatrix} l_L^i \\ \nu_L^i \end{pmatrix}, \begin{pmatrix} u_L^i \\ d_L^i \end{pmatrix},\end{aligned}\tag{2.1.10}$$

with  $i = 1,2,3$  corresponding to the generation index. It is necessary define the Lagrangian of the gauge field

$$\mathcal{L}_{gauge} = -\frac{1}{4}W_{\mu\nu}^i W_i^{\mu\nu} - \frac{1}{4}B_{\mu\nu} B^{\mu\nu}.\tag{2.1.11}$$

The  $W_{\mu\nu}^i$  and  $B_{\mu\nu}$  are the field strength tensors for the weak isospin and weak hypercharge fields and they can be explicitly written as

$$\begin{aligned}W_{\mu\nu}^i &\equiv \partial_\mu W_\nu^i - \partial_\nu W_\mu^i + g\epsilon^{ijk}W_\mu^j W_\nu^k, \\ B_{\mu\nu} &\equiv \partial_\mu B_\nu - \partial_\nu B_\mu,\end{aligned}\tag{2.1.12}$$

where  $\epsilon^{ijk}$  corresponds to the totally antisymmetric Levi-Civita tensor,  $g$  corresponds to the  $SU(2)_L$  gauge coupling,  $W_\nu^i$  and  $B_\nu$  are the gauge bosons of  $SU(2)_L$  and  $U(1)_Y$  respectively and  $i$  take values of 1, 2 or 3. Finally, this theory could be described through the Lagrangian

$$\mathcal{L}_{EW} = \sum_{f=l,q} \bar{f}(i\gamma^\mu D_\mu)f + \mathcal{L}_{gauge} \quad (2.1.13)$$

where covariant derivative  $D_\mu$  is defined by

$$D_\mu \equiv \partial_\mu - ig\vec{T} \cdot \vec{W}_\mu - ig'\frac{Y}{2}B_\mu \quad (2.1.14)$$

where  $g$  and  $g'$  are the coupling constants of the  $SU(2)_L$  and  $U(1)_Y$  gauge groups, respectively.

At this point, these gauge boson fields are massless in order to maintain the gauge invariance while we know that the weak interaction is mediated by heavy bosons ( $W^\pm$  and  $Z$ ).

#### 2.1.4 The Brout-Englert-Higgs mechanism

Proposed by three independent groups [12, 13, 14], the Brout-Englert-Higgs mechanism solved the contradiction between massive particles and the requirement of gauge invariance. This mechanism is based in a spontaneous symmetry breaking, where the symmetry group  $SU(2)_L \otimes U(1)_Y$  breaks down to  $U(1)_{EM}$ . The Higgs field is an isospin doublet of complex scalar fields and is defined as

$$\Phi \equiv \begin{pmatrix} \phi^+ \\ \phi^0 \end{pmatrix} \quad (2.1.15)$$

where  $\phi^+$  corresponds to a electrically charged field and  $\phi^0$  to a electrically neutral field.

The Lagrangian which describes the free Higgs field is defined as

$$\mathcal{L}_\Phi = (D_\mu\Phi)^\dagger(D^\mu\Phi) - V(\Phi) \quad (2.1.16)$$

with the covariant derivative  $D_\mu$  given by Equation 2.1.14 and the  $V(\Phi)$  corresponding to the Higgs potential defined as

$$V(\Phi) = \mu^2\Phi^\dagger\Phi + \lambda(\Phi^\dagger\Phi)^2. \quad (2.1.17)$$



The Higgs potential depends on the parameters  $\mu^2$  and  $\lambda$ . Consider the case where  $\mu^2 < 0$  e  $\lambda > 0$ , the minimum of the potential  $V(\Phi)$  is given by

$$\Phi^\dagger \Phi = -\frac{\mu^2}{2\lambda} \equiv \frac{v^2}{2} \quad (2.1.18)$$

and the Higgs field has a non-zero vacuum expectation value of  $v/\sqrt{2}$  and does not have a unique minimum. The Higgs potential minimum could be chosen in a way that the Higgs field acquiring a vacuum expectation value is the electrically neutral field and the Equation 2.1.15 can be rewritten as

$$\Phi(x) = \frac{1}{\sqrt{2}} \begin{pmatrix} 0 \\ v + H(x) \end{pmatrix} \quad (2.1.19)$$

where  $H(x)$  represents the ground state fluctuations around the vacuum state. The interaction between the Higgs field and the fermions fields could be written as

$$\mathcal{L}_{Yukawa} = \sum_{f=l,q} y_f (\bar{f}_L \Phi f_R + \bar{f}_R \bar{\Phi} f_L) \quad (2.1.20)$$

where the matrices  $y_f$  describe the Yukawa couplings between the Higgs doublet and the fermions. This Lagrangian, called the Yukawa Lagrangian, is gauge invariant since the terms  $\bar{f}_L \Phi f_R$  and  $\bar{f}_R \bar{\Phi} f_L$  are singlets. Through the Yukawa Lagrangian, the Higgs field and the Higgs Lagrangian, the prediction for the mass of the fermions and the mass of the Higgs boson can be obtained

$$\begin{aligned} m_f &= y_f \frac{v}{\sqrt{2}}, \\ m_H &= \sqrt{2\lambda}v. \end{aligned} \quad (2.1.21)$$

The mass of the Higgs boson could not be predicted since the value of the  $\lambda$  is unknown by the theory. The electroweak boson masses could also be obtained through the Higgs Lagrangian and can be written as

$$\begin{aligned} m_W &= \frac{vg}{2}, \\ m_Z &= v \frac{\sqrt{g^2 + g'^2}}{2}, \\ m_\gamma &= 0. \end{aligned} \quad (2.1.22)$$

The  $W^\pm$  boson can couple the up type quarks with the down type quarks from another generation changing the quark flavour. The Cabibbo-Kobayashi-Maskawa (CKM) matrix describe the strength of flavour changing weak decays. The CKM matrix consists in a  $n \times n$  unitary matrix which describe  $n$  quark families. Imposing the three known particle generations and the unitarity of the matrix, the CKM matrix can be obtained through a global fit to all available measurements [5]:

$$V_{CKM} = \begin{pmatrix} |V_{ud}| & |V_{us}| & |V_{ub}| \\ |V_{cd}| & |V_{cs}| & |V_{cb}| \\ |V_{td}| & |V_{ts}| & |V_{tb}| \end{pmatrix} = \quad (2.1.23)$$

$$= \begin{pmatrix} 0.97427 \pm 0.00014 & 0.22536 \pm 0.00061 & 0.00355 \pm 0.00015 \\ 0.22522 \pm 0.00061 & 0.97343 \pm 0.00015 & 0.0414 \pm 0.0012 \\ 0.00886 \pm 0.00033 & 0.0405 \pm 0.0011 & 0.99914 \pm 0.00005 \end{pmatrix}$$

The theory of SM is based in the combination of the electroweak and strong interactions through a gauge theory with the underlying symmetry group  $SU(3)_c \otimes SU(2)_L \otimes U(1)_Y$ . Except for gravity, the SM explain the fundamental interactions of fermionic fields having free parameters corresponding to [15]:

- three coupling parameters ( $g, g'$  and  $g_s$ );
- two parameters to define the Higgs potential ( $\mu^2$  and  $\lambda$ );
- six Yukawa couplings of the quarks to the Higgs field;
- four parameters for the CKM matrix corresponding to three mixing angles and one CP-violating phase;
- three charged lepton masses;
- one parameter related with non-perturbative CP violation in QCD.

Since its formulation, the SM has been strongly tested and proved to be a well based theory. However, there are also some open questions that the SM cannot answer as, for example, the matter anti-matter asymmetry, the number of fermion

generations and the mass of neutrinos confirmed by neutrino oscillations [16, 17, 18, 19, 20]. Knowing that neutrinos have mass, the SM was extended with seven more parameters (three parameters for neutrino masses, three for their mixing angles and one for CP violating phase for the neutrino mixing matrix). The SM as described here has a total of 26 parameters.

## 2.2 Top quark physics

Discovered in 1995 by the *CDF* and *DØ* collaborations at Fermilab [2, 3], the top quark is the heaviest elementary particle known so far. Its existence has been postulated since the discovery of the bottom quark allowing the completion of the third generation of the SM. With the discovery of the top quark, a new field of particle physics opened due to its exciting properties:

- It is the only quark that decays before hadronising due to the very short lifetime around  $10^{-25}$  s [21];
- It is the heaviest quark with a mass close to the electroweak symmetry breaking scale of  $v = 246$  GeV [5];
- Determined by the CKM matrix ( $|V_{tb}|$ ), the decay is dominated by the  $t \rightarrow Wb$  channel with a branching ratio of approximately 1 [5].

The top quark can be produced in top quark pairs called  $t\bar{t}$  production or as a single top-quark associated with other particles called single top quark production. In hadron colliders, the  $t\bar{t}$  production occurs dominantly through the strong interaction (QCD). In the  $pp$  collider LHC, unlike the  $p\bar{p}$  collider Tevatron, the top quark pair is produced dominantly through the gluon fusion (around 85%). The quark anti-quark annihilation and the gluon fusion processes at Leading Order (LO) are shown in Figure 2.2.1.

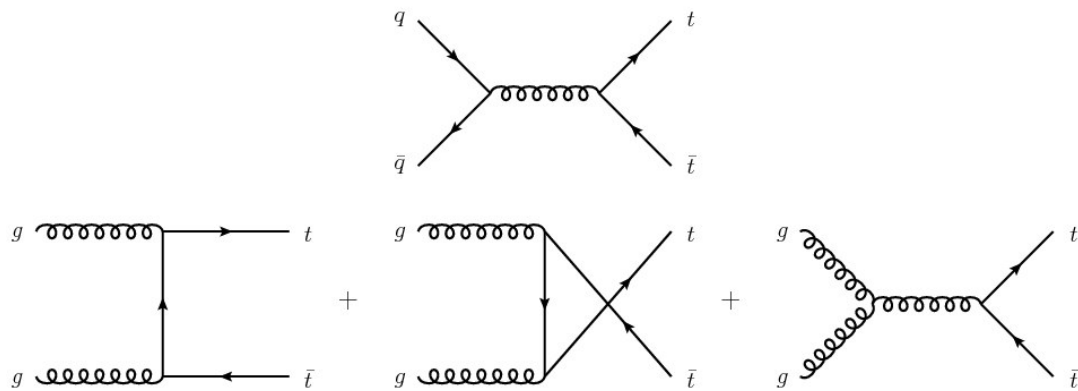


Figure 2.2.1: Leading order Feynman diagrams corresponding to the top quark pair production through quark anti-quark annihilation and gluon fusion [22].

Considering the single top quark production, the top quark is produced via the weak interaction in three different channels:

- $t$ -channel:  $W$  boson and gluon fusion (shown in Figure 2.2.2(a));
- $Wt$ -channel: associated production of a top quark and a  $W$  boson (shown in Figure 2.2.2(b));
- $s$ -channel:  $W$  boson and quark anti-quark annihilation (shown in Figure 2.2.2(c)).

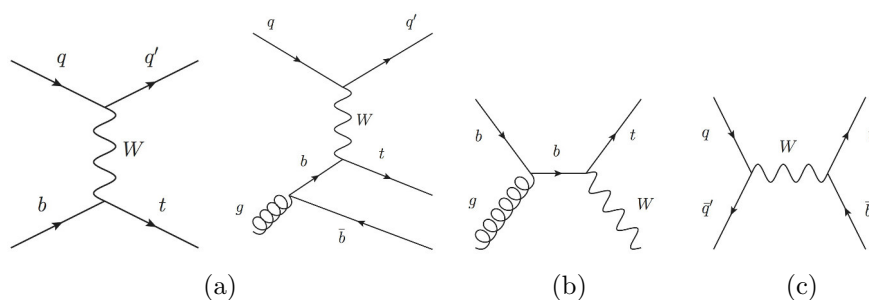


Figure 2.2.2: Feynman diagrams for the single top quark production at leading order: (a)  $t$ -channel, (b)  $Wt$ -channel and (c)  $s$ -channel [23].

The cross-section values for the three channels are presented in Figure 2.2.3 with the ATLAS and CMS measurements and the theoretical calculations which are

based on NLO QCD, NLO QCD complemented with NNLL and NNLO QCD (for  $t$ -channel only) assuming a  $m_{top}=172.5$  GeV.

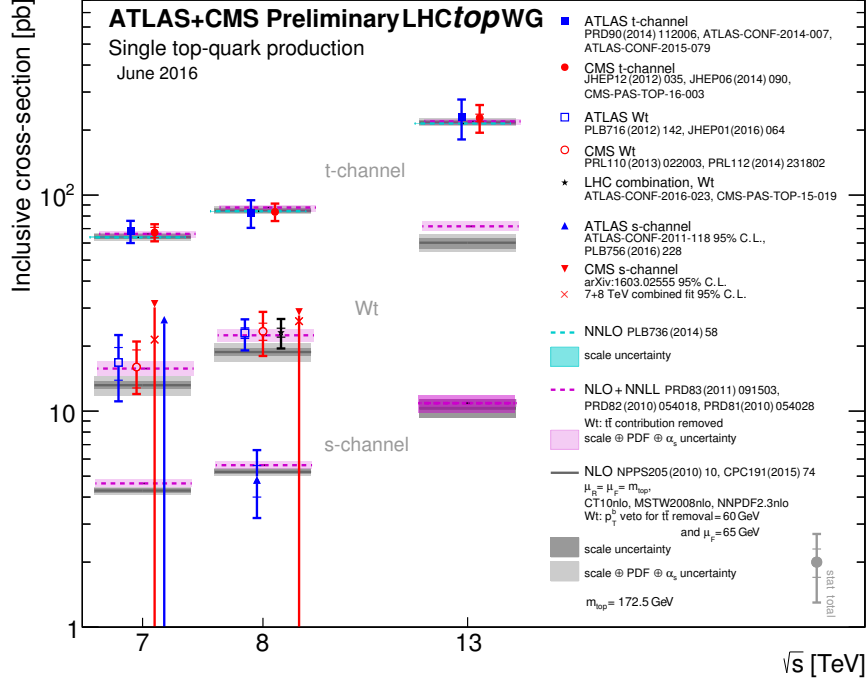


Figure 2.2.3: Summary of ATLAS and CMS measurements of the single top production cross-sections in various channels as a function of the center of mass energy [24, 25, 26, 27, 28, 29, 30, 31, 32, 33, 34, 35, 36, 37, 38, 39, 40, 41, 42, 43, 44].

## 2.3 Top quark FCNC interactions

Flavour Changing Neutral Current (FCNC) corresponds to a interaction with a change in the fermion (quark or lepton) flavour through the emission of a neutral boson. This process is not allowed at tree-level in the SM since there is no vertex that directly couples neutral currents with two fermions from different generations. However, this process can occur at higher order correction or loop-level or in Beyond the Standard Model (BSM) models. The branching ratio of top quark decay via FCNC is highly suppressed since it suffers from the small decay width through FCNC [4] and the large tree-level rate for top quark decay to a  $b$  quark and

a  $W$  boson. In the other hand, there are several new physics models that predict FCNCs with higher branching ratios by several orders of magnitude and where it is possible to have this processes at tree-level. A comparison between SM and new physics models predictions for branching ratios of the decays of the top quark to a up or a charm quark and a neutral boson is shown in Table 5.2.2. Several theoretical studies has been done through the years related to FCNC processes. Two examples of these studies are related with the FCNC processes on the strong sector [45, 46] or the implementation of a Lagrangian describing these processes in a Universal Feynrules Output (UFO) model using dimension-six gauge invariant operators [47, 48, 49].

Process	SM	QS	2HDM	FC 2HDM	MSSM	$\mathcal{R}$ SUSY
$t \rightarrow gu$	$3.7 \times 10^{-14}$	$1.5 \times 10^{-7}$	–	–	$8 \times 10^{-5}$	$2 \times 10^{-4}$
$t \rightarrow Zu$	$8 \times 10^{-17}$	$1.1 \times 10^{-4}$	–	–	$2 \times 10^{-6}$	$3 \times 10^{-5}$
$t \rightarrow \gamma u$	$3.7 \times 10^{-16}$	$7.5 \times 10^{-9}$	–	–	$2 \times 10^{-6}$	$1 \times 10^{-6}$
$t \rightarrow Hu$	$2 \times 10^{-17}$	$4.1 \times 10^{-5}$	$5.5 \times 10^{-6}$	–	$10^{-5}$	$\sim 10^{-6}$
$t \rightarrow gc$	$4.6 \times 10^{-12}$	$1.5 \times 10^{-7}$	$\sim 10^{-4}$	$\sim 10^{-8}$	$8 \times 10^{-5}$	$2 \times 10^{-4}$
$t \rightarrow Zc$	$1 \times 10^{-14}$	$1.1 \times 10^{-4}$	$\sim 10^{-7}$	$\sim 10^{-10}$	$2 \times 10^{-6}$	$3 \times 10^{-5}$
$t \rightarrow \gamma c$	$4.6 \times 10^{-14}$	$7.5 \times 10^{-9}$	$\sim 10^{-6}$	$\sim 10^{-9}$	$2 \times 10^{-6}$	$1 \times 10^{-6}$
$t \rightarrow Hc$	$3 \times 10^{-15}$	$4.1 \times 10^{-5}$	$1.5 \times 10^{-3}$	$\sim 10^{-5}$	$10^{-5}$	$\sim 10^{-6}$

Table 2.3.1: The theoretical values for the branching ratios of FCNC top decays predicted by the Standard Model, the quark-singlet model (QS), the two Higgs doublet model (2HDM), the flavour-conserving two Higgs doublet model (FC 2HDM), the minimal supersymmetric model (MSSM) and SUSY with R parity violation ( $\mathcal{R}$  SUSY) [50].

Searches for FCNC interactions in the top sector have already been performed at the Tevatron [51, 52] and the LHC. The ATLAS collaboration performed searches for  $tgq$  anomalous couplings [53] and the CMS collaboration searches for  $t\gamma q$  anomalous couplings [54]. Concerning the  $tZq$  anomalous couplings, both the AT-

LAS and the CMS collaboration obtained expected and observed upper limits at 95% CL for  $tZ$  production,  $t\bar{t}$  decay [55, 56, 57] and for the two production modes combined [58]. The most stringent and recent exclusion limit on  $\mathcal{BR}(t \rightarrow qZ)$  excluded at 95% CL branching ratios for  $tZ$  production via FCNC greater than 0.02% [58]. Searching for the production of a single top quark in association with a  $Z$  boson is a good strategy due to the sensitivity of these processes to both  $tZq$  and  $tgq$  anomalous couplings.

$t$ production 20 fb <sup>-1</sup> $\sqrt{s}$ = 8 TeV [53]	$\mathcal{BR}(t \rightarrow ug) < 4 \times 10^{-5}$ $\mathcal{BR}(t \rightarrow cg) < 2 \times 10^{-4}$	
$t$ production 20 fb <sup>-1</sup> $\sqrt{s}$ = 8 TeV [54]	$\mathcal{BR}(t \rightarrow u\gamma) < 1 \times 10^{-4}$ $\mathcal{BR}(t \rightarrow c\gamma) < 2 \times 10^{-3}$	
$tZ$ production 5 fb <sup>-1</sup> $\sqrt{s}$ = 7 TeV [56]	$\mathcal{BR}(t \rightarrow ug) < 6 \times 10^{-3}$ $\mathcal{BR}(t \rightarrow cg) < 7 \times 10^{-2}$	$\mathcal{BR}(t \rightarrow uZ) < 5 \times 10^{-3}$ $\mathcal{BR}(t \rightarrow cZ) < 1 \times 10^{-1}$
$t\bar{t}$ decay 20 fb <sup>-1</sup> $\sqrt{s}$ = 8 TeV [55]		$\mathcal{BR}(t \rightarrow qZ) < 7 \times 10^{-4}$ $q = u, c$
$t\bar{t}$ decay 20 fb <sup>-1</sup> $\sqrt{s}$ = 8 TeV [57]		$\mathcal{BR}(t \rightarrow qZ) < 6 \times 10^{-4}$ $q = u, c$
$tZ$ production and $t\bar{t}$ decay 20 fb <sup>-1</sup> $\sqrt{s}$ = 8 TeV [58]		$\mathcal{BR}(t \rightarrow uZ) < 1.7 \times 10^{-4}$ $\mathcal{BR}(t \rightarrow cZ) < 2.0 \times 10^{-4}$

Table 2.3.2: Summary of the 95% CL observed limits on the branching ratios along with the production mode, the luminosity and the centre-of-mass energy for the different searches performed by the ATLAS and the CMS collaboration.

Figure 2.3.1 shows a summary of the current 95% CL observed limits on the branching ratios specifically of the top decays via FCNC to a charm quark with a neutral boson and to an up quark with a neutral boson.

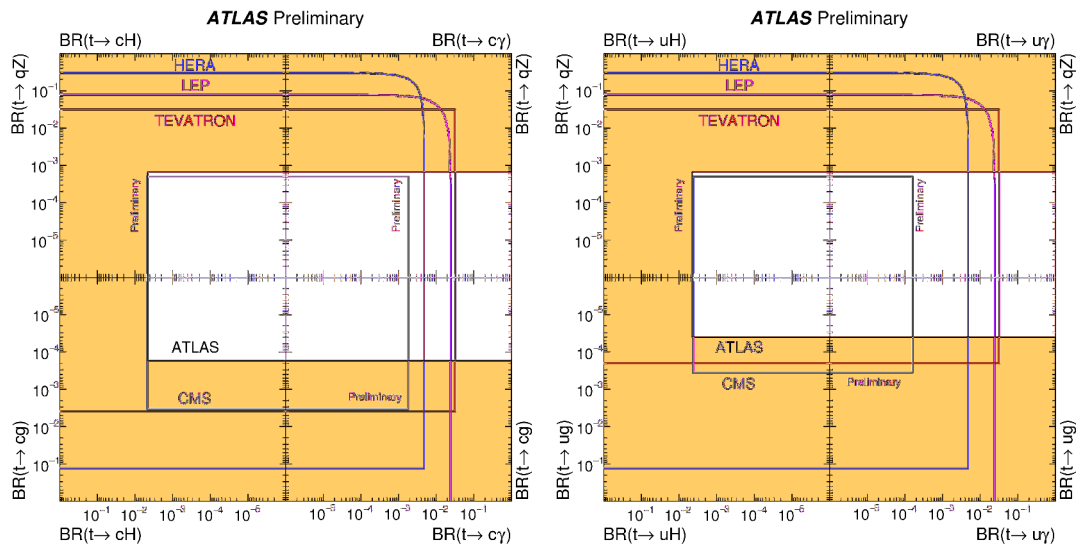


Figure 2.3.1: Summary of the current 95% CL observed limits on the branching ratios of the top quark decays via FCNC to a charm quark (left) and to an up quark (right) along with a neutral boson [59].



# Chapter 3

## Experimental Setup

Located at the European Organization for Nuclear Research (CERN), the Large Hadron Collider (LHC) [60] is the world's highest energy particle accelerator. The ATLAS experiment [61] is one of the four large experiments that benefit from the collisions of the particles in the LHC. In this chapter an introduction to the CERN's accelerator complex, the LHC and the ATLAS detector is presented.

### 3.1 CERN

Based on the Franco-Swiss border near Geneva, the CERN was founded in September 29<sup>th</sup> of 1954 with 12 member states and the acronym CERN *Conseil Européen pour la Recherche Nucléaire* was born. The initial goal of this council was the study of atomic nuclei and the congregation of scientists. It was soon improved to the research in the high energy physics focusing in the interactions of subatomic particles.

CERN has built several accelerators and detectors with distinct targets in the particle physics field to probe the fundamental structure of the Universe. Figure 3.1.1 shows the accelerators and the detectors currently working at CERN.

Since its beginning, CERN played a major role in the great achievements in particle physics. Among them are the discovery of neutral currents with the Gargamelle bubble chamber (1973) [63], the discovery of  $W^\pm$  and  $Z$  boson with the UA1

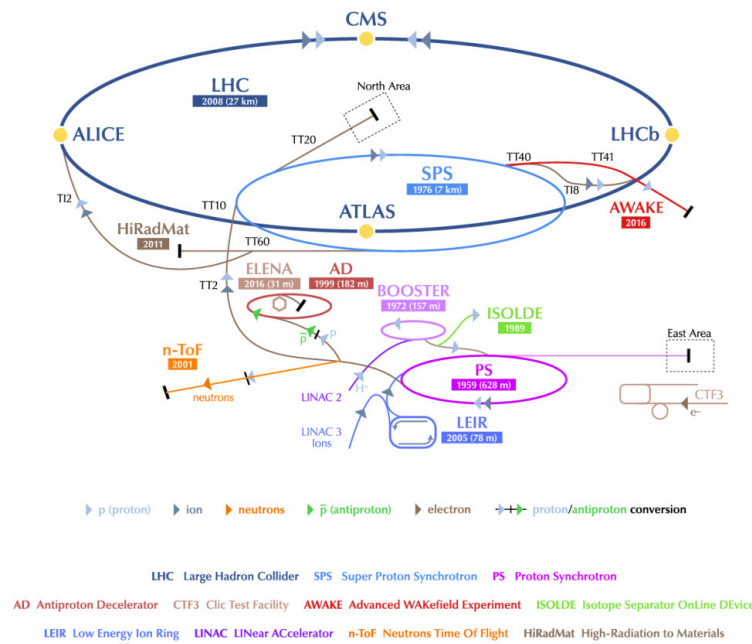


Figure 3.1.1: Schematic view of the CERN accelerator complex.[62]

and UA2 experiments (1983) [64, 65], the determination of the number of light neutrino families at the Large Electron-Positron Collider (LEP) (1989) [66], the discovery of direct CP violation [67](1999) and the latest discovery of the Higgs boson [68, 69](2012) with a mass of 125 GeV observed by the ATLAS and the CMS collaboration to fulfill the SM.

Through the years, the CERN laboratory has become more than an european organization having already 22 member states and receiving more than 12,000 scientists from over 70 countries for their research.

## 3.2 The Large Hadron Collider

The latest addition to the CERN's accelerator complex was the Large Hadron Collider [60]. Today it is the world's largest and most powerful particle accelerator.

Located in a tunnel 100 meters underground, the LHC consists of a ring with a perimeter of 27 kilometers of superconducting magnets and several accelerating structures. Inside the tunnel, two proton beams, traveling in opposite directions in separate beam pipes, are accelerated until reaching a speed close to the speed of light.

Older accelerators like the Proton Synchrotron (PS) and Super Proton Synchrotron (SPS) are used to boost the energy of the particles before the injection in the LHC. First they are accelerated at the LINear ACcelerator 2 (LINAC 2) reaching an energy of 50 MeV. After that they are accelerated in the Proton Synchrotron Booster (BOOSTER), PS and SPS until they have an energy of 1, 25 and 450 GeV, respectively. Finally, the bunches of protons are injected in the LHC (each bunch contains about  $10^{11}$  protons). The first protons beams circulated in the LHC for the first time in September 10<sup>th</sup> of 2008. From 2010 to 2012, the protons beams had an energy of 3.5 TeV. From 2012 to 2013, the energy reached was 4 TeV per beam. The first shutdown ended when the LHC started to accelerate beams up to an energy of 6.5 TeV in April 5<sup>th</sup> of 2015. Since then, the LHC have been performing very well running at  $\sqrt{s}=13$  TeV for the rest of 2015 and 2016.

Since the protons are charged particles, a strong magnetic field maintained by electromagnets is needed to curve the proton beams around the circular accelerator. The total of 1232 superconducting electromagnets requires a temperature of 1.9 K (-271.3 °C) which is colder than outer space and, consequently, a ultrahigh vacuum. This temperature allows this dipole magnets to generate a magnetic field of 8 T. Besides this magnets, a total of 392 quadrupole magnets maintain the beams focused and 16 radiofrequency cavities accelerate particles and keep them in controlled bunches with an constant energy.

The beams inside the LHC intersect in four interaction points where distinct particle detectors are placed: A Large Ion Collider Experiment (ALICE) [70], A Toroidal LHC ApparatuS (ATLAS) [61], Compact Muon Solenoid (CMS) [71] and Large Hadron Collider beauty (LHCb) [72]. The ATLAS and CMS detectors are two multi-purpose experiments, and ALICE and LHCb are focused on the study of heavy-ions collisions, and CP violation and *b*-physics, respectively.

### 3.3 The ATLAS detector

The ATLAS detector, shown in Figure 3.3.1, is one of the two general purpose detectors at the LHC that explores a vast range of physics scenarios studying the particles produced in proton-proton collisions at high energies [61]. It is the biggest detector of this kind built having 44 meters long, 25 meters wide and weighting 7000 tonnes.

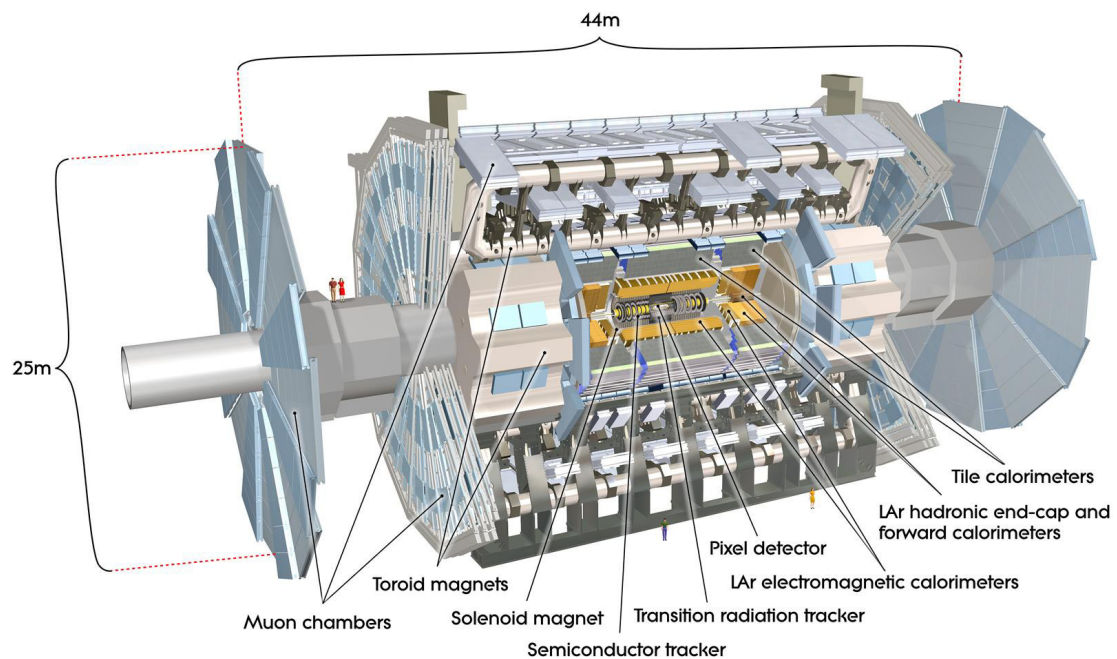


Figure 3.3.1: Representation of the ATLAS detector showing the different subsystems.[61]

The full coverage of the space around the  $pp$  interaction point allows the detection and the reconstruction of almost all final state objects. This full coverage is possible due to the multilayer structure which consists in many sub-detectors, each of them with a specific purpose. From inside to outside, the sub-detectors are: the inner detector, the electromagnetic calorimeter, the hadronic calorimeter and the muon spectrometer.

The ATLAS coordinate system is a right-handed cartesian system, with the  $x$ -axis

towards the center of the LHC ring, the  $y$ -axis pointing upwards and the  $z$ -axis pointing along the beam pipe. The nominal interaction point is defined as the origin of the coordinate system. To better describe rotational invariant properties, the spherical coordinates  $(R, \phi, \theta)$  are used and defined by

$$R = \sqrt{x^2 + y^2}, \phi = \arctan(y/x), \theta = \arctan(R/z). \quad (3.3.1)$$

The azimuthal angle  $\phi$  is the angle between the  $x$ -axis and the  $y$ -axis and the polar angle  $\theta$  is defined as the angle between the  $z$ -axis and the  $x - y$  plane. The azimuthal angle is defined within  $\phi \in [-\pi, \pi]$  and the polar angle within  $\theta \in [0, \pi]$ . The particle momentum  $p_x$ ,  $p_y$  and  $p_z$  are defined along the  $x$ ,  $y$  and  $z$ -axis, respectively. However, it is widely used the transverse momentum  $p_T$  defined by

$$p_T = \sqrt{p_x^2 + p_y^2}. \quad (3.3.2)$$

The pseudorapidity is another important variable used in the ATLAS experiment and it is defined by

$$\eta \equiv \frac{1}{2} \ln\left(\frac{|\vec{P}| + p_z}{|\vec{P}| - p_z}\right). \quad (3.3.3)$$

Since the difference in the pseudorapidity of two particles  $\Delta y$  is independent of Lorentz boosts along the beam axis and, for massless particles, the pseudorapidity coincides with the rapidity  $y$ , the pseudorapidity provides a physically better variable. It can be also written in terms of the polar angle as

$$\eta \equiv -\ln\left(\tan\frac{\theta}{2}\right). \quad (3.3.4)$$

Another variable used is the distance between two particles  $\Delta R$  defined in terms of the difference in the pseudorapidity and the difference in the azimuthal angle between the two particles:

$$\Delta R \equiv \sqrt{\Delta\eta^2 + \Delta\phi^2}. \quad (3.3.5)$$

### 3.3.1 Inner detector

The inner detector, shown in Figure 3.3.2, is a very compact and highly sensitive part of ATLAS and the closest system to the beam pipe allowing the study of

the resultant particles from the  $pp$  collisions. This detector constitutes a tracking system used to the identification and the measurement of the momenta of the charged particles. It also allows the reconstruction of the interaction vertex. It begins a few centimeters close to the proton beam axis and extends to a radius of 2.1 meters and is 6.3 meters in length along the beam pipe. The inner detector has an acceptance in pseudorapidity of  $|\eta| < 2.5$  and full coverage in the azimuthal angle  $\phi$ .

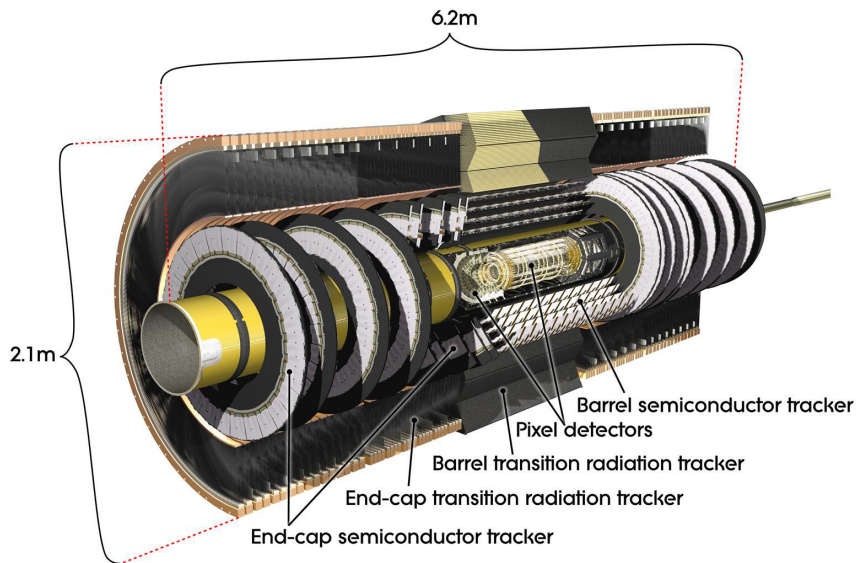


Figure 3.3.2: Representation of the ATLAS inner detector. The pixel detectors refers to the Insertable B-Layer and the Pixel Detector. [73]

Immersed in a 2 T solenoidal magnetic field parallel to the beam axis, it is divided in four different concentric subdetectors named the Insertable B-Layer (IBL), the Pixel Detector (PD), the Semiconductor Tracker (SCT) and the Transition Radiation Tracker (TRT). The Pixel detectors which consist in the IBL and the PD are the innermost part of the inner detector contributing to the accurate measurement of vertices. The PD uses silicon sensors (pixels) composed by three cylindrical layers in the barrel region and three concentric disks in the end-cap region. The SCT is the middle part of the inner detector and is a silicon microstrip detector composed of a barrel, with four layers of silicon microstrip detectors,

and two end-caps, each with nine disks. The TRT is the outermost part the inner detector and consists of 4 mm diameter gaseous straw tubes interleaved with transition radiation material.

Combining the information from the four subdetectors, the transverse momentum resolution measured in the plane perpendicular to the beam axis is [61]

$$\frac{\sigma_{p_T}}{p_T} = \frac{0.05\%}{\text{GeV}} p_T \oplus 1\%. \quad (3.3.6)$$

### 3.3.2 Calorimeters

The ATLAS calorimeter system, shown in Figure 3.3.3, is used to provide an accurate measurement of particles energies by absorbing them and measuring the shower properties, which eases the particle identification. The calorimeters are designed to stop the majority of the particles, except for muons and neutrinos. Each of the calorimeters are divided into a central barrel part and two symmetric end-caps.

The calorimeter system stops most of the particles from arriving to the muon spectrometer preventing them from being identified as muons. Given the neutrinos do not leave any signatures to be observed and do not interact with the detector material, the called missing transverse energy  $E_T^{\text{miss}}$  could be obtained since the four-momentum carried by neutrino implies as unbalance in the total momentum available in the event. The good measurement of  $E_T^{\text{miss}}$  is an important mission in the ATLAS calorimeters since this variable is a crucial discriminant for many physics searches.

The electromagnetic calorimeter force the decay and then measure the energy of the electromagnetic particles which are leptons or photons. The hadronic calorimeter measures the energy deposition from the hadronic showers of high energy hadrons which are protons or neutrons. The components of the calorimetry system are: the Liquid Argon (LAr) electromagnetic calorimeter, the LAr hadronic end-cap calorimeter (HEC), the LAr forward calorimeter (FCal) and the Tile calorimeter (TileCal). The electromagnetic and the hadronic calorimeters cover a region of  $|\eta| < 3.2$  and  $|\eta| < 4.9$ , respectively.

The LAr electromagnetic calorimeter uses liquid argon as active material and lead

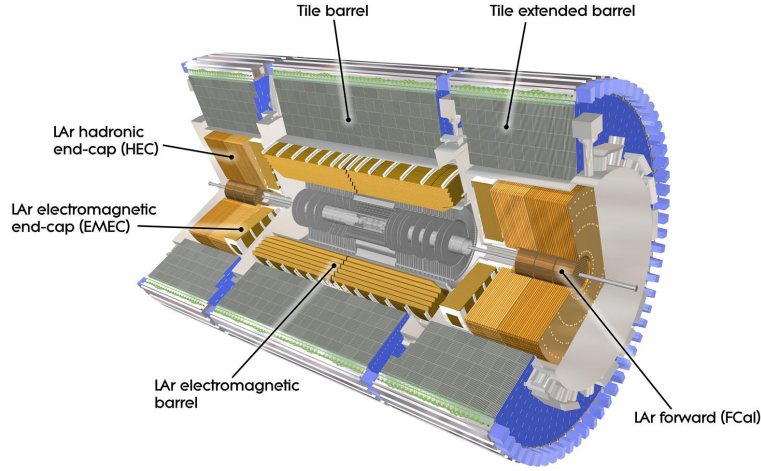


Figure 3.3.3: Open view of the ATLAS calorimeter system.[74]

plates as absorber composing a sampling detector of one barrel and two end-caps. The target energy resolution for the electromagnetic calorimeter is [61]

$$\frac{\sigma_E}{E} = \frac{10\%}{\sqrt{E}} \oplus \frac{17\%}{E} \oplus 0.7\%, \quad (3.3.7)$$

with  $E$  measured in GeV.

The TileCal hadronic calorimeter is also a sampling calorimeter using steel (as absorber material) and scintillating plastic tiles (as active material) placed in one central barrel and two extended barrels. The target energy resolution for the TileCal hadronic calorimeter is [61]

$$\frac{\sigma_E}{E} = \frac{50\%}{\sqrt{E}} \oplus 3\% \quad (3.3.8)$$

with  $E$  measured in GeV.

### 3.3.3 Muon spectrometer

The muon spectrometer, shown in Figure 3.3.4, is a combination of toroidal superconducting magnets and precision chambers designed to detect and measure the



momentum of the muons. As muons minimally interact with the other parts of the detector and have long lifetimes, they are identified and measured in the outermost detector layer. This system is by far the largest tracking system in ATLAS since it extends from a radius of 4.25 m around the calorimeters out to the full radius of the detector (which is 11 m). This detector system covers a region of  $|\eta| < 2.7$ . It is also designed to trigger the muons in the region  $|\eta| < 2.4$ .

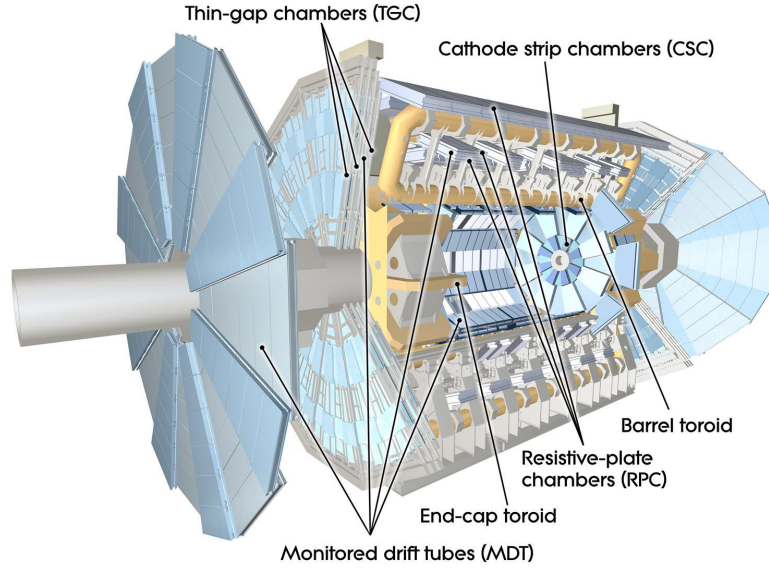


Figure 3.3.4: Representation of the ATLAS muon spectrometer.[75]

It is composed by four distinct chambers: Thin Gap Chambers (TGC), Resistive Plate Chambers (RPC), Monitored Drift Tubes (MDT) and Cathode Strip Chambers (CSC). Due to the magnetic field provided by the toroidal magnets, this subdetectors measure the muons momentum through the measurement of the curvature of the deflected muon trajectory. The muon spectrometer was designed to provide a transverse momentum resolution of [61]

$$\frac{\sigma_{p_T}}{p_T} = 10\% \text{ at } p_T = 1 \text{ TeV.} \quad (3.3.9)$$

### 3.3.4 Magnet system

The ATLAS magnet system allows the measurement of the charged particles momentum and it is designed to provide a field mostly orthogonal to the particle trajectory. It is composed of four large superconducting magnets: one central solenoid magnet, one barrel toroid, and two end-cap toroids.

The central solenoid magnet encloses the inner detector and provides a high magnetic field to bend the trajectory of charged particles allowing the momentum measurement by the tracking system.

The toroidal magnet system is divided in three parts with a barrel part placed around the central calorimeter and two end-caps placed at each end of the detector. Each of these toroidal magnets has eight identical coils built radially in a symmetric way around the beam pipe. The toroidal magnet system provides the magnetic field for additional bending of the muon trajectories in order to measure with precision their momentum in the muon barrel and end-cap spectrometers.

In contrast with the central solenoid magnet which produces a uniform magnetic field of approximately 0.5 T, the magnetic field produced by the toroidal magnets it varies from 0.15 T to 2.5 T [61].

### 3.3.5 Trigger and data acquisition system

The production cross-section of inelastic proton-proton scattering events at the LHC is several orders of magnitude higher than the cross-section of elastic scattering. Consequently, millions of uninteresting collisions happen every second. Besides that, the high collision rate of 40 million events per second at the LHC running conditions does not allow the storage and analysis of all amount of data generated.

To reduce the flow of data to acceptable levels, the ATLAS trigger and data acquisition system selects in real time events with different characteristics that make them interesting for physics analyses. The trigger system works in three stages: the level 1 hardware trigger (L1), the high level software trigger containing the level 2 (L2) and event filter triggers (EF) [61]. In nominal conditions, the

L1, L2 and EF system reduces the event rate to 75 kHz, 3.5 kHz and 200 Hz, respectively.

The collision data samples used in this analysis were collected by the ATLAS detector during 2015. The total integrated luminosity delivered by the LHC in 2015 was  $4.2 \text{ fb}^{-1}$ . However, not all collisions events recorded by ATLAS are used for data analysis. Each subdetector has a record of its performance across the run and only the data collected with all subdetectors working with certain quality requirements are considered. With this information, Good Run Lists (GRL) are created recording which subdetectors satisfied the requirements for each luminosity block. The fraction of data considered as "good" is  $\sim 82\%$ , giving a total integrated luminosity of  $3.21 \text{ fb}^{-1}$  satisfying data quality that is used for this analysis.

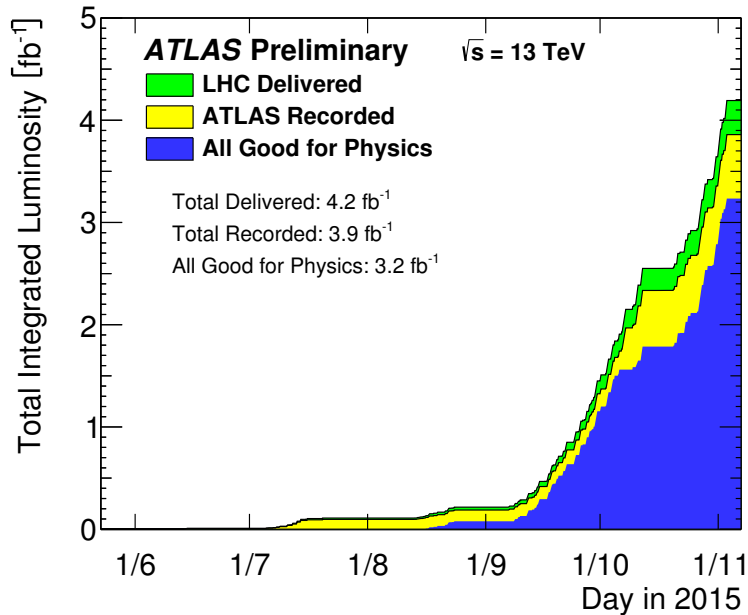


Figure 3.3.5: The total integrated luminosity delivered in the year of 2015 as a function of time [76].

### 3.3.6 Worldwide LHC Computer GRID

The Worldwide LHC Computer GRID (WLCG) is a global network of more than 170 computing centers in 42 countries. With the goal of the distribution around the

globe the data from the LHC experiments, the WLCG is linking up national and international grid infrastructures. This worldwide network is designed to store, organize and analyze the  $\sim 30$  Petabytes of data annually generated at the LHC [77]. The WLCG is divided in different layers, called tiers, each one with distinct purposes.

The Tier 0 is the CERN data Centre located in Geneva and also at the Wigner Research Centre for Physics in Budapest. The two sites are connected by two dedicated 100 Gigabit/s data links. The Tier 0 is responsible for the safe-keeping of raw data, first pass reconstruction, distribution of raw data and reconstruction output to the Tier 1.

The Tier 1 is composed by thirteen large computer centres. They are responsible for the safe-keeping of a proportional share of raw and reconstructed data, large-scale reprocessing and safe-keeping of corresponding output, distribution of data to Tier 2 and safe-keeping of a share of simulated data produced at these Tier 2. The Tier 2 is composed by around 160 sites typically located at universities and other scientific institutes. This sites can store data and provide computing power for specific analysis tasks. The individual scientists can access and process the data through the Tier 3 computing resources consisting of local clusters.

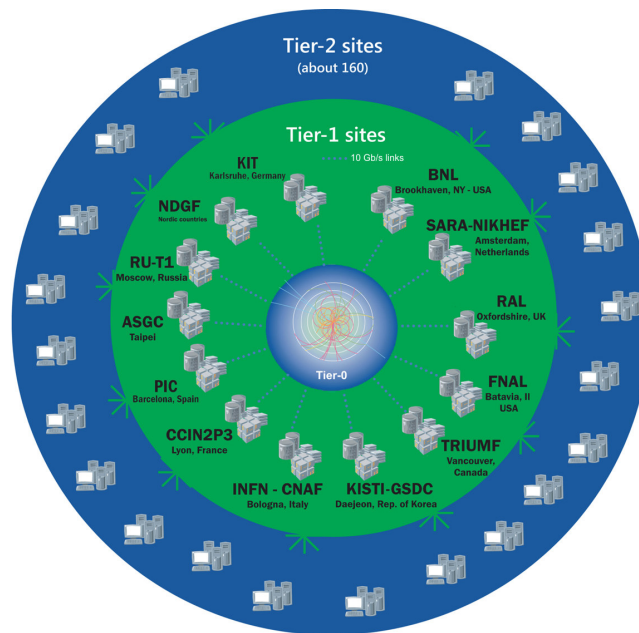


Figure 3.3.6: Representation of the structure of the tiers 0, 1 and 2. The various locations of the thirteen computer centres of tier 1 can also be found [78].



# Chapter 4

## Event analysis

This chapter presents the search analysis focused on the top FCNC process where a top quark and a neutral  $Z$  boson is produced. A trileptonic topology with three leptons, two charged leptons coming from the decay of the  $Z$  boson and one charged lepton along with one neutrino coming and one  $b$ -tagged jet from the decay of the top quark is considered. This topology was chosen since the final state consists in a clear signature of three leptons and just one jet [79]. The consequent loss in acceptance are compensated with the gain in efficiency. An overview of the analysis is presented taking in account the objects definition, data and Monte Carlo (MC) simulation samples, analysis strategy and systematic uncertainties. The analysis presented in this thesis uses the A++ code as analysis code which was developed by the Humboldt University group in Berlin [80].

### 4.1 Data sample and triggers

The data sample analyzed in this search was collected with the ATLAS detector in proton-proton collisions at a centre-of-mass energy of 13 TeV between July and November of 2015. A total integrated luminosity of  $3.21 \text{ fb}^{-1}$  was recorded after requiring all subdetectors to be fully operational during the data taking.

The analyzed events are selected using single electron and muon triggers with different  $p_T$  thresholds and then are combined in a logical OR in order to increase

the overall efficiency [81]. The single electron triggers used are HLT\_e60\_1hmedium and HLT\_e120\_1hloose. Beside these, HLT\_e24\_1hmedium\_L1EM20VH for data and HLT\_e24\_1hmedium\_L1EM18VH for MC triggers are used where the only difference is due to the transverse energy threshold of the electromagnetic cluster. The single muon triggers used are HLT\_mu20\_iloose\_L1MU15 and HLT\_mu50 [82]. The  $p_T$  thresholds are 24 or 60 GeV for the electron triggers and 20 or 50 GeV for the muon triggers. In order to share information, a process named triggers match is performed where a geometrical acceptance is applied to the triggers information with a chosen  $\Delta R$ . Due to the precise momentum measurement and the low misidentification rate, muons are the objects best able to be measured and provide an excellent trigger matching.

## 4.2 Objects definition

The physics objects studied in this analysis are electrons, muons and hadronic jets including  $b$ -tagged jets.

Electron candidates [83] are reconstructed from energy deposits in the electromagnetic calorimeter that are matched with tracks in the inner detector. Only electron candidates with  $p_T > 25$  GeV in the central region defined by the range  $|\eta_{cluster}| < 2.47$  ( $|\eta_{cluster}|$  corresponds to the pseudorapidity of the cluster associated with the electron candidate) are selected. There are three electron identification selections: Medium, Loose and Tight to the specific needs of different physics analyses. In this analysis, electrons candidates must satisfy tight quality criteria.

Muon candidates [84] are reconstructed from tracks in the layers of the muon spectrometer which matched with the corresponding tracks in the inner detector. Only muon candidates with  $p_T > 25$  GeV and  $|\eta| < 2.5$  are selected. A longitudinal impact parameter with respect to the interaction point smaller than 2 mm is required to ensure that the muon candidate is a muon produced in the collisions and not cosmic muons. Concerning the muon reconstruction, there are four identification selections: Medium, Loose, Tight and High- $p_T$ . Loose, Medium and Tight are inclusive categories where muons identified with tighter requirements are also



included in the looser categories. In this analysis, muon candidates must satisfy tight quality criteria.

Jets are reconstructed using the anti- $k_t$  algorithm [85, 86, 87] with a radius parameter of  $\Delta R=0.4$  using calibrated topological clusters built from energy deposits in the hadronic calorimeter. The calibration of topological clusters [88, 89] is made to correct the cluster energy for the effects of non-compensation, dead material and out-of-cluster leakage. The corrections are obtained through simulation of neutral and charged particles. During the jets reconstruction electrons and hadronic energy deposition can not be distinguish. To remove this overlap between electrons and jets, any jet identified within a cone of radius  $\Delta R < 0.2$  is excluded. After that, any remaining electrons or muons within a radius of  $\Delta R < 0.4$  of a select jet are excluded. After energy calibration [90], only jets that satisfy  $p_T > 30$  GeV and  $|\eta| < 2.5$  are selected.

The identification of jets coming from the bottom quark, known as  $b$ -tagged jets, is made using the MV2c20 algorithm. The MV2c20 algorithm uses a boosted decision tree algorithm to discriminate  $b$ -jets from light ( $u,d,s$ -quark or gluon jets) where the training is performed on a set of around 5 million  $t\bar{t}$  events. With a total of 24 input variables, this  $b$ -tagging algorithm takes into account parameters like transverse momentum, pseudorapidity, invariant mass of tracks and distances between others. Through a cut on the MV2 output distribution, the  $b$ -tagging algorithm is characterized by different operating points. The operating points are calibrated in a sample of simulated  $t\bar{t}$  events and provide a specific  $b$ -tagging efficiency of 60%, 70%, 77% or 85% [91]. The performance of the  $b$ -tagging algorithm is affected by the capability to correctly identify jets coming from a real  $b$ -quark compared to the probability of mistakenly  $b$ -tagging a jet originating from a  $c$ -quark or a light-flavour parton ( $u,d,s$ -quark or gluon). The  $b$ -tagging efficiencies with the  $c$ -jet and light-jets rejection rates are presented in Table 4.2.1.

<b><math>b</math>-jet efficiency</b>	<b><math>c</math>-jet rejection</b>	<b>Light-jet rejection</b>
60%	21	1900
70%	8.1	440
77%	4.5	140
85%	2.6	28

Table 4.2.1: Operating points for the MV2c20  $b$ -tagging algorithm including the  $c$ -jet and light-jets rejection rates [91].

For the analysis presented in this thesis, the operating point used is the one with a jet efficiency of 77% due to the reasonable balance between the efficiency of the identification of  $b$ -jets and the rejection of light quarks. The tagging efficiency to  $b$ ,  $c$  and light-flavour jets for the MV2c20 algorithm with the 77% operating point as a function of jet  $p_T$  and  $|\eta|$  are presented in Figure 4.2.1.

(a)

(b)

Figure 4.2.1: The efficiency to tag  $b$  (green),  $c$  (blue) and light-flavour (red) jets for the MV2c20 tagger with the 77% working point. Efficiencies are shown as a function of the jet (a)  $p_T$  and (b)  $|\eta|$  [92, 93].

### 4.3 Analysis strategy

The strategy of this analysis consists in a set of requirements taking into account the final state of  $tZ$  production via FCNC. The  $tZ$  production via FCNC consists in the production of a  $Z$  boson which decays to two leptons, the production of a top quark which decays to a  $W$  boson and a bottom quark. The final state is characterized by two leptons coming from the  $Z$  boson, one charged lepton and one neutral lepton (neutrino) coming from the  $W$  boson decay and one  $b$ -tagged jet coming from the hadronisation of a bottom quark.

At the first selection level is required that events contain, exactly, one jet and three leptons. In the next selection level, the events without a  $Z$  boson candidate are excluded. The two leptons with higher  $p_T$  are used to reconstruct the  $Z$  boson candidate. The  $Z$  boson candidates are reconstructed with a pair of Opposite-Sign Same-Flavour (OSSF) leptons (electrons or muons) with a invariant mass higher than 70 GeV and lower than 110 GeV (which are around 20 GeV of difference from the measured  $Z$  boson mass 91.19 GeV [5]). In the case of two  $Z$  bosons reconstructed, the candidate with the mass closest to 91.19 GeV is selected. The lepton not chosen as coming from the decay of the  $Z$  boson is used to reconstruct the decay of the  $W$  boson. It is assumed that the  $W$  boson decays leptonically, having a charged and a neutral lepton as final state. Figure 4.3.1 shows the lepton multiplicity and the three leptons  $p_T$  distributions after requiring events with exactly one jet. The filled region corresponds to the multiple background processes predictions and the solid line is the signal hypothesis for the  $tZ$  production through FCNC processes.

Figure 4.3.1 (a) shows the lepton multiplicity. The signal sample has more events in the regions with two and three leptons, which corresponds to the  $W$  boson decaying hadronically and leptonically, respectively. In the dileptonic region the background is defined by the  $Z$ +jets and dibosons processes. However, in the trileptonic region the background corresponds mainly to the diboson processes. In this analysis, it is studied the process where the  $W$  boson decays leptonically.

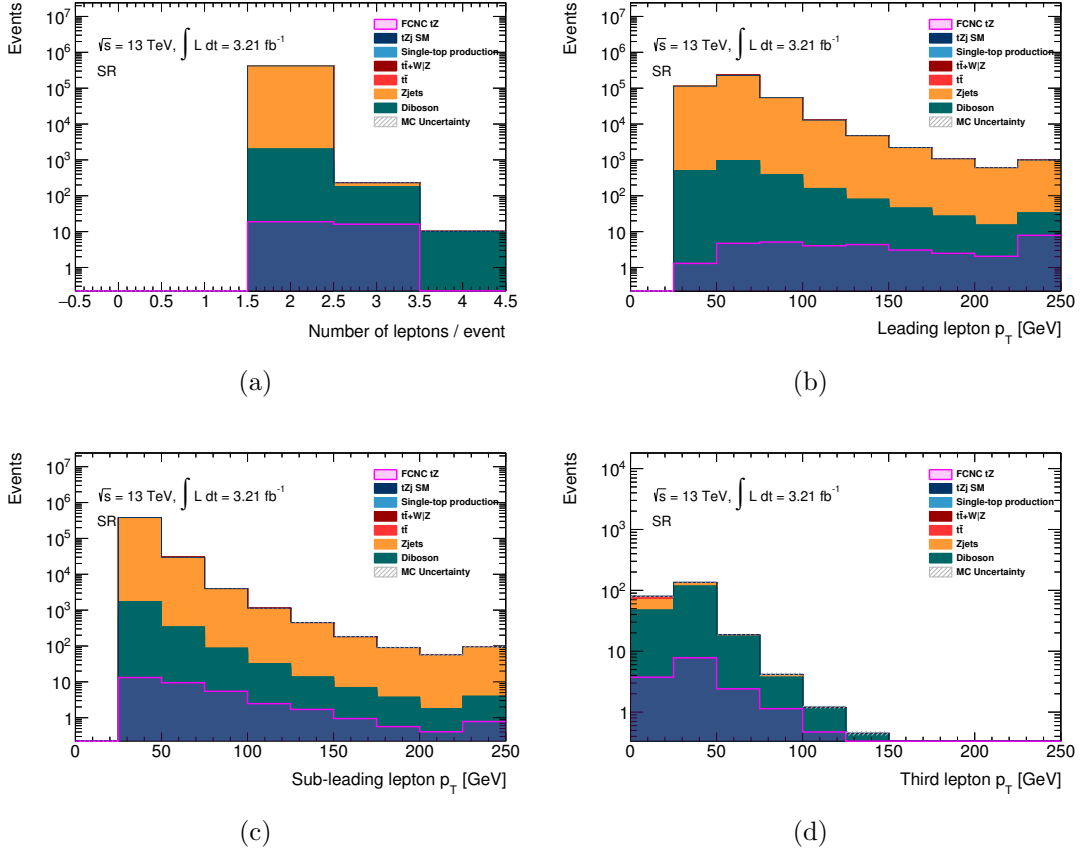


Figure 4.3.1: Distributions of (a) lepton multiplicity, (b) leading lepton  $p_T$ , (c) sub-leading lepton  $p_T$  and (d) third lepton  $p_T$  after require exactly one jet.

Figures 4.3.1 (b), (c) and (d) shows the  $p_T$  distributions for the three leptons where just the requirement of exactly one jet are applied. The  $p_T$  distributions indicates that the requirement of three leptons decrease the majority of background events mainly in the  $Z + \text{jets}$  processes as expected. These distributions also shows that the fakes in the  $Z + \text{jets}$  background should not be a problem for this analysis.

After the cuts on the jet and the lepton multiplicity and the reconstruction of  $Z$  boson candidate, is required that the jet considered is only selected if it is a  $b$ -tagged jet. The  $b$ -tagged jet along with the  $W$  boson decay are considered being from the decay of the top quark. Figure 4.3.2 shows the  $b$ -tagged jet multiplicity after requiring one jet and three leptons.

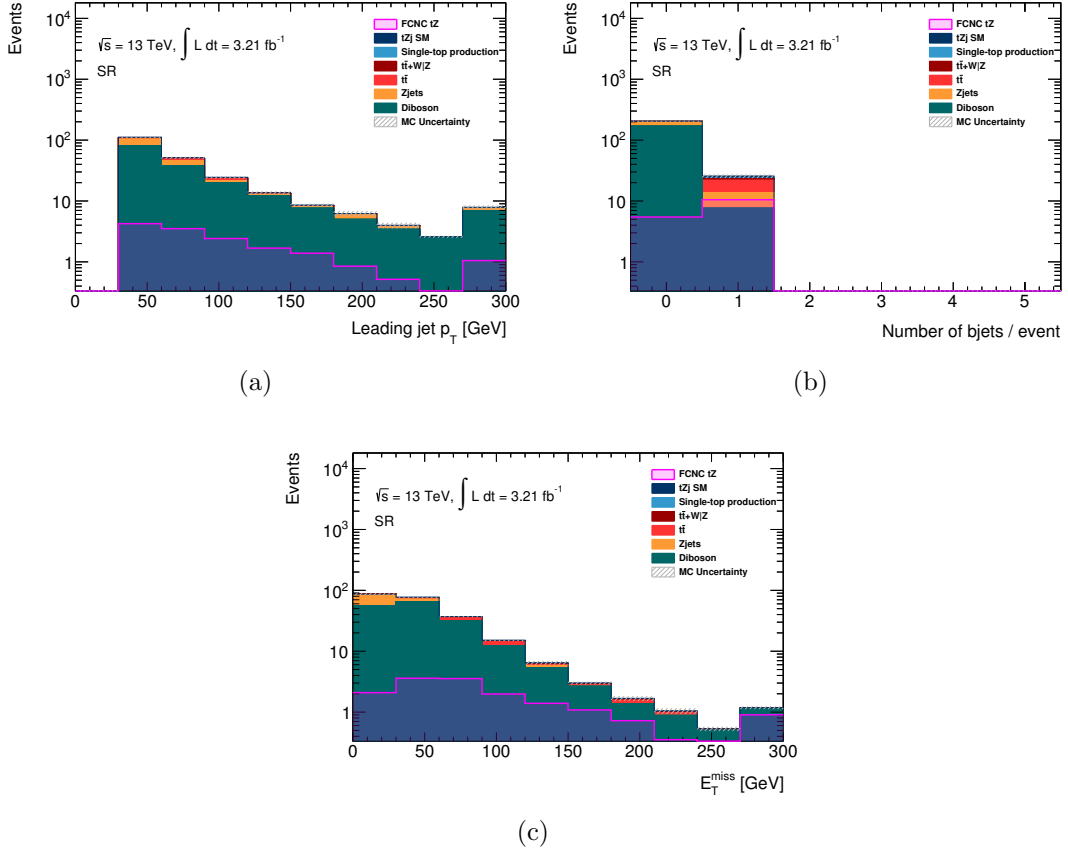


Figure 4.3.2: Distributions of (a) leading jet  $p_T$ , (b)  $b$ -tagged jet multiplicity and (c)  $E_T^{\text{miss}}$  after require exactly one jet and three leptons.

Figure 4.3.2 (a) shows the leading jet  $p_T$  distribution. Both signal and background distributions has the same behavior. Figure 4.3.2 (b) shows the  $b$ -tagged jet multiplicity. The number of signal events increases in the region with exactly one  $b$ -tagged jet where the dibosons background dominates with a presence of  $Z$ +jets,  $t\bar{t}$  and  $tZj$  SM backgrounds in a small fraction. Figure 4.3.2 (c) shows the  $E_T^{\text{miss}}$  distribution. The highest value for this variable in the signal simulation is between 50 and 100 GeV which is consistent with the hypothesis of having one neutrino in the final state.

## 4.4 Signal modeling

Monte Carlo samples of LO  $tZ$  production through FCNC were generated with MADGRAPH5\_AMC@NLO [94] interfaced with PYTHIA [95] for parton shower and fragmentation through the TOPFCNC Universal FeynRules Output (UFO) model [47]. The cross-section multiplied by the branching ratio is arbitrary chosen to have a normalisation of 0.1 pb.

## 4.5 Background modeling

Several SM processes have the same final state particles as the signal events and are considered as a background to the FCNC analysis. The backgrounds studied in this analysis are:

- Dibosons ( $WW$ ,  $WZ$  and  $ZZ$ );
- $Z$  + jets;
- $t\bar{t}$ ;
- $t\bar{t} + W/Z$ ;
- Single top ( $Wt$ -channel);
- $tZj$ .

The dibosons samples corresponding to  $WW$ ,  $WZ$  and  $ZZ$  have been generated using POWHEG\_BOX [96] interfaced with PYTHIA.

The  $Z$ +jets samples have been generated using POWHEG\_BOX interfaced with PYTHIA.

The  $t\bar{t}$  samples have been generated using POWHEG\_BOX interfaced with PYTHIA. The  $t\bar{t} + W/Z$  samples have been generated using MADGRAPH5\_AMC@NLO interfaced with PYTHIA.

The Single top sample corresponding to  $Wt$ -channel have been generated using POWHEG\_BOX interfaced with PYTHIA.

The  $tZj$  sample have been generated using MADGRAPH5\_AMC@NLO interfaced with PYTHIA.

The background processes described are simulated in multiple MC samples which cross-sections and generators used are shown in Table 4.5.1.

Process	$\sigma$ (pb)	Generator
$WW \rightarrow l\nu l\nu$	10.631	POWHEG_BOX + PYTHIA
$WZ \rightarrow l\nu ll$	4.462	POWHEG_BOX + PYTHIA
$WZ \rightarrow qqll$	3.285	POWHEG_BOX + PYTHIA
$ZZ \rightarrow ll ll$	1.257	POWHEG_BOX + PYTHIA
$ZZ \rightarrow l\nu l\nu$	0.925	POWHEG_BOX + PYTHIA
$ZZ \rightarrow qqll$	2.274	POWHEG_BOX + PYTHIA
$Z \rightarrow ee$	1950.63	POWHEG_BOX + PYTHIA
$Z \rightarrow \mu\mu$	1950.63	POWHEG_BOX + PYTHIA
$Z \rightarrow \tau\tau$	1950.63	POWHEG_BOX + PYTHIA
$t\bar{t}$	451.664	POWHEG_BOX + PYTHIA
$t\bar{t} + W$	0.221	MADGRAPH5_AMC@NLO + PYTHIA
$t\bar{t} + W$	0.176	MADGRAPH5_AMC@NLO + PYTHIA
$t\bar{t} + W$	0.171	MADGRAPH5_AMC@NLO + PYTHIA
$t\bar{t} + Z$	0.013	MADGRAPH5_AMC@NLO + PYTHIA
$t\bar{t} + Z$	0.023	MADGRAPH5_AMC@NLO + PYTHIA
$t\bar{t} + Z$	0.013	MADGRAPH5_AMC@NLO + PYTHIA
$t\bar{t} + Z$	0.023	MADGRAPH5_AMC@NLO + PYTHIA
$t\bar{t} + Z$	0.013	MADGRAPH5_AMC@NLO + PYTHIA
$t\bar{t} + Z$	0.024	MADGRAPH5_AMC@NLO + PYTHIA
$Wt$ Channel	35.845	POWHEG_BOX + PYTHIA
$tZj$	0.240	MADGRAPH5_AMC@NLO + PYTHIA

Table 4.5.1: Background MC samples with the corresponding cross-sections and generators used in the analysis presented in this thesis.

## 4.6 Signal region definition

After the sensitivity study made in Section 4.3, the event selection for the signal region chosen consists in the requirement of exactly three leptons, at least one OSSF pair of leptons and, finally, exactly one  $b$ -tagged jet. The requirement of three leptons allows a clean signature implying the exclusion of the majority of events. The analysis presented in this thesis has blinded according to ATLAS blinding policy which means that the data in the signal region is not shown until the analysis strategy is well based and the background behavior is fully understood. Figure 4.6.1 shows some distributions of important variables after the event selection.

The jet multiplicity represented in Figure 4.6.1(a) shows the same behavior seen in the  $b$ -tagged jet multiplicity shown in Figure 4.6.1 (b). Comparing the plots for the two levels of the selection, it is clear the importance of the cut on the  $b$ -tagged jet multiplicity in the number of events selected. This cut decreases the number of background events in a factor of 10. The total of  $\sim 20$  background events, after the cut on the  $b$ -tagged jet multiplicity, are divided in dibosons,  $Z$ +jets,  $t\bar{t}$ ,  $t\bar{t}+W/Z$  and  $tZj$  processes. Figure 4.6.1(b) indicates that the region with one jet that is not an  $b$ -tagged jet is dominated by the dibosons background as expected. The  $E_{\text{T}}^{\text{miss}}$  distribution for the signal region represented in Figure 4.6.1(c) reveals a different behavior for signal and background. While the majority of the backgrounds have a softer distribution, the signal has a harder distribution of  $E_{\text{T}}^{\text{miss}}$  which is compatible with a neutrino in the final state. The difference between background and signal is better for the plot after the  $b$ -tagging requirement.

Figure 4.6.1(d) shows the mass of the  $Z$  boson candidate. This distribution shows the  $Z$  boson candidate mass peak close to the measured mass even with a low statistics. Figure 4.6.2(a) shows the  $p_{\text{T}}$  distribution of the  $Z$  boson candidate which is very different for signal and background. The signal events have a harder distribution compared with all the background processes, which can be used for a discriminant variable in the future.



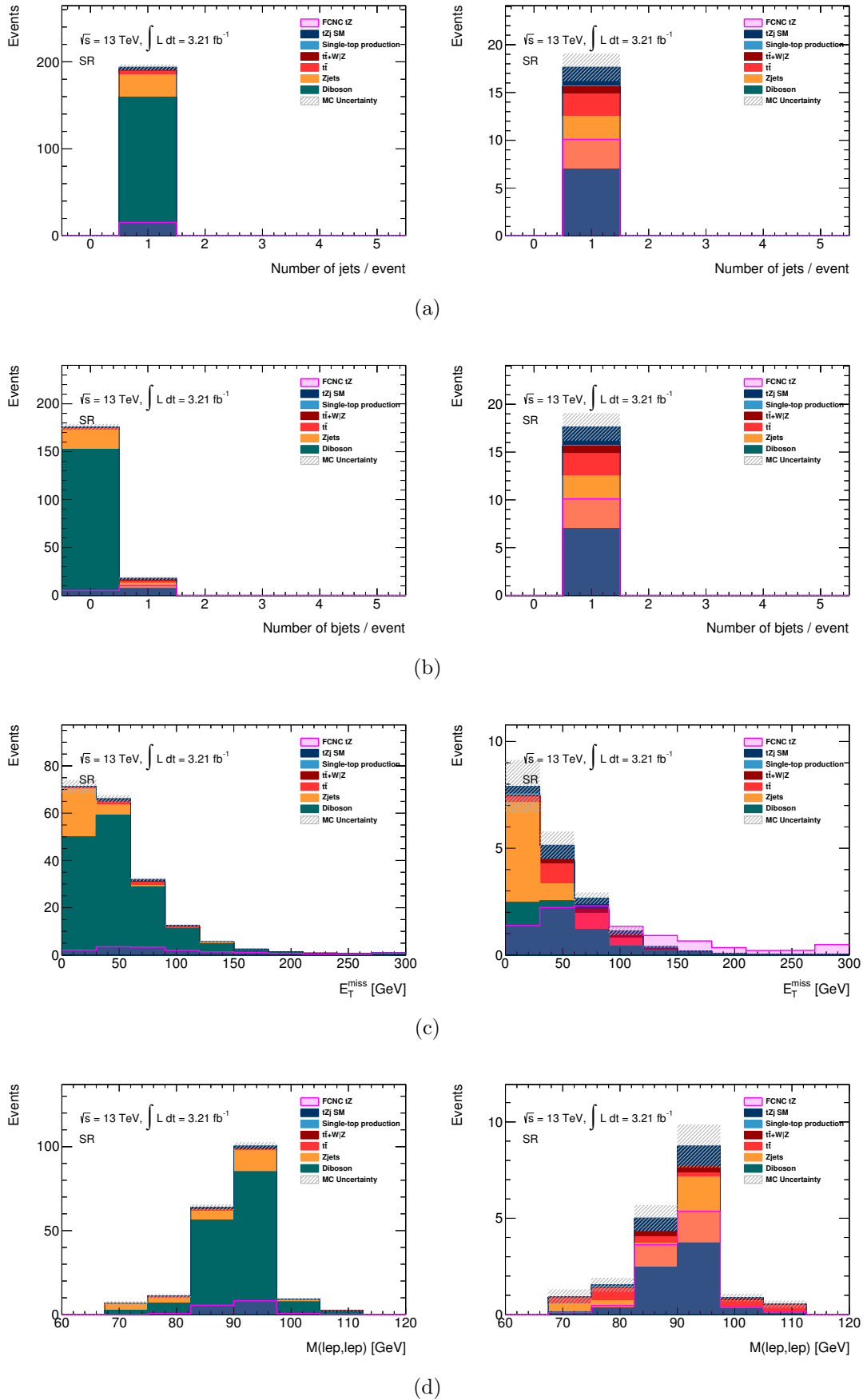


Figure 4.6.1: Signal region distributions of (a) jet multiplicity, (b)  $b$ -tagged jet multiplicity, (c)  $E_T^{\text{miss}}$  and (d)  $Z$  boson candidate mass before (left) and after (right) the  $b$ -tagged jet requirement.

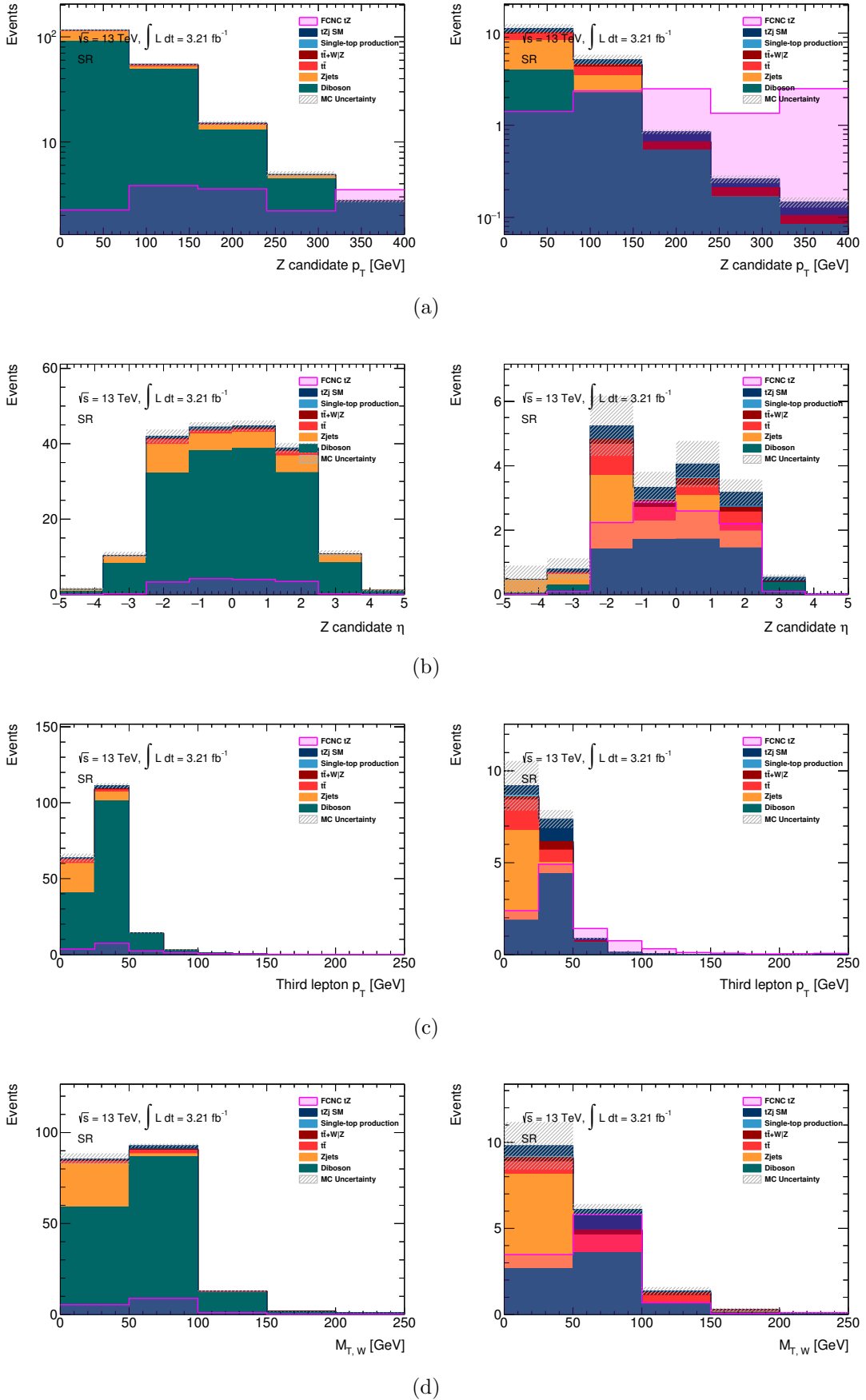


Figure 4.6.2: Signal region distributions of (a)  $Z$  boson candidate  $p_T$ , (b)  $Z$  boson candidate  $\eta$ , (c) third lepton  $p_T$  and (d) transverse mass of the  $W$  boson before (left) and after (right) the  $b$ -tagged jet requirement.

The  $Z$  boson candidate  $\eta$  represented in Figure 4.6.2(b) shows the majority of events located in the region where  $\eta$  is zero. The third lepton  $p_T$  distribution shown in Figure 4.6.2(c) is characterized by a harder distribution for the signal events when compared with the background processes. This distribution shows the behavior of a possible distribution variable. In Figure 4.6.2(d), the transverse mass of the  $W$  boson is shown. This observable is computed considering the lepton associated with the  $W$  boson and the missing transverse energy ( $E_T^{\text{miss}}$ ):

$$M_T(W) = \sqrt{(E_T^l + E_T^{\text{miss}})^2 - (p_x^l + p_x^{\text{miss}})^2 - (p_y^l + p_y^{\text{miss}})^2} \quad (4.6.1)$$

Both distributions of this observable, before and after the  $b$ -tagging requirement, shows the signal events located in the region between 50 and 100 GeV. This behavior is consistent with one neutrino in the final state which is the case for the signal of this analysis. Along with the  $Z$  boson candidate  $p_T$ , this observable can be a variable used to discriminate signal and background events.

The events yields to the signal region after the selection are shown in Table 4.6.1. The number of events in the total background are the sum of the number of events for all background processes.

Process	Signal
FCNC $tZ$	$10.10 \pm 0.37$
SM $tZj$	$1.94 \pm 0.04$
Single Top	$0.08 \pm 0.05$
$t\bar{t} + W/Z$	$0.77 \pm 0.01$
$t\bar{t}$	$2.36 \pm 0.45$
$Z + \text{jets}$	$5.47 \pm 1.35$
Dibosons	$7.00 \pm 0.21$
Total background	$17.63 \pm 1.44$

Table 4.6.1: Signal region event yields after the selection criteria. The uncertainties presented corresponds only to the statistical errors.

## 4.7 Comparison between data and prediction

The selection criteria for the analysis of this thesis was presented in Section 4.3. This section shows the comparison between the data events with an integrated luminosity of  $3.21 \text{ fb}^{-1}$  recorded with a centre-of-mass energy of  $\sqrt{s} = 13 \text{ TeV}$  at the ATLAS detector and the MC prediction for the different processes.

### 4.7.1 Validation regions

Beside the signal region, multiple control regions are defined. While the signal region is targeted to provide the signal sensitivity, the control regions are defined to validate the background processes. The following regions are studied:

- $Z$  + jets in a dileptonic topology;
- $Z$  + jets in a trileptonic topology;
- $t\bar{t}$  in a trileptonic topology;
- Diboson, specifically the  $WZ$  process, in a trileptonic topology;
- $tZj$  in a trileptonic topology.

Table 4.7.1 summarizes the event selection of the different control regions.

$Z$ +jets 2L CR	$Z$ +jets 3L CR	$t\bar{t}$ CR	WZ Diboson CR	$tZj$ CR
= 2 leptons	= 3 leptons	= 3 leptons	= 3 leptons	= 3 leptons
-	-	$E_T^{miss} > 20 \text{ GeV}$	-	$E_T^{miss} > 20 \text{ GeV}$
-	-	$M_T(W) > 40 \text{ GeV}$	-	-
$\geq 1$ OSSF Pair	$\geq 1$ OSSF Pair	$\geq 1$ OSSF Pair	$\geq 1$ OSSF Pair	$\geq 1$ OSSF Pair
$70 \text{ GeV} < M(\ell\ell)$	$70 \text{ GeV} < M(\ell\ell)$	$M(\ell\ell) < 80 \text{ GeV}$	$81 \text{ GeV} < M(\ell\ell)$	$70 \text{ GeV} < M(\ell\ell)$
$M(\ell\ell) < 110 \text{ GeV}$	$M(\ell\ell) < 110 \text{ GeV}$	$M(\ell\ell) > 100 \text{ GeV}$	$M(\ell\ell) < 101 \text{ GeV}$	$M(\ell\ell) < 110 \text{ GeV}$
$\geq 1$ Jet	$\geq 1$ Jet	= 2 Jets	= 1 Jet	$\geq 1$ Jet
= 1 $b$ -tagged jet	= 1 $b$ -tagged jet	= 1 $b$ -tagged jet	-	= 1 $b$ -tagged jet

Table 4.7.1: Selection criteria used to define the considered control regions.

The selection of the  $Z$ +jets control region, taking into account the dileptonic topology, consists in the requirement of exactly two leptons, at least one OSSF

pair of leptons with a reconstructed mass between 70 and 110 GeV and at least one jet where one is an  $b$ -tagged jet.

Figure 4.7.1 shows some distributions to the dileptonic  $Z$ +jets control region. Figure 4.7.1(a) shows the  $Z$  boson candidate mass distribution, having a good agreement between data and MC, with the mass peak in the value of  $\sim 91$  GeV (close to the measured  $Z$  boson mass). The  $p_T$  distribution of the  $Z$  boson candidate, shown in Figure 4.7.1(b), is characterized by low values of this variable mainly localized in the range of 0 and 150 GeV. In Figure 4.7.1(c), the comparison between data and MC reveals a good agreement in the  $\eta$  distribution of the  $Z$  boson candidate. The agreement is better before the  $b$ -tagging requirement.

The jet multiplicity in Figure 4.7.1(d) shows an excellent agreement in the region with one jet before and after the  $b$ -tagging requirement. In the region with two jets, the agreement is not so good and gets worse after requiring the  $b$ -tagged jet. Since the normalisation is worse in the region with more than one jet and the signal region requires exactly one jet, the disagreement between data and MC will not be significant. The  $b$ -tagged jet multiplicity represented in Figure 4.7.2 is characterized by a better data and MC agreement in the region without  $b$ -jets when compared with the region with one  $b$ -tagged jet. This behavior is compatible in both distributions (before and after the  $b$ -tagging requirement). Knowing from Figure 4.7.1(d) that the agreement between data and MC is reasonable in the region with exactly one jet, this not so good agreement in the  $b$ -tagged jet multiplicity should not affect the analysis. Since the  $Z$ +jets processes does not have  $b$ -quarks in the final state, it is expected that the majority of the number of events are excluded after the requirement of one  $b$ -tagged jet.

The events yields for the control region of  $Z$ +jets background, in a dileptonic topology, after the selection are shown in Table 4.7.2. The number of events observed that can be seen in Table 4.7.2 corresponds to the data events.

The  $Z$ +jets dileptonic control region selection allowed a good isolation of this background having a total of  $\sim 29000$   $Z$ +jets events against  $\sim 32000$  background events.

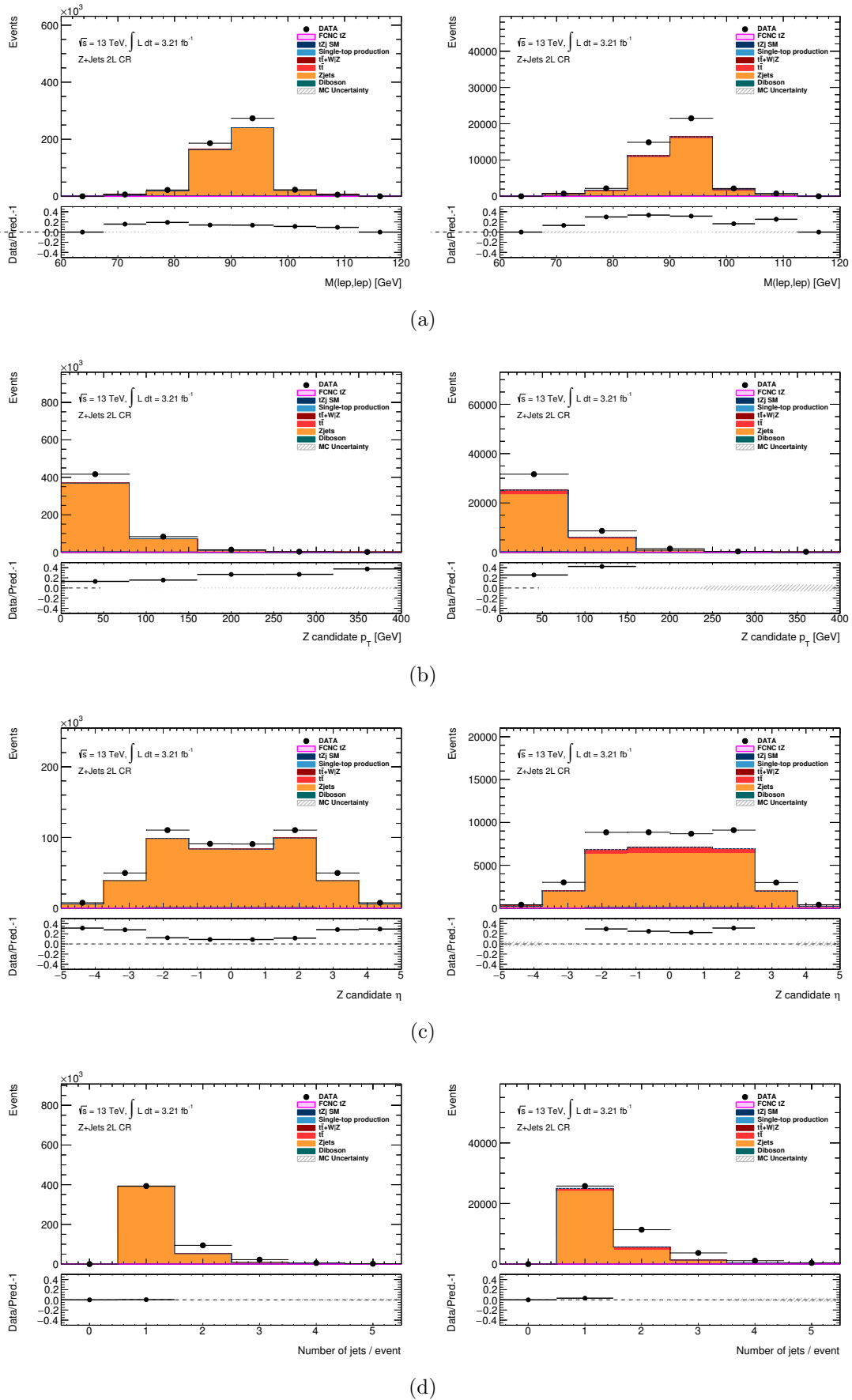


Figure 4.7.1:  $Z$ +jets dilepton control region distributions of (a)  $Z$  boson candidate mass, (b)  $Z$  boson candidate  $p_T$ , (c)  $Z$  boson candidate  $\eta$  and (d) jet multiplicity before (left) and after (right) the  $b$ -tagged jet requirement.

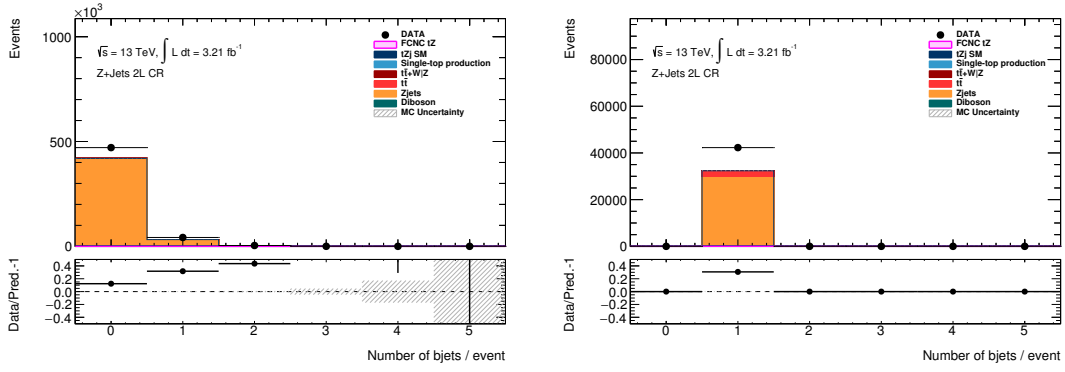


Figure 4.7.2:  $Z$ +jets dilepton control region distributions of  $b$ -tagged jet multiplicity before (left) and after (right) the  $b$ -tagged jet requirement.

Process	$Z$ +jets 2L CR
FCNC $tZ$	$26.64 \pm 0.60$
SM $tZj$	$19.23 \pm 0.13$
Single Top	$141.74 \pm 1.96$
$t\bar{t} + W/Z$	$22.00 \pm 0.08$
$t\bar{t}$	$2\,751.23 \pm 15.43$
$Z + \text{jets}$	$29\,064.40 \pm 117.12$
Dibosons	$355.76 \pm 4.74$
Total background	$32\,354.37 \pm 118.24$
Observed	42 281

Table 4.7.2:  $Z$ +jets dilepton control region event yields after the selection criteria. The uncertainties presented corresponds only to the statistical errors.

Analyzing the number of data events, the conclusion is that a not so good agreement between data and prediction is obtained for this control region, specifically in the region with more than one jet. This difference in the number of events can be explained by the  $Z$ +jets background normalisation that will be corrected after a fit.

The selection of the  $Z$ +jets control region considering a trileptonic topology is the same as for the dileptonic case but it requires exactly three leptons instead of two. The control region considered here allows the study of the significance of the fakes on the  $Z$ +jets processes since this process has only two leptons in the final state. Figures 4.7.3 and 4.7.4 show some distributions for the trileptonic  $Z$ +jets control region.

Figure 4.7.3(a) represents the  $Z$  boson candidate mass distribution with a peak in the true value of the  $Z$  boson mass and a good agreement between data and MC, even with a lot less events than the dileptonic  $Z$ +jets region. The  $p_T$  distribution shown in Figure 4.7.3(b) reveals again a softer distribution of background compared with the signal. Figure 4.7.3(c) shows the  $Z$  boson candidate  $\eta$  where a good agreement between data and MC exists before the  $b$ -tagging requirement but not so good after. The jet multiplicity can be found in Figure 4.7.3(d) having a big fraction of dibosons background what is expected since, in this topology, the  $Z$ +jets will be characterized by fakes. However, the  $Z$ +jets background has a reasonable number of events after all the selection criteria. The  $b$ -tagged jet multiplicity distribution represented in Figure 4.7.4 shows a reasonable data and MC agreement in both distributions. This agreement is a little better for the distributions after the  $b$ -tagging requirement. Due to the low statistics of this control region, the number of events for signal increases while the number of the dominant background (which corresponds to dibosons) decreases after the  $b$ -tagging requirement.

The events yields for the control region of  $Z$ +jets background, in a trileptonic topology, after the selection are shown in Table 4.7.3. Table 4.7.3 shows a not so good isolation of  $Z$ +jets background where the dibosons is the dominant process. However, the  $Z$ +jets is the third background with highest number of events, having  $\sim 6$  of the total of  $\sim 37$  background events. This behavior allows to conclude that the fakes do not affect on a significant way this analysis since the processes with three real leptons in the final state still dominate the background event yields. A reasonable agreement between data and prediction is achieved even with a low statistics after all the selection criteria for the control region considered.



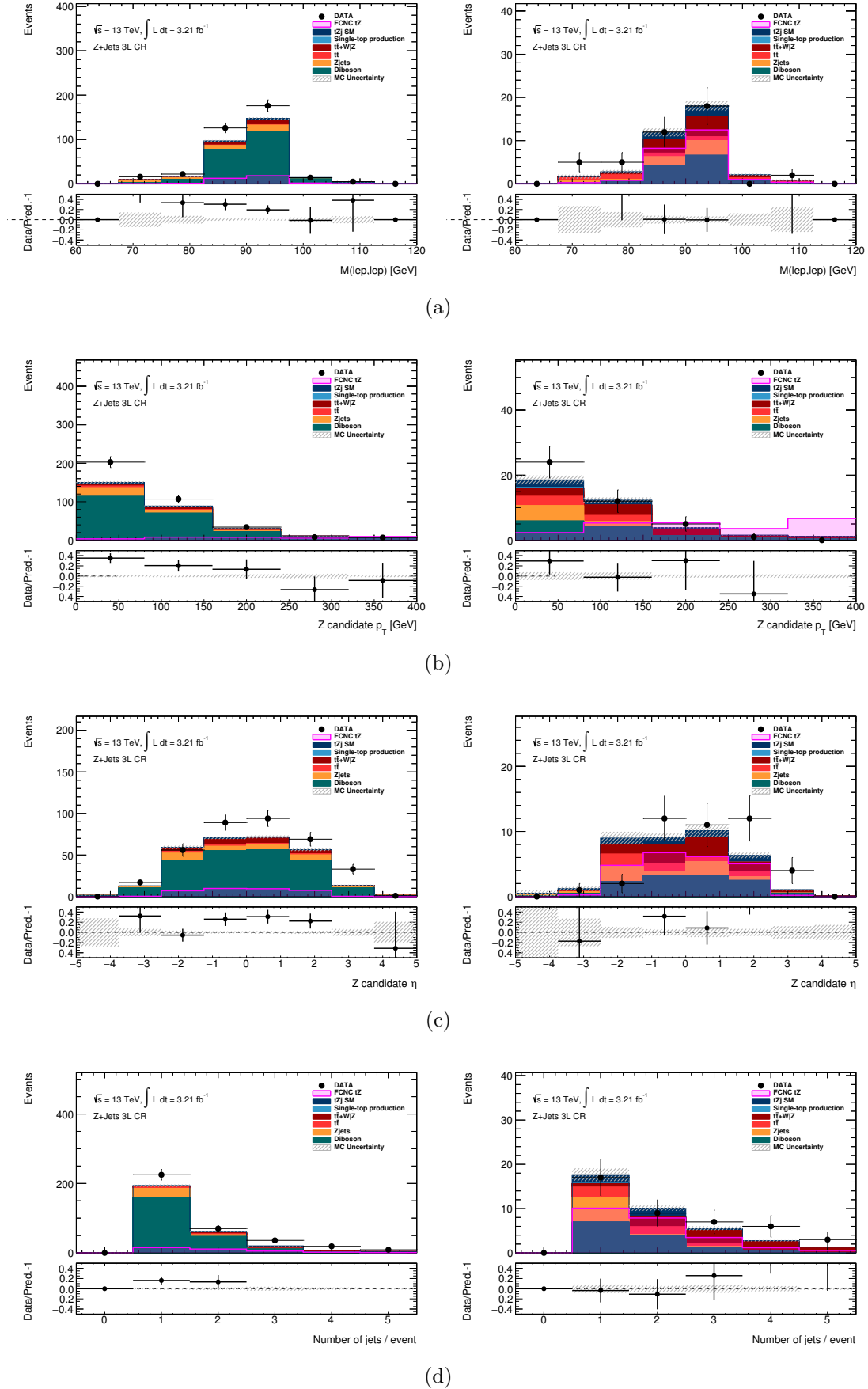


Figure 4.7.3:  $Z$ +jets triplepton control region distributions of (a)  $Z$  boson candidate mass, (b)  $Z$  boson candidate  $p_T$ , (c)  $Z$  boson candidate  $\eta$  and (d) jet multiplicity before (left) and after (right) the  $b$ -tagged jet requirement.

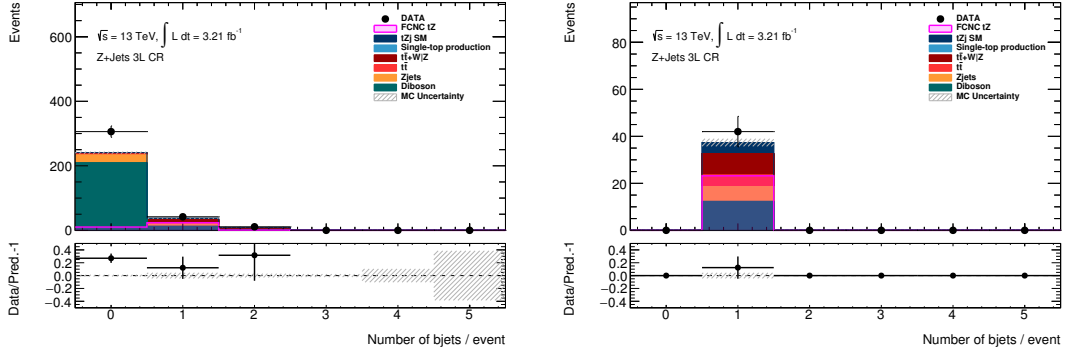


Figure 4.7.4:  $Z$ +jets trilepton control region distributions of  $b$ -tagged jet multiplicity before (left) and after (right) the  $b$ -tagged jet requirement.

Process	$Z$ +jets 3L CR	
FCNC $tZ$	$23.19 \pm$	$0.56$
SM $tZj$	$4.67 \pm$	$0.06$
Single Top	$0.14 \pm$	$0.06$
$t\bar{t} + W/Z$	$9.06 \pm$	$0.05$
$t\bar{t}$	$4.90 \pm$	$0.64$
$Z + jets$	$6.28 \pm$	$1.47$
Dibosons	$12.30 \pm$	$0.25$
Total background	$37.36 \pm$	$1.62$
Observed	42	

Table 4.7.3:  $Z$ +jets trilepton control region event yields after the selection criteria. The uncertainties presented corresponds only to the statistical errors.

The  $t\bar{t}$  control region selection requires exactly three leptons,  $E_T^{\text{miss}}$  higher than 20 GeV,  $M_T(W)$  higher than 40 GeV, at least one OSSF pair of leptons with a reconstructed mass outside the range of 80 and 100 GeV and, finally, exactly two jets where one is an  $b$ -tagged jet. Figure 4.7.5 shows relevant distributions of the  $t\bar{t}$  control region.

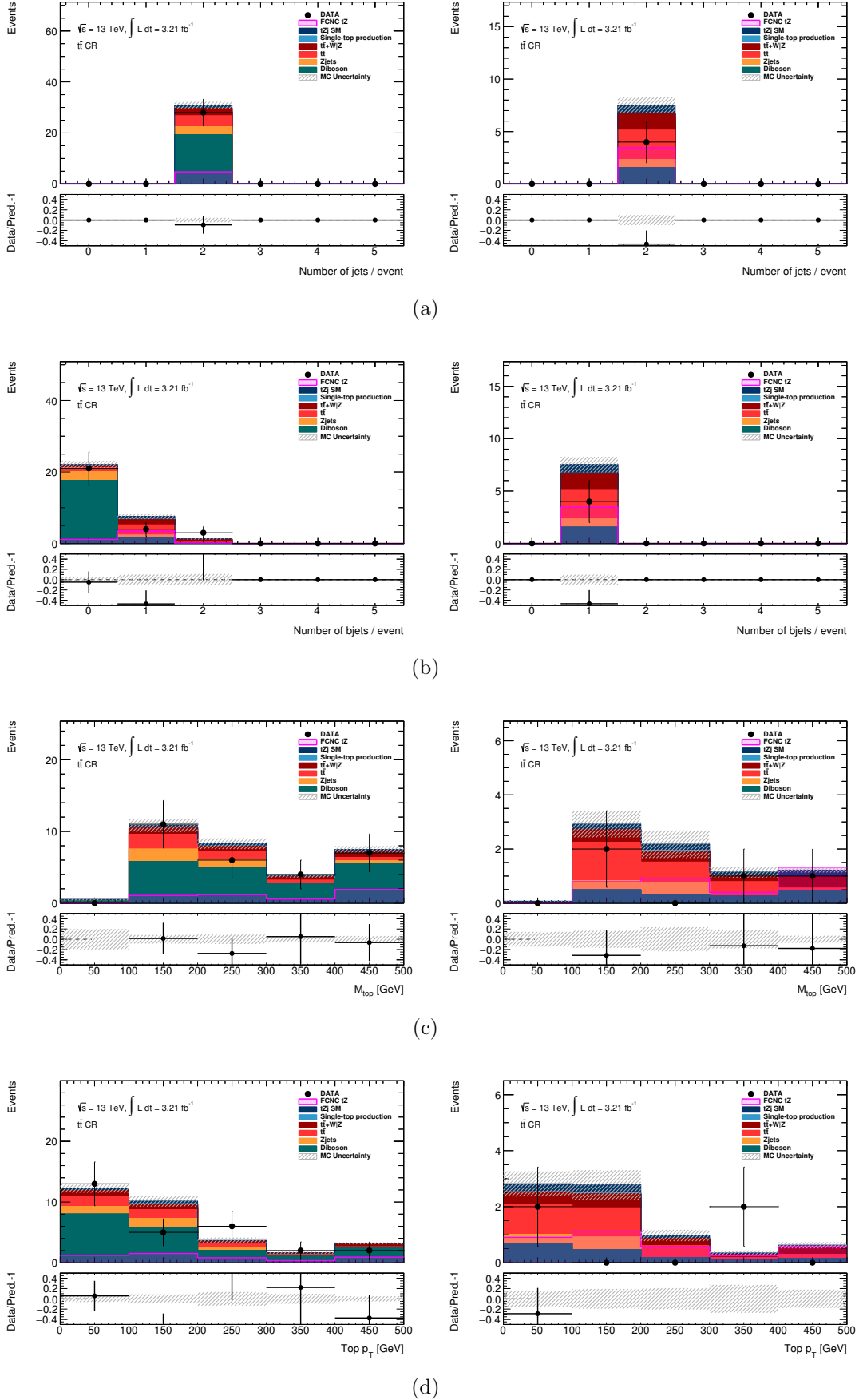


Figure 4.7.5:  $t\bar{t}$  control region distributions of (a) jet multiplicity, (b)  $b$ -tagged jet multiplicity, (c) top quark mass and (d) top quark  $p_T$  before (left) and after (right) the  $b$ -tagged jet requirement.

Figure 4.7.5(a) represents the jet multiplicity before and after the  $b$ -tagging requirement. The agreement between data and MC is reasonable for the distribution before requiring a  $b$ -tagged jet while is not good for the distribution after this requirement. The same behavior is also observed in the distributions in Figure 4.7.5(b). The  $b$ -tagged jet multiplicity in Figure 4.7.5(b) shows the exclusion power of the  $b$ -tagging requirement in the dibosons processes. After the selection criteria, a reasonable fraction of  $t\bar{t}$  events can be seen, even taking into account that this process is characterized by having two and not three leptons in the final state. Figure 4.7.5(c) represents the top quark reconstructed mass. The distribution shows a range of 100 and 500 GeV to this variable with a small peak in the measured top quark mass ( $\sim 173$  GeV). The  $p_T$  distribution of the reconstructed top quark shown in Figure 4.7.5(d) has a big range localized between 0 and 500 GeV. A good agreement between data and MC for the distributions in Figure 4.7.5 is disallowed by the low statistics in this region. Comparing the distributions for the levels before and after the  $b$ -tagging requirement, a better agreement can be seen in the distributions before this final criteria due to a higher statistics.

The events yields for the control region of  $t\bar{t}$  background after the selection are shown in Table 4.7.4. The event yields presented in Table 4.7.4 reveals that the selection made for this control region was appropriate. The  $t\bar{t}$  process is the dominant background process having  $\sim 3$  of the  $\sim 7$  background events. However, this region selection was defined taking in account the signal processes implying a lack of statistics after the selection criteria. Despite that, a reasonable agreement between data and MC was achieved considering the number of events after the selection criteria. Through the event yields, a contamination of signal can be seen due to the normalisation arbitrary chosen that was already excluded by the limits obtained in previous searches [56, 57, 53, 55, 58].

The dibosons control region is focused on the  $WZ$  process since it is the dibosons process closest to the signal final state. The selection consists in requiring exactly three leptons, at least one OSSF pair of leptons with a reconstructed mass between 81 and 101 GeV and exactly one jet.

Process	$t\bar{t}$ CR
FCNC $tZ$	$3.45 \pm 0.21$
SM $tZj$	$0.80 \pm 0.03$
Single Top	$0.05 \pm 0.03$
$t\bar{t} + W/Z$	$1.54 \pm 0.02$
$t\bar{t}$	$2.81 \pm 0.48$
$Z + \text{jets}$	$0.78 \pm 0.55$
Dibosons	$1.54 \pm 0.07$
Total background	$7.52 \pm 0.73$
Observed	4

Table 4.7.4:  $t\bar{t}$  control region event yields after the selection criteria. The uncertainties presented corresponds only to the statistical errors.

Figure 4.7.6 shows some relevant distributions for the  $WZ$  dibosons control region. Figure 4.7.6(a) represents the  $W$  boson mass where a peak in the measured  $W$  mass ( $\sim 80$  GeV) can be seen. Besides that, it is clear that the dibosons is the dominant background. Figure 4.7.6(b) shows the  $Z$  boson candidate mass with a good agreement between data and MC and a peak in the region between 80 and 100 GeV. The  $p_T$  distribution of the  $Z$  boson candidate in Figure 4.7.6(c) reveals the main difference between the dibosons background and the signal. While the dibosons events has a softer  $p_T$  distribution, the signal has a harder distribution. This characteristic can be used to separate background and signal in the next step of this analysis. A good agreement between data and prediction is also achieved in these distributions. The  $b$ -tagged jet multiplicity represented in Figure 4.7.6(d) shows again that the signal events are characterized by having a  $b$ -tagged jet in the final state and the majority of events are localized in the region without a  $b$ -tagged jet which is important to distinguish signal from background. Figure 4.7.6(e) represents the distribution for the transverse mass of the  $W$  boson showing that the signal and the dibosons background have similar distributions for this

observable. This characteristic can be predicted since one  $W$  boson is expected in both final states. A good agreement between data and MC is a characteristic of the distributions for this control region.

The same behavior is seen in Figure 4.7.6(f) where the  $E_T^{\text{miss}}$  distribution is shown. Both the signal and the dibosons background has a distribution composed by high values of  $E_T^{\text{miss}}$  which is consistent with at least one neutrino in the final state. Knowing that the  $W$  boson can decay to a charged lepton and a neutrino, this distribution is consistent with the prediction.

The events yields for the control region of dibosons background, specifically in the  $WZ$  process, after the selection are shown in Table 4.7.5.

The good isolation of the  $WZ$  dibosons processes in this control region can be seen in Table 4.7.5 where the dibosons background has  $\sim 125$  against the total of  $\sim 133$  background events. The agreement between data and MC is not so good and can be explain by the  $Z$ +jets normalisation. A fit can be helpful for a better agreement between data and MC. Since the dibosons is the dominant background of the signal region, the distributions for this control region allows the study of possible discriminant variables.

The  $tZj$  control region definition is important since this process has a topology similar to the signal region. The  $tZj$  process has a small cross-section expectation and no evidence was found until the moment [58]. The selection requires exactly three leptons,  $E_T^{\text{miss}}$  higher than 20 GeV, at least one OSSF pair of leptons having a mass between 70 and 110 GeV and at least one jet having exactly one  $b$ -tagged jet.

Figure 4.7.7 shows some relevant distributions for the  $tZj$  control region. The jet multiplicity represented in Figure 4.7.7(a) shows the effect that the  $b$ -tagging requirement has in this control region. Before requiring an  $b$ -tagged jet the main background corresponds to the dibosons processes. However, after the  $b$ -tagging requirement, the total background is composed by the different backgrounds considered but in small fractions. The data and MC agreement is reasonable for both the distributions in the regions between one and three jets where the majority of the number of events is observed.

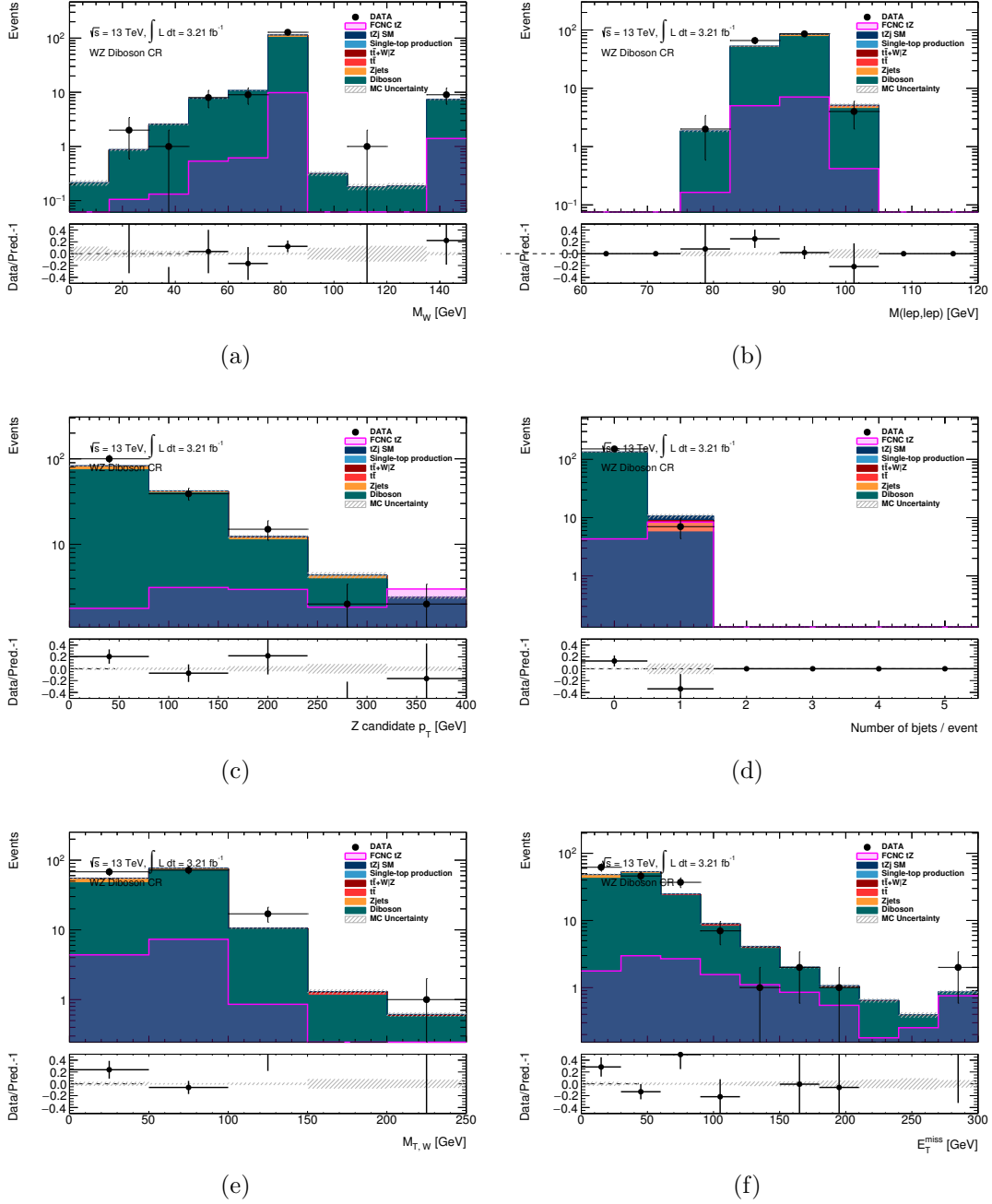


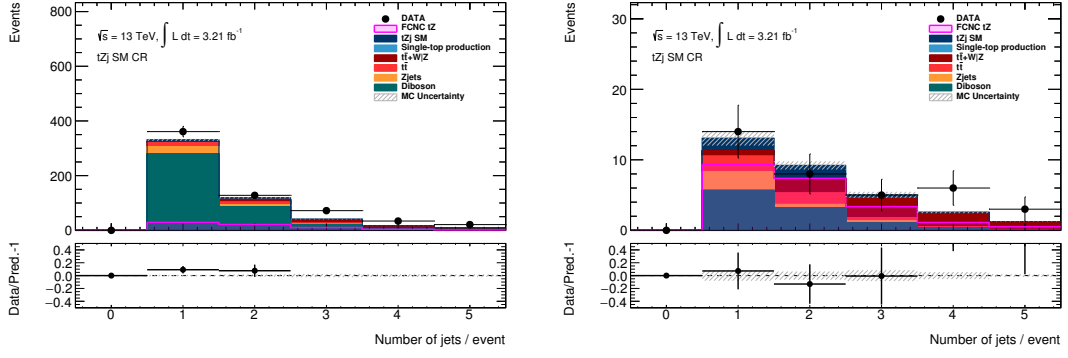
Figure 4.7.6:  $WZ$  Diboson control region distributions of (a)  $W$  boson mass, (b)  $Z$  boson candidate mass, (c)  $Z$  boson candidate  $p_T$ , (d)  $b$ -tagged jet multiplicity, (e)  $W$  boson transverse mass and (f)  $E_T^{\text{miss}}$  after the selection criteria.

Process	WZ Diboson CR	
FCNC $tZ$	$4.41 \pm$	0.25
SM $tZj$	$1.01 \pm$	0.03
Single Top	$0.03 \pm$	0.03
$t\bar{t} + W/Z$	$0.40 \pm$	0.01
$t\bar{t}$	$0.75 \pm$	0.25
$Z + \text{jets}$	$5.85 \pm$	1.64
Dibosons	$125.45 \pm$	0.63
Total background	$133.50 \pm$	1.77
Observed	151	

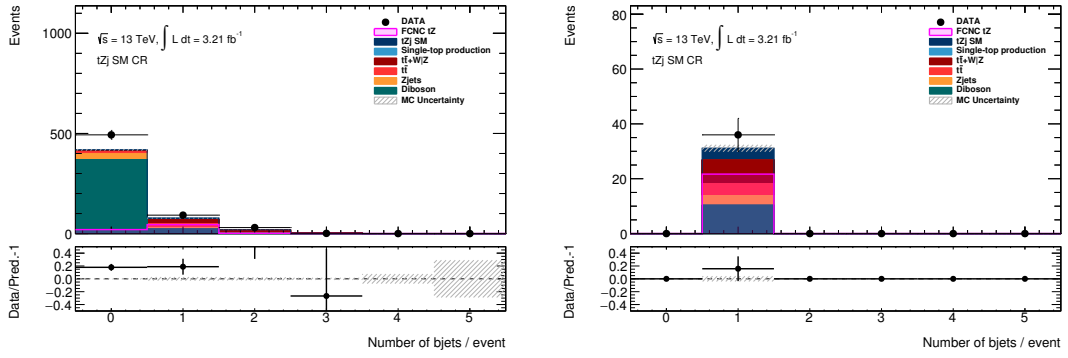
Table 4.7.5:  $WZ$  Diboson control region event yields after the selection criteria. The uncertainties presented corresponds only to the statistical errors.

Figure 4.7.7(b) represents the  $b$ -tagged jet multiplicity distributions. Before requiring a  $b$ -tagged jet, a reasonable agreement between data and MC is seen in the region without  $b$ -jets and with exactly one  $b$ -jet. After requiring one  $b$ -jet, a better agreement between data and MC was achieved where the  $tZj$  SM background starts to appear along with the other background processes. Figure 4.7.7(c) shows the  $Z$  boson candidate mass distribution with a reasonable data and MC agreement being better in the region between 80 and 100 GeV due to the large statistics. Comparing the two distributions, it is clear the effect that the  $b$ -tagging requirement has in the number of events of background decreasing a factor of  $\sim 10$ . The  $E_T^{\text{miss}}$  distributions in Figure 4.7.7(d) show a similar behavior between the signal and the main background which corresponds to the dibosons background. This behavior is characterized by high values of  $E_T^{\text{miss}}$  which is consistent with the signal and the dibosons background prediction. Since a  $W$  boson is a characteristic of these two processes, a neutrino is expected in the final state leading to high values of the variable  $E_T^{\text{miss}}$ .

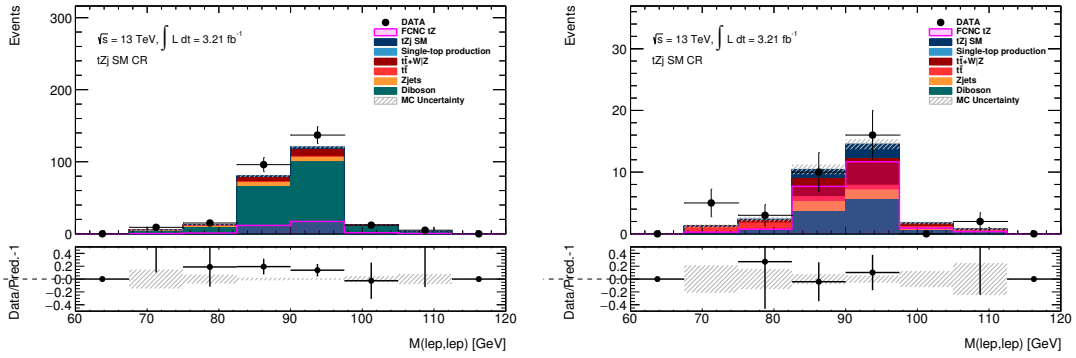




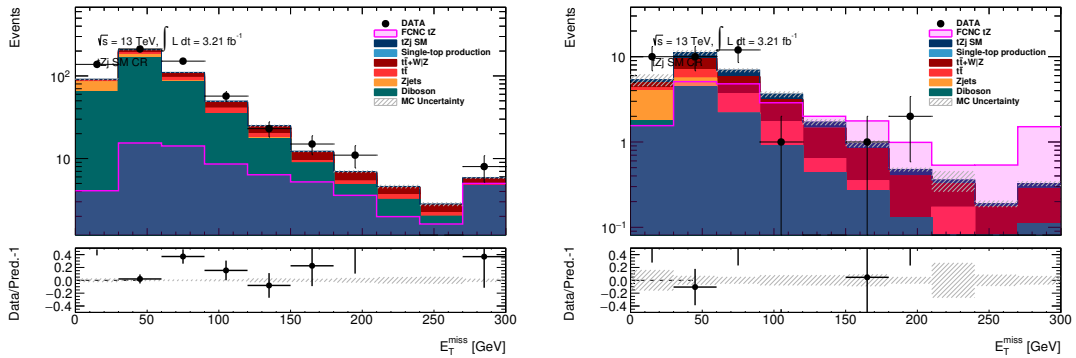
(a)



(b)



(c)



(d)

Figure 4.7.7:  $tZj$  control region distributions of (a) jet multiplicity, (b)  $b$ -tagged jet multiplicity, (c)  $Z$  boson candidate mass and (d)  $E_T^{\text{miss}}$  before (left) and after (right) the  $b$ -tagged jet requirement.

The events yields for the control region of  $tZj$  background after the selection are shown in Table 4.7.6.

Process	$tZj$ CR
FCNC $tZ$	$21.68 \pm 0.54$
SM $tZj$	$4.27 \pm 0.06$
Single Top	$0.08 \pm 0.05$
$t\bar{t} + W/Z$	$8.50 \pm 0.05$
$t\bar{t}$	$4.50 \pm 0.61$
$Z + \text{jets}$	$3.40 \pm 1.08$
Dibosons	$10.35 \pm 0.22$
Total background	$31.12 \pm 1.26$
Observed	36

Table 4.7.6:  $tZj$  control region event yields after the selection criteria. The uncertainties presented corresponds only to the statistical errors.

In the  $tZj$  control region, the dominant background is the dibosons taking in account the events yields. There are other backgrounds with a significant number of events after the selection criteria which explain the difficulty on the  $tZq$  SM production observation. Although, the  $tZj$  SM process has  $\sim 4$  of the total of  $\sim 31$  background events which indicates an appropriate control region definition. This control region is characterized by a good data and prediction agreement even with a low statistics after all the selection.

In this section, a comparison between data and prediction is made. However, a reasonable level of agreement between data and MC was not achieved for all the control regions. This disagreement appears to be essentially due to the normalisation of the  $Z+\text{jets}$  background which can be corrected in the fit discussed in Section 5.2.

## 4.8 Systematic uncertainties

The presented results are affected by different sources of systematic uncertainties associated with the respective measurement and that include the background and signal modeling as well as the instrumental uncertainties. The sources studied in this thesis include the measurement of the luminosity, lepton efficiency scale factor, lepton energy scale and resolution, jet energy scale and resolution, the  $b$ -tagging efficiency and  $E_T^{\text{miss}}$  calculation. These uncertainties are propagated to the analysis by varying the corresponding parameters in the event reconstruction and repeating the full analysis. The resulting event yields can then be compared to the central values obtained with the nominal event reconstruction in order to get an estimate of the effect of the systematic uncertainty.

Uncertainties like the  $b$ -tagging efficiency and the jet energy scale are split into several components representing independent uncertainties. The dominant sources of uncertainty are due to the jet energy scale and resolution. The jet energy scale uncertainty is divided in orthogonal components which represent independent effective uncertainties using different techniques. The jet energy resolution uncertainty is obtained through comparisons of simulation and data using studies with Run-1 data. These studies are then checked to have an agreement with Run-2 data [97].

The  $E_T^{\text{miss}}$  calculation consists in contributions from soft terms coming from low- $p_T$  pileup jets and underlying event activity and from hard terms coming from leptons and jets. The uncertainty related with the soft terms is obtained by comparing the simulated scale and resolution to that in data. The uncertainty associated with the hard terms is propagated from the corresponding jet and lepton scale and resolution uncertainties being classified together with the uncertainty on the hard objects.

The  $b$ -tagging uncertainties are determined with the  $\sqrt{s}=8$  TeV data, then extrapolated and checked using the  $\sqrt{s}=13$  TeV data. These uncertainties use independent eigenvectors for the efficiency of  $b$  jets,  $c$  jets, light-parton jets and two extrapolation uncertainty factors.

## 4.9 Discriminant variables

The separation of background and signal can be found through a study of possible discriminant variables. In Section 4.6.1, the signal region selection was presented and the conclusion is that the  $p_T$  distribution of the  $Z$  boson candidate corresponds to the best variable to distinguish signal from background. Since the dominant backgrounds of this analysis corresponds to the dibosons and  $Z$ +jets processes, the final state of these processes can be used to study the relation between the distributions of  $p_T$  of the  $Z$  boson candidate with the reconstructed top quark mass and with the transverse mass of the reconstructed  $W$  boson. The  $Z$ +jets background was a final state with a reconstructed  $Z$  boson and jets. This process does not contain a top quark or a  $W$  boson which means that the reconstructed top quark mass should not peak in the top quark mass and the transverse mass of the reconstructed  $W$  boson should have values below 50 GeV. The dominant process of the dibosons background is the  $WZ$  process. This means that the transverse mass of the  $W$  boson should be higher than 50 GeV with the same behavior of the signal process. Since a top quark is not expected in the final state, it is expected that the reconstructed top quark mass do not have a distribution compatible with the mass distribution of a top quark. In Figures 4.9.1 and 4.9.2, a comparison for backgrounds and signal of two dimensional distributions of the  $p_T$  of the  $Z$  boson candidate with the reconstructed top quark mass and the transverse mass of the  $W$  boson after the signal region selection was presented.

Figure 4.9.1(a) shows the distributions for the single top background where the production of one top quark is expected. Since in this analysis only the  $Wt$  channel are studied for the single top production, the final state consists in a top quark and a  $W$  boson. The distributions shown in Figure 4.9.1(a) reveals a good description of the background process studied.

Concerning the  $t\bar{t}$  background distributions, represented in Figure 4.9.1(b), the transverse mass of the  $W$  boson was distributed in all the range (between 0 and 250 GeV). This behavior only can be seen in these background process.

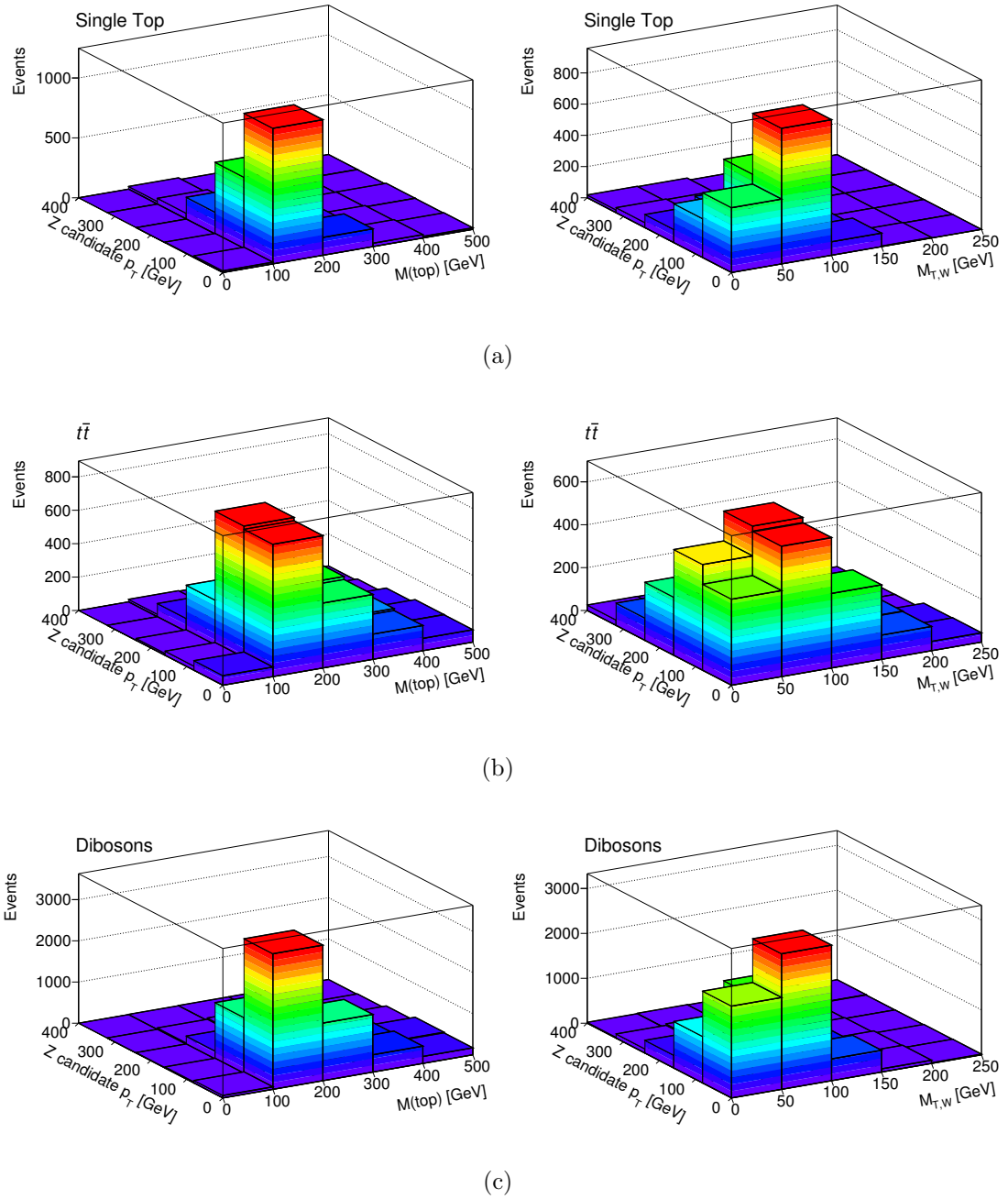


Figure 4.9.1: Two dimensional distributions for (a) single top production, (b)  $t\bar{t}$  and (c) dibosons, shown as a function of the  $Z$  boson candidate  $p_T$  and the reconstructed top quark mass (left) and the transverse mass of the  $W$  boson (right).

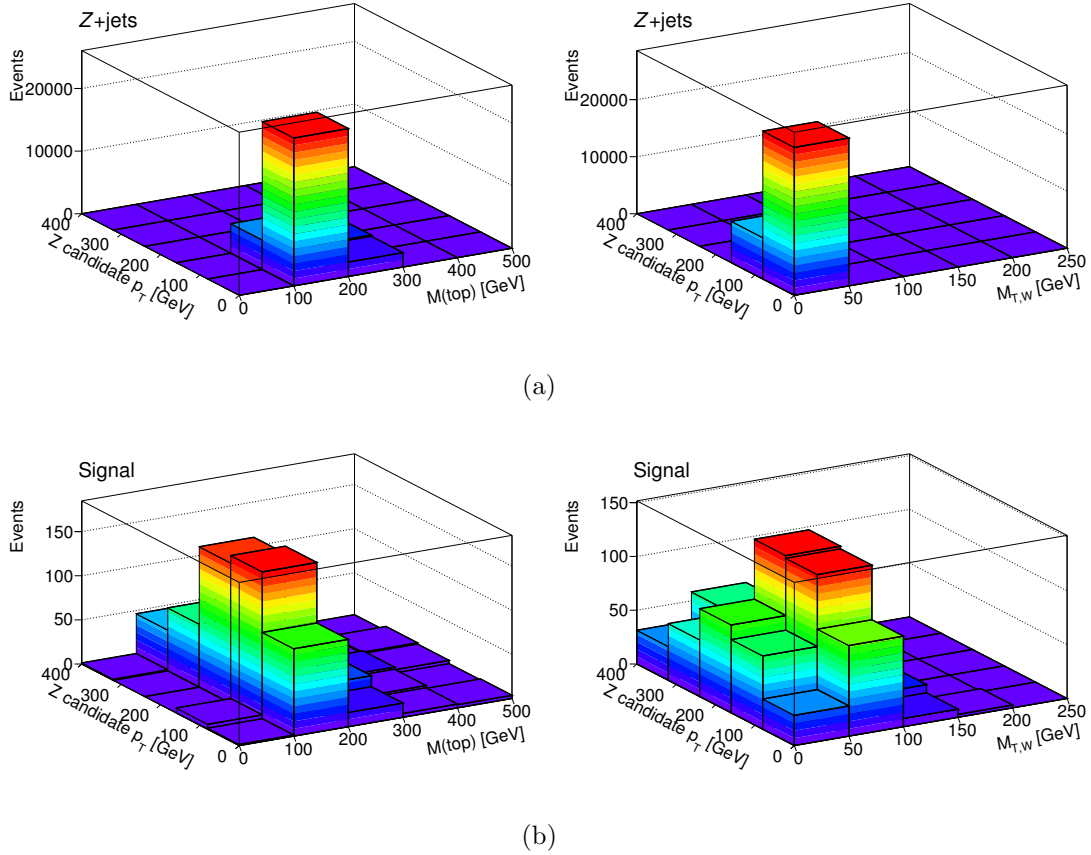


Figure 4.9.2: Two dimensional distributions for (a)  $Z + \text{Jets}$  and (b) signal, shown as function of the  $Z$  boson candidate  $p_T$  and the reconstructed top quark mass (left) and the transverse mass of the  $W$  boson (right).

In Figure 4.9.1(c) are represented the dibosons background distributions with the a higher number of events in the region with a transverse mass of  $W$  boson between 50 and 100 GeV.

In Figure 4.9.2(a) for the  $Z+\text{jets}$ , the two dimensional distributions shows that all the events have a transverse mass of the  $W$  boson lower than 50 GeV, implying that this a good variable to cut on the signal region selection.

The distributions for signal, in Figure 4.9.2(b), show the majority of events in the region with the  $M_T(W)$  higher than 50 GeV which are in agreement with the presence of a  $W$  boson in the final state.

For all the background and signal distributions, the number of events is significantly higher in the region of the reconstructed top quark mass between 100 and 200 GeV (which are in agreement with the measured top quark mass of 173 GeV). These two dimensional distributions comparing the  $Z$  boson candidate  $p_T$  with the reconstructed top quark mass shows that maybe the top quark mass is not a good discriminant variable.

In order to study the effect of this two variables, new signal regions are defined where one cut is added to the signal region selection. The goal is to have two sets of complementary regions. The first set is characterized for having a cut on the transverse mass of the  $W$  boson with one region requiring a value below 50 GeV and the complementary region above 50 GeV. The second set has a cut on the reconstructed top quark mass where the reconstructed top quark mass should be inside or outside a range of 153 and 193 GeV (difference of 20 GeV to the measured top quark mass which is 173 GeV [5]).

SR $M_T(W) < 50$ GeV	SR $M_T(W) > 50$ GeV	SR On top peak	SR Off top peak
		= 3 leptons	
		$\geq 1$ OSSF Pair	
		$70 \text{ GeV} < M(\ell\ell) < 110 \text{ GeV}$	
		= 1 $b$ -tagged jet	
$M_T(W) < 50 \text{ GeV}$	$M_T(W) > 50 \text{ GeV}$	$ M_{reco}(t) - M(t)  < 20 \text{ GeV}$	$ M_{reco}(t) - M(t)  > 20 \text{ GeV}$

Table 4.9.1: Definition of distinct signal region selections in order to separate background for signal. A cut on the transverse mass of  $W$  boson or in the reconstructed top quark mass are added to the signal region selection.

The distributions of the two regions with the added cut on the transverse mass of  $W$  boson are shown in Figure 4.9.3. With this cut, the expectation is to separate the  $Z$ +jets background from all the other backgrounds and signal.

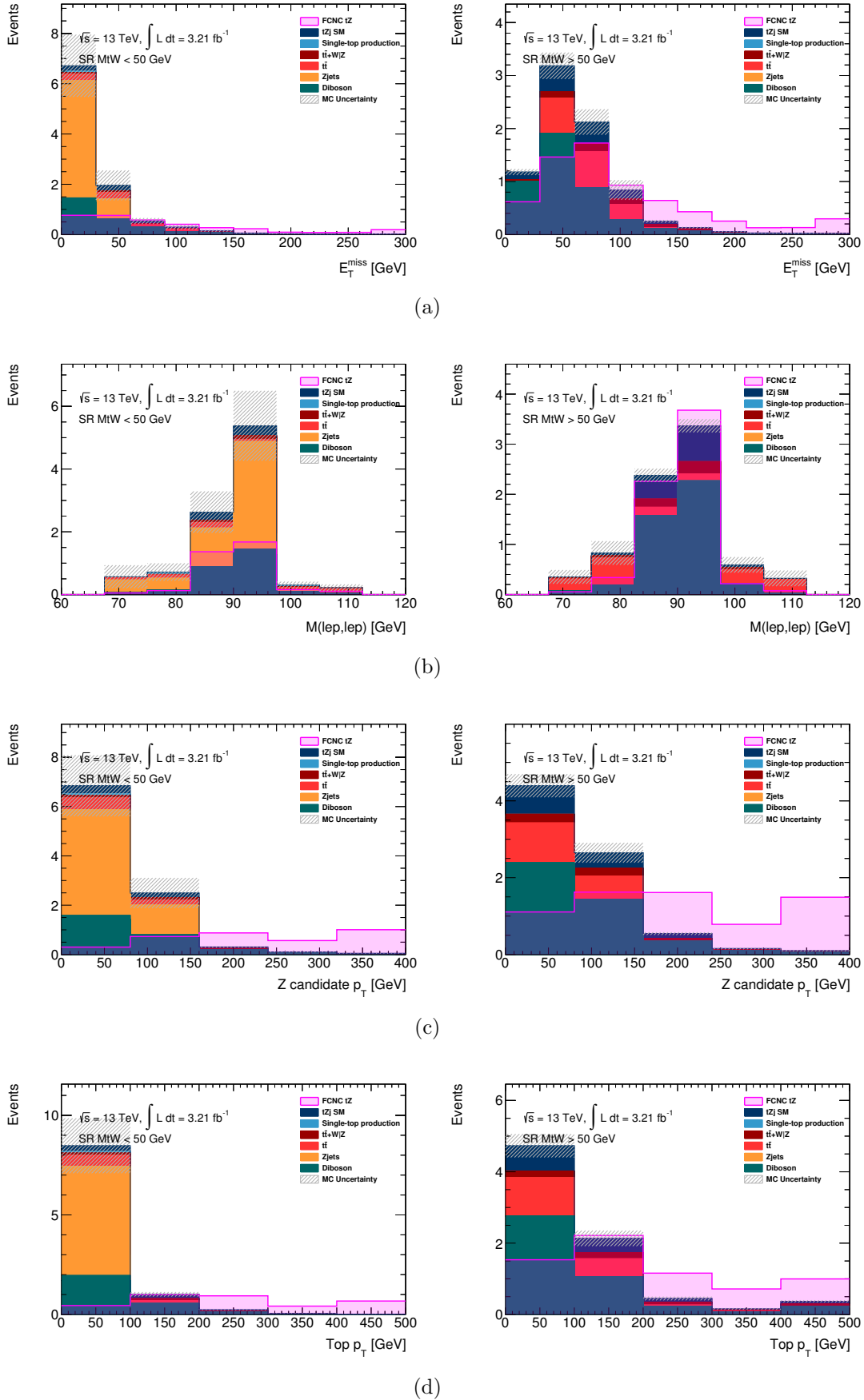


Figure 4.9.3: Distributions of (a)  $E_T^{\text{miss}}$ , (b) the  $Z$  boson candidate mass, (c) the  $Z$  boson candidate  $p_T$  and (d) the reconstructed top quark  $p_T$  for the signal region with the added cut on the transverse mass of the  $W$  boson.



The plots in Figure 4.9.3 reflect the excellent isolation of the  $Z$ +jets background in the region with the transverse mass of the  $W$  boson below 50 GeV which is the second dominant background of the signal region. More specifically the  $E_T^{\text{miss}}$  distribution in Figure 4.9.3(a) shows the clear signature of signal when the cut of  $M_T(W) > 50$  GeV is applied. Beside that, the  $Z$ +jets background has the lowest values of this variable in agreement with the final state of this process.

In Figure 4.9.3(b) the  $Z$  boson candidate mass is characterized by a good distribution in the two regions with a peak centered in the  $Z$  boson measured mass. This behavior does not allow the possibility of considering the  $Z$  mass as a discriminant variable. The  $p_T$  of the  $Z$  boson candidate and the reconstructed top quark mass can be considered as discriminant variables due to the differences between signal and background distributions shown in Figures 4.9.3(c) and 4.9.3(d).

The event yields for these two complementary regions, in Table 4.9.2, reveals once again the excellent isolation of the  $Z$ +jets with all the events from this background in the region with the  $M_T(W)$  lower than 50 GeV. The single top background corresponding to the  $Wt$  channel are also isolated in the region with the lower  $M_T(W)$ . However, the dibosons processes still have the higher fraction of the background event yields.

The distributions of the two regions with the added cut on the reconstructed top quark mass are shown in Figure 4.9.4. With this cut, the expectation is also separate the  $Z$ +jets background from all the other backgrounds and signal since this process do not have a top quark in the final state.

Process	SR	
	$M_T(W) < 50$	$M_T(W) > 50$
FCNC $tZ$	$3.47 \pm 0.22$	$6.62 \pm 0.30$
SM $tZj$	$0.62 \pm 0.02$	$1.32 \pm 0.03$
Single Top	$0.08 \pm 0.05$	$0.00 \pm 0.00$
$t\bar{t} + W/Z$	$0.23 \pm 0.01$	$0.53 \pm 0.01$
$t\bar{t}$	$0.71 \pm 0.24$	$1.64 \pm 0.38$
$Z + \text{jets}$	$5.47 \pm 1.35$	$0.00 \pm 0.00$
Dibosons	$2.66 \pm 0.17$	$4.34 \pm 0.12$
Total background	$9.80 \pm 1.38$	$7.84 \pm 0.40$

Table 4.9.2: Event yields for the signal region selection with a cut on the transverse mass of the reconstructed  $W$  boson. The uncertainties presented corresponds only to the statistical errors.

The  $E_T^{\text{miss}}$  distribution, in Figure 4.9.4(a), shows a higher percentage of  $t\bar{t}$ , dibosons and other backgrounds in the region inside the top quark mass and a higher percentage of  $Z+\text{jets}$  in the region outside the top quark mass. The signal simulation has higher values of  $E_T^{\text{miss}}$  in the region inside the top quark mass in agreement with the prediction since a neutrino are expected in the final state.

In Figure 4.9.4(b) are shown the  $Z$  boson candidate mass distribution in agreement with the prediction and well defined around the measured value of the  $Z$  boson.

The  $Z$  boson candidate  $p_T$  represented in Figure 4.9.4(c) reveals a promising distribution which is different for background and signal. The same behavior can be seen in Figure 4.9.4(d) where the reconstructed top quark mass are shown. For these distributions, the background processes have a softer distribution while the signal has a harder  $p_T$  values. In agreement with Figure 4.9.3(c), the  $Z$  boson candidate  $p_T$  probes again being a good discriminant variable.

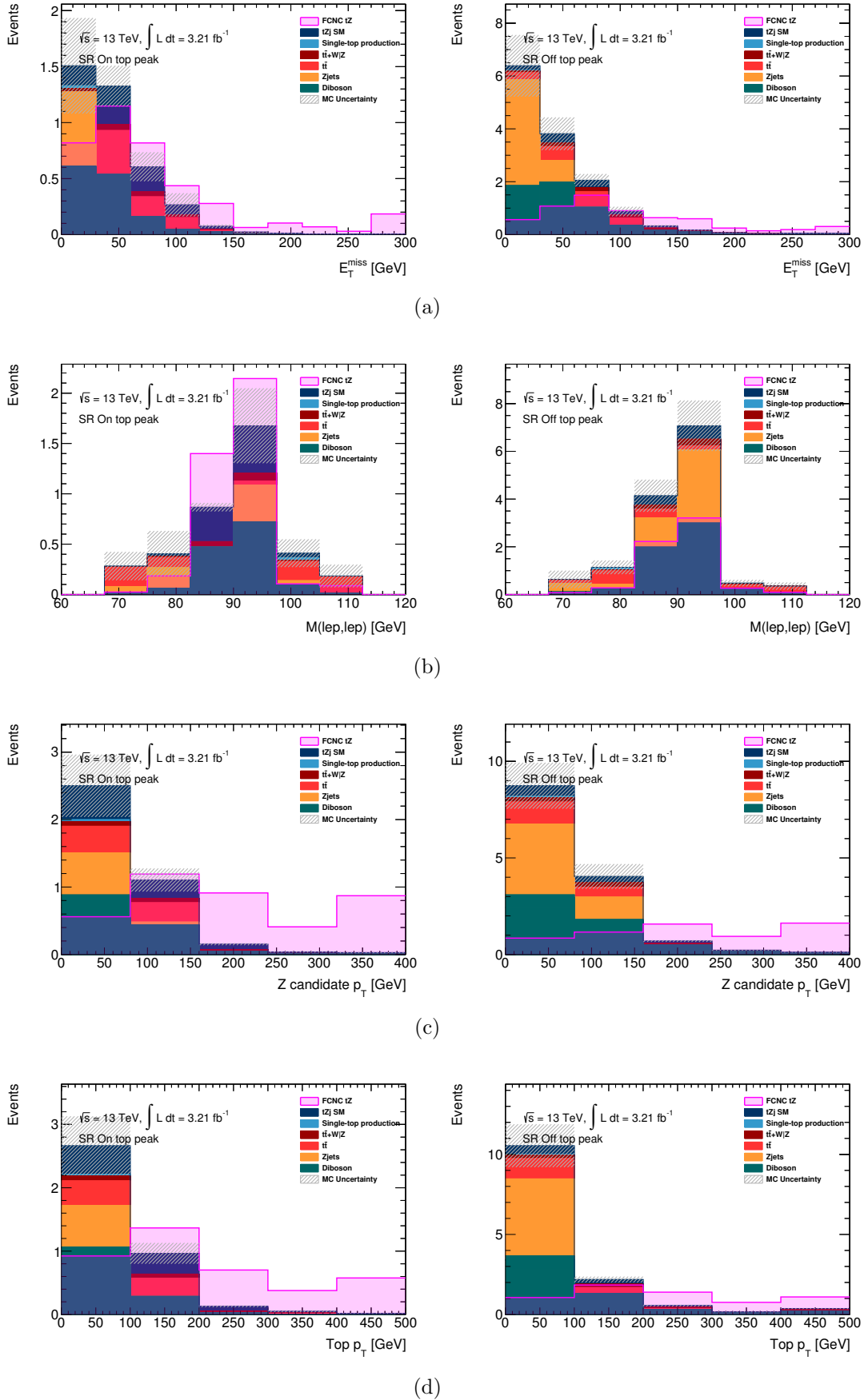


Figure 4.9.4: Distributions of (a)  $E_T^{\text{miss}}$ , (b) the  $Z$  boson candidate mass, (c) the  $Z$  boson candidate  $p_T$  and (d) the reconstructed top quark  $p_T$  for the signal region with the added cut on the reconstructed top quark mass.

Process	SR		SR	
	On top peak		Off top peak	
FCNC $tZ$	$3.95 \pm$	$0.23$	$6.15 \pm$	$0.29$
SM $tZj$	$0.89 \pm$	$0.03$	$1.05 \pm$	$0.03$
Single Top	$0.03 \pm$	$0.03$	$0.06 \pm$	$0.04$
$t\bar{t} + W/Z$	$0.17 \pm$	$0.01$	$0.60 \pm$	$0.01$
$t\bar{t}$	$0.69 \pm$	$0.24$	$1.67 \pm$	$0.38$
$Z + \text{jets}$	$0.66 \pm$	$0.42$	$4.81 \pm$	$1.28$
Dibosons	$1.38 \pm$	$0.06$	$5.62 \pm$	$0.20$
Total background	$3.82 \pm$	$0.49$	$13.81 \pm$	$1.35$

Table 4.9.3: Event yields for the signal region selection with a cut on the reconstructed top quark mass. The uncertainties presented corresponds only to the statistical errors.

The events yields for the two regions with the cut on the reconstructed top quark mass, in Table 4.9.3, reveals that the majority of events passed the selection with the reconstructed quark mass outside the top peak. However, a reasonable isolation of the  $Z+\text{jets}$  background are obtained with  $\sim 90\%$  of the events selected by the region with the top quark mass outside the mass peak.

# Chapter 5

## Limits

Through the  $CL_s$  prescription at the 95% CL, expected upper limits on the  $tZ$  production via FCNC cross-section was obtained. With these limits on the cross-section, expected limits on the branching ratios can be defined. In this chapter a briefly description of the  $CL_s$  method [98, 99] and the limits on the anomalous coupling and the branching ratio are presented.

### 5.1 The $CL_s$ method

In particle physics one of the most important goals of a search is to exclude as much as possible the existence of a signal in its absence or to confirm the existence of a true signal as much as possible. The discovery or exclusion of a new physics model is performed through a statistical test. In order to achieve this, two hypothesis are considered and tested where one describes the known physics processes and the other includes the new phenomena. These two scenarios are described as follows:

- Corresponding to the SM known processes, it is often referred to as the background-only ( $b$ ) hypothesis;
- Corresponding to the SM known processes with the addition of a new signal process, it is often referred to as the signal-plus-background ( $s+b$ ) hypothesis.

In the search presented in this thesis, the SM without FCNC interactions is considered the background-only scenario, while the signal-plus-background scenario includes the FCNC interactions as signal.

A test statistical  $Q$  is used to quantify the compatibility of the observed data with the given hypothesis being optimal when it is the likelihood ratio of Poisson probabilities as follows

$$Q = \frac{P(\text{data}|\text{signal} + \text{background})}{P(\text{data}|\text{background})} \quad (5.1.1)$$

where the probabilities are defined as

$$P(\text{data}|\text{background}) = \frac{b^n e^{-b}}{n!} \quad (5.1.2)$$

$$P(\text{data}|\text{signal} + \text{background}) = \frac{(s + b)^n e^{-(s+b)}}{n!} \quad (5.1.3)$$

being  $s$  and  $b$  the signal and background expected events after an analysis and  $n$  the observed number of events.

The consistency of the data with the background-only and the signal-plus-background hypothesis is obtained through a association between the test statistic  $Q$  and the probability distribution  $P$ . These consistencies are obtained by defining different confidence levels.

The confidence level for excluding the possibility of simultaneous presence of new interactions or new particles production and background ( $s+b$  hypothesis) is given by  $CL_{s+b}$  and can be defined as the probability that the test statistic would be less than or equal to that observed in the data, assuming the presence of both signal and background. The confidence level for the background alone is given by  $CL_b$  and can be defined as the probability that background processes would give fewer than or equal to the number of candidates observed. These two confidence levels are defined as follows

$$CL_{s+b} = P(Q \leq Q_{obs}|\text{signal} + \text{background}) \quad (5.1.4)$$

$$CL_b = P(Q \leq Q_{obs}|\text{background}) \quad (5.1.5)$$

With the  $CL_{s+b}$  and  $CL_b$  defined, the equation of the confidence level for the

signal-only hypothesis,  $CL_s$ , can be obtained and defined as

$$CL_s = \frac{CL_{s+b}}{CL_b}. \quad (5.1.6)$$

In case  $CL_s < 0.05$ , the signal-plus-background hypothesis with a signal strength  $\mu$  is excluded at 95% CL. Taking in account that the number of expected signal events  $s$  depends on the expected cross-section or other model parameters, the upper or lower limits for the different values can be computed. Specifically in the cross-section, upper limits on the expected cross-section can be obtained by solving the equation

$$CL_s(\sigma) = \alpha \quad (5.1.7)$$

with the fixed value of  $\alpha$  is defined on the chosen confidence level  $(1 - \alpha)$ .

## 5.2 Limits on the $tZ$ production

The study of possible discriminant variables in Section 4.8 enabled the definition of the transverse mass of the  $W$  boson as the discriminant variable used for this analysis. Through a fit in the two complementary signal regions with a cut on the  $M_T(W)$  (selection defined in Table 4.9.1), expected upper limits are obtained for a luminosity of  $3.21 \text{ fb}^{-1}$  and  $30 \text{ fb}^{-1}$ .

The calculation of the limits for  $tZ$  production via FCNC presented here have been made in collaboration with the Humboldt University of Berlin. To obtain the limits presented here, different fits have been performed. First, a fit background-only model to real data was made. After this, using the nuisance parameters from the fit, a Asimov dataset without signal was generated. The expected upper limits was determined and a new Asimov dataset with signal set to the upper limit was generated. Finally, a fit of signal and background model to the last dataset was performed.

The input uncertainties on the normalisation are:

- Luminosity - 5.0%;
- $Z$ +jets and dibosons - 24.5%;

- $Wt$  channel - 5.4%;
- $t\bar{t}$  - 5.2%;
- $t\bar{t}V$  and  $tZj$  - 30.0%.

The pull plot was obtained with the correlation of a respective systematic and the signal added, shown in Figure 5.2.1. This correlation indicates how much of the total uncertainty is due to that particular systematic. The total correlation for the MC statistical error is 9.5%. In Figure 5.2.1 the pull plot shows that all the systematics considered are in agreement with the prediction since the central value agrees with the  $\theta=0$  and the error band do not pass significantly beyond  $|\theta| = 1$ . The higher pulls are the dibosons normalisation and the luminosity that affect directly the number of background events in the signal region.

For a luminosity of  $3.21 \text{ fb}^{-1}$ , the expected upper limits to the inclusive cross-section was 2.00 pb. For a luminosity of  $3.21 \text{ fb}^{-1}$ , the expected upper limits to the inclusive cross-section was 0.533 pb. In order to obtain a limit on the anomalous coupling  $K_{ut}^L$ , the cross-section as a function of the  $K_{ut}^L/\Lambda$  ( $\Lambda$  corresponds to the new physics scale) coupling was drawn for the two expected upper limits and for the theoretical prediction. For this study, it was considered that the inclusive cross-section does not depends of the anomalous coupling value. The intersection between the theoretical curve and the limits value corresponds to the limit on the anomalous coupling  $K_{ut}^L/\Lambda$ . The inclusive cross-section as a function of the anomalous coupling  $K_{ut}^L/\Lambda$  are shown in Figure 5.2.2.

The limit on the  $K_{ut}^L$  anomalous coupling for a luminosity of  $3.21 \text{ fb}^{-1}$  has the value of  $K_{ut}^L/\Lambda=0.045 \text{ TeV}^{-1}$ . In order to compare with the branching ratio from the section 2.3, the conversion of the anomalous coupling to the branching ratio was made using MADGRAPH5\_AMC@NLO. With the value of  $K_{ut}^L/\Lambda=0.045 \text{ TeV}^{-1}$ , the limit on the branching ratio for a luminosity of  $3.21 \text{ fb}^{-1}$  are  $\mathcal{BR}(t \rightarrow Zq) < 0.135\%$ . For a luminosity of  $30 \text{ fb}^{-1}$ , the limit has the value of  $K_{ut}^L/\Lambda=0.023 \text{ TeV}^{-1}$ . The limit on the branching ratio for a luminosity of  $30 \text{ fb}^{-1}$  are  $\mathcal{BR}(t \rightarrow Zq) < 0.036\%$ .



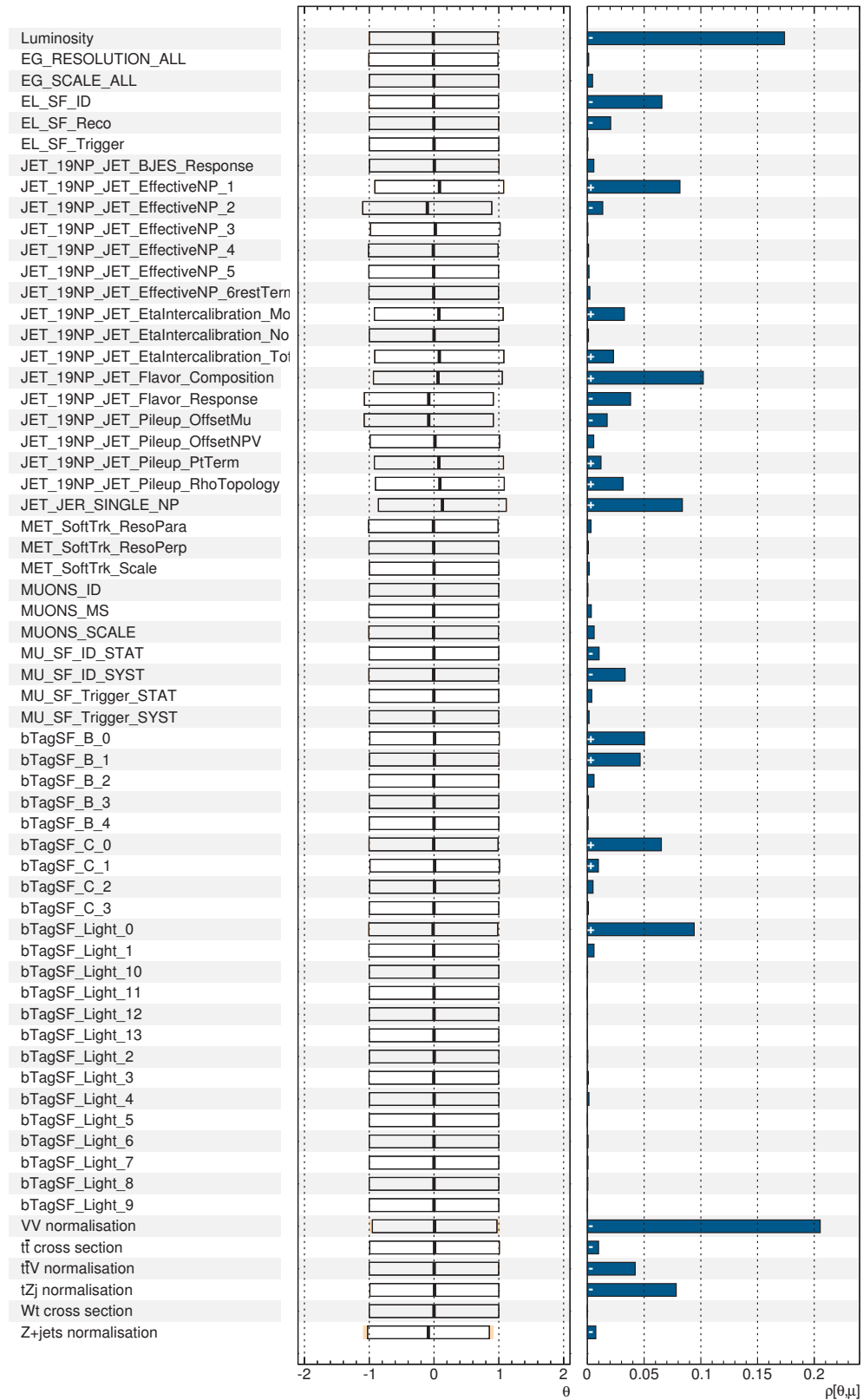


Figure 5.2.1: The pull plot for the systematics studied in this analysis and their correlation with the signal.

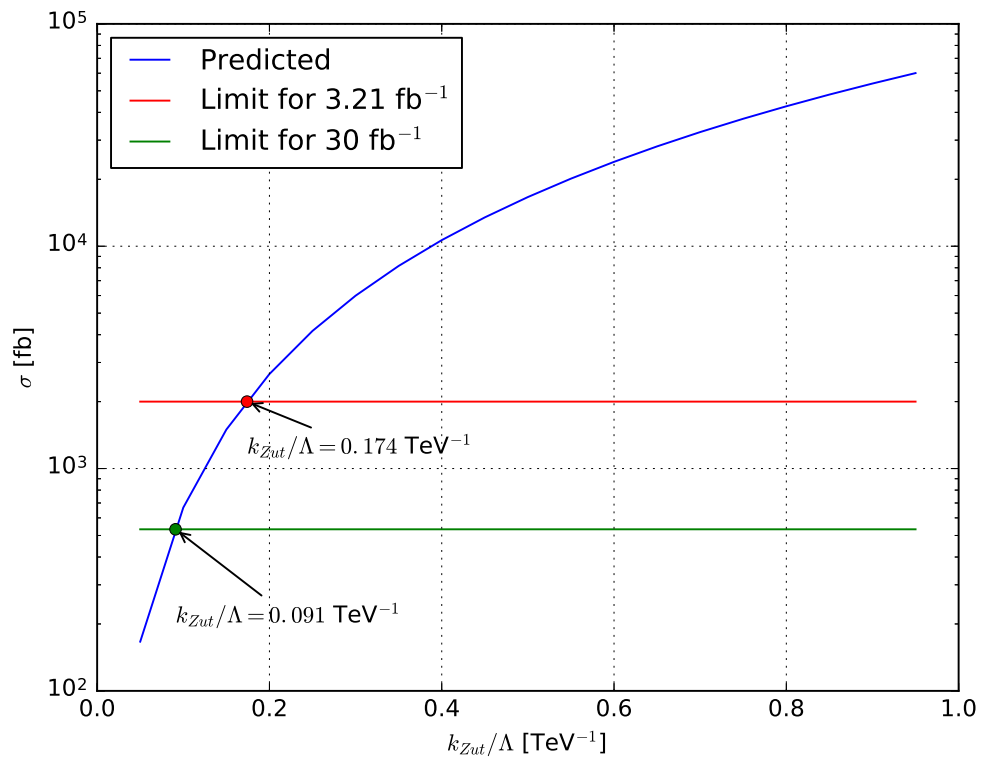


Figure 5.2.2: Expected upper limits at 95% CL for the anomalous coupling  $K_{Lut}/\Lambda$  considering the expected upper limits of the cross-sections for a luminosity of 3.21 fb $^{-1}$  and 30 fb $^{-1}$  and the theoretical prediction.

# Chapter 6

## Conclusions

In the present thesis, a search for  $tZ$  production through FCNC using LHC data collected by the ATLAS detector is presented. The data sample corresponds to an integrated luminosity of  $3.21 \text{ fb}^{-1}$  recorded in 2015 by the ATLAS experiment in proton-proton collisions at  $\sqrt{s} = 13 \text{ TeV}$ . As a first step to the unblinding of the data events in the signal region, the expected limits on the cross-section of the  $tZ$  production were obtained in the absence of signal. The unblinding of the data events in the signal region will be done as soon as the 2016 data be incorporated and after the collaboration approval.

A dedicated data analysis, composed by different control regions for the main backgrounds and a signal region focusing in the production of a top quark and a  $Z$  boson via FCNC was developed. A signal region selection was implemented considering the number of events remaining after all the selection cuts. However, a study of discriminant variables was presented to better distinguish between signal and background. The transverse mass of the  $W$  boson was the variable chosen to be the discriminant variable for the signal region and a fit was performed taking in account this added cut. The several sources of systematic uncertainties were also evaluated in this analysis.

With the collaboration of the Humboldt University (Berlin) group, the expected upper limits at 95% CL are set on the branching ratio for the decay of a top quark into a  $Z$  boson and a  $u$ -quark. The LHC continues to deliver 13 TeV collision data,

as shown in Figure 6.0.1, the new data will allow a increase in the sensitivity of this process that may enable the discovery or, alternatively, constrain in a significantly way the cross-section of the  $tZ$  production via FCNC.

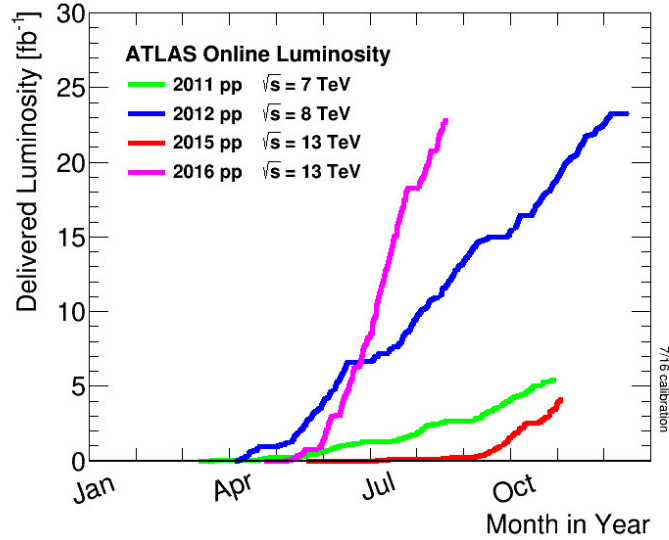


Figure 6.0.1: Luminosity per year for the different centre-of-mass energy at the LHC [100].

The posterior studies will consist in the conclusion of the study of systematic uncertainties as well as the possibility of increasing the sensitivity of the analysis considering multivariate techniques.

# Bibliography

- [1] S. L. Glashow, “Partial Symmetries of Weak Interactions,” *Nucl. Phys.*, vol. 22, pp. 579–588, 1961.
- [2] F. Abe *et al.*, “Observation of top quark production in  $\bar{p}p$  collisions,” *Phys. Rev. Lett.*, vol. 74, pp. 2626–2631, 1995.
- [3] S. Abachi *et al.*, “Observation of the top quark,” *Phys. Rev. Lett.*, vol. 74, pp. 2632–2637, 1995.
- [4] S. L. Glashow, J. Iliopoulos, and L. Maiani, “Weak Interactions with Lepton-Hadron Symmetry,” *Phys. Rev.*, vol. D2, pp. 1285–1292, 1970.
- [5] K. A. Olive *et al.*, “Review of Particle Physics,” *Chin. Phys.*, vol. C38, p. 090001, 2014.
- [6] H. Fritzsch, M. Gell-Mann, and H. Leutwyler, “Advantages of the color octet gluon picture,” *Physics Letters B*, vol. 47, no. 4, pp. 365 – 368, 1973.
- [7] Politzer, H. David, “Reliable Perturbative Results for Strong Interactions?,” *Phys. Rev. Lett.*, vol. 30, pp. 1346–1349, Jun 1973.
- [8] D. J. Gross and F. Wilczek, “Ultraviolet behavior of non-abelian gauge theories,” *Phys. Rev. Lett.*, vol. 30, pp. 1343–1346, Jun 1973.
- [9] S. L. Glashow, “Partial-symmetries of weak interactions,” *Nuclear Physics*, vol. 22, no. 4, pp. 579 – 588, 1961.

- 
- [10] A. Salam, “Weak and Electromagnetic Interactions,” *Conf. Proc.*, vol. C680519, pp. 367–377, 1968.
- [11] Weinberg, Steven, “A Model of Leptons,” *Phys. Rev. Lett.*, vol. 19, pp. 1264–1266, Nov 1967.
- [12] F. Englert and R. Brout, “Broken Symmetry and the Mass of Gauge Vector Mesons,” *Phys. Rev. Lett.*, vol. 13, pp. 321–323, 1964.
- [13] P. W. Higgs, “Broken Symmetries and the Masses of Gauge Bosons,” *Phys. Rev. Lett.*, vol. 13, pp. 508–509, 1964.
- [14] Guralnik, G. S. and Hagen, C. R. and Kibble, T. W. B., “Global Conservation Laws and Massless Particles,” *Phys. Rev. Lett.*, vol. 13, pp. 585–587, Nov 1964.
- [15] M. Bustamante, L. Cieri, and J. Ellis, “Beyond the Standard Model for Montaneros,” in *High-energy physics. Proceedings, 5th CERN-Latin-American School, Recinto Quirama, Colombia, March 15-28, 2009*, 2009.
- [16] Y. Fukuda *et al.*, “Evidence for oscillation of atmospheric neutrinos,” *Phys. Rev. Lett.*, vol. 81, pp. 1562–1567, 1998.
- [17] M. Altmann *et al.*, “Complete results for five years of GNO solar neutrino observations,” *Phys. Lett.*, vol. B616, pp. 174–190, 2005.
- [18] K. Abe *et al.*, “Evidence for the Appearance of Atmospheric Tau Neutrinos in Super-Kamiokande,” *Phys. Rev. Lett.*, vol. 110, no. 18, p. 181802, 2013.
- [19] K. Eguchi *et al.*, “First results from KamLAND: Evidence for reactor anti-neutrino disappearance,” *Phys. Rev. Lett.*, vol. 90, p. 021802, 2003.
- [20] Bruce T. Cleveland and Timothy Daily and Raymond Davis, Jr. and James R. Distel and Kenneth Lande and C. K. Lee and Paul S. Wildenhain and Jack Ullman, “Measurement of the Solar Electron Neutrino Flux with the Homestake Chlorine Detector,” *The Astrophysical Journal*, vol. 496, no. 1, p. 505, 1998.

- [21] K. Kröniger, A. B. Meyer, and P. Uwer, “Top-Quark Physics at the LHC,” in *The Large Hadron Collider: Harvest of Run 1* (T. Schörner-Sadenius, ed.), pp. 259–300, 2015.
- [22] <http://inspirehep.net/record/1103034/plots>. [Accessed: 28-06-2016].
- [23] <https://twiki.cern.ch/twiki/pub/AtlasProtected/FeynmanDiagrams>. [Accessed: 28-06-2016].
- [24] [https://atlas.web.cern.ch/Atlas/GROUPS/PHYSICS/CombinedSummaryPlots/TOP/singletop\\_allchanvsroots/singletop\\_allchanvsroots.pdf](https://atlas.web.cern.ch/Atlas/GROUPS/PHYSICS/CombinedSummaryPlots/TOP/singletop_allchanvsroots/singletop_allchanvsroots.pdf). [Accessed: 27-07-2016].
- [25] “Measurement of the Inclusive and Fiducial Cross-Section of Single Top-Quark  $t$ -Channel Events in  $pp$  Collisions at  $\sqrt{s} = 8$  TeV,” Tech. Rep. ATLAS-CONF-2014-007, CERN, Geneva, Mar 2014.
- [26] “Measurement of the inclusive cross-section of single top-quark  $t$ -channel production in  $pp$  collisions at  $\sqrt{s} = 13$  TeV,” Tech. Rep. ATLAS-CONF-2015-079, CERN, Geneva, Dec 2015.
- [27] “Comprehensive measurements of  $t$ -channel single top-quark production cross sections at  $\sqrt{s} = 7$  TeV with the ATLAS detector,” *Phys. Rev. D*, vol. 90, p. 112006, Dec 2014.
- [28] S. Chatrchyan *et al.*, “Measurement of the single-top-quark  $t$ -channel cross section in  $pp$  collisions at  $\sqrt{s} = 7$  TeV,” *JHEP*, vol. 12, p. 035, 2012.
- [29] V. Khachatryan *et al.*, “Measurement of the  $t$ -channel single-top-quark production cross section and of the  $|V_{tb}|$  CKM matrix element in  $pp$  collisions at  $\sqrt{s} = 8$  TeV,” *JHEP*, vol. 06, p. 090, 2014.
- [30] “Measurement of the inclusive cross section of single top quark production in the  $t$  channel at  $\sqrt{s} = 13$  TeV,” Tech. Rep. CMS-PAS-TOP-16-003, CERN, Geneva, 2016.

- 
- [31] G. Aad *et al.*, “Evidence for the associated production of a  $W$  boson and a top quark in ATLAS at  $\sqrt{s} = 7$  TeV,” *Phys. Lett.*, vol. B716, pp. 142–159, 2012.
- [32] G. Aad *et al.*, “Measurement of the production cross-section of a single top quark in association with a  $W$  boson at 8 TeV with the ATLAS experiment,” *JHEP*, vol. 01, p. 064, 2016.
- [33] S. Chatrchyan *et al.*, “Evidence for associated production of a single top quark and  $W$  boson in  $pp$  collisions at  $\sqrt{s} = 7$  TeV,” *Phys. Rev. Lett.*, vol. 110, p. 022003, 2013.
- [34] S. Chatrchyan *et al.*, “Observation of the associated production of a single top quark and a  $W$  boson in  $pp$  collisions at  $\sqrt{s} = 8$  TeV,” *Phys. Rev. Lett.*, vol. 112, no. 23, p. 231802, 2014.
- [35] “Combination of cross-section measurements for associated production of a single top-quark and a  $W$  boson at  $\sqrt{s} = 8$  TeV with the ATLAS and CMS experiments,” Tech. Rep. ATLAS-CONF-2016-023, CERN, Geneva, May 2016.
- [36] “Combination of cross-section measurements of associated production of a single top quark and a  $W$  boson at  $\sqrt{s} = 8$  TeV with the ATLAS and CMS experiments,” Tech. Rep. CMS-PAS-TOP-15-019, CERN, Geneva, 2016.
- [37] “Search for  $s$ -Channel Single Top-Quark Production in  $pp$  Collisions at  $\sqrt{s} = 7$  TeV,” Tech. Rep. ATLAS-CONF-2011-118, CERN, Geneva, Aug 2011.
- [38] “Evidence for single top-quark production in the  $s$ -channel in proton–proton collisions at  $\sqrt{s} = 8$  TeV with the ATLAS detector using the Matrix Element Method,” *Phys. Lett. B*, vol. 756, pp. 228–246. 16 p, Nov 2015.
- [39] V. Khachatryan *et al.*, “Search for  $s$  channel single top quark production in  $pp$  collisions at  $\sqrt{s} = 7$  and 8 TeV,” 2016.



- [40] “Fiducial  $t$  channel single top-quark cross section at 8 TeV,” Tech. Rep. CMS-PAS-TOP-15-007, CERN, Geneva, 2015.
- [41] Kidonakis, Nikolaos, “Next-to-next-to-leading-order collinear and soft gluon corrections for  $t$ -channel single top quark production,” *Phys. Rev. D*, vol. 83, p. 091503, May 2011.
- [42] Kidonakis, Nikolaos, “Two-loop soft anomalous dimensions for single top quark associated production with a  $W^-$  or  $H^-$ ,” *Phys. Rev. D*, vol. 82, p. 054018, Sep 2010.
- [43] Kidonakis, Nikolaos, “Next-to-next-to-leading logarithm resummation for  $s$ -channel single top quark production,” *Phys. Rev. D*, vol. 81, p. 054028, Mar 2010.
- [44] P. Kant, O. Kind, T. Kintscher, T. Lohse, T. Martini, S. Mölbitz, P. Rieck, and P. Uwer, “Hathor for single top-quark production: Updated predictions and uncertainty estimates for single top-quark production in hadronic collisions,” *Computer Physics Communications*, vol. 191, pp. 74 – 89, 2015.
- [45] R. Guedes, R. Santos, and M. Won, “Limits on strong flavor changing neutral current top couplings at the LHC,” *Phys. Rev.*, vol. D88, no. 11, p. 114011, 2013.
- [46] P. M. Ferreira and R. Santos, “Strong flavor changing effective operator contributions to single top quark production,” *Phys. Rev.*, vol. D73, p. 054025, 2006.
- [47] A. Amorim, J. P. Araque, N. F. Castro, J. Santiago, and R. Santos, “Production of  $t\gamma$ ,  $tZ$  and  $tH$  via Flavour Changing Neutral Currents,” *PoS*, vol. TOP2015, p. 067, 2016.
- [48] R. Coimbra, A. Onofre, R. Santos, and M. Won, “MEtop – a top FCNC event generator,” *J. Phys. Conf. Ser.*, vol. 447, p. 012031, 2013.

- 
- [49] C. Degrande, F. Maltoni, J. Wang, and C. Zhang, “Automatic computations at next-to-leading order in QCD for top-quark flavor-changing neutral processes,” *Phys. Rev.*, vol. D91, p. 034024, 2015.
- [50] J. A. Aguilar-Saavedra, “Top flavor-changing neutral interactions: Theoretical expectations and experimental detection,” *Acta Phys. Polon.*, vol. B35, pp. 2695–2710, 2004.
- [51] V. M. Abazov *et al.*, “Search for flavor changing neutral currents via quark-gluon couplings in single top quark production using  $2.3 \text{ fb}^{-1}$  of  $p\bar{p}$  collisions,” *Phys. Lett.*, vol. B693, pp. 81–87, 2010.
- [52] “Search for the flavor-changing neutral-current decay  $t \rightarrow Zq$  in  $p\bar{p}$  collisions at  $\sqrt{s}=1.96\text{TeV}$ ,” *Physical Review Letters*, vol. 101, 11 2008.
- [53] G. Aad *et al.*, “Search for single top-quark production via flavour-changing neutral currents at 8 TeV with the ATLAS detector,” *Eur. Phys. J.*, vol. C76, no. 2, p. 55, 2016.
- [54] V. Khachatryan *et al.*, “Search for anomalous single top quark production in association with a photon in pp collisions at  $\sqrt{s} = 8 \text{ TeV}$ ,” *JHEP*, vol. 04, p. 035, 2016.
- [55] G. Aad *et al.*, “Search for flavour-changing neutral current top-quark decays to  $qZ$  in  $pp$  collision data collected with the ATLAS detector at  $\sqrt{s} = 8 \text{ TeV}$ ,” *Eur. Phys. J.*, vol. C76, no. 1, p. 12, 2016.
- [56] “Search for Flavour Changing Neutral Currents in single top events,” Tech. Rep. CMS-PAS-TOP-12-021, CERN, Geneva, 2013.
- [57] S. Chatrchyan *et al.*, “Search for Flavor-Changing Neutral Currents in Top-Quark Decays  $tZq$  in  $pp$  Collisions at  $\sqrt{s} = 8 \text{ TeV}$ ,” *Phys. Rev. Lett.*, vol. 112, no. 17, p. 171802, 2014.

- [58] “Search for associated production of a Z boson with a single top quark and for tZ flavour-changing interactions in pp collisions at  $\sqrt{s} = 8$  TeV,” Tech. Rep. CMS-PAS-TOP-12-039, CERN, Geneva, 2016.
- [59] <https://atlas.web.cern.ch/Atlas/GROUPS/PHYSICS/CombinedSummaryPlots/TOP/>. [Accessed: 12-07-2016].
- [60] Lyndon Evans and Philip Bryant, “LHC Machine,” *Journal of Instrumentation*, vol. 3, no. 08, p. S08001, 2008.
- [61] The ATLAS Collaboration, “The ATLAS Experiment at the CERN Large Hadron Collider,” *Journal of Instrumentation*, vol. 3, no. 08, p. S08003, 2008.
- [62] <https://cds.cern.ch/record/2119882>. [Accessed: 17-06-2016].
- [63] F. J. Hasert *et al.*, “Observation of Neutrino Like Interactions Without Muon Or Electron in the Gargamelle Neutrino Experiment,” *Phys. Lett.*, vol. B46, pp. 138–140, 1973.
- [64] G. Arnison *et al.*, “Experimental Observation of Isolated Large Transverse Energy Electrons with Associated Missing Energy at  $\sqrt{s} = 540$ -GeV,” *Phys. Lett.*, vol. B122, pp. 103–116, 1983. [,611(1983)].
- [65] M. Banner *et al.*, “Observation of Single Isolated Electrons of High Transverse Momentum in Events with Missing Transverse Energy at the CERN anti-p p Collider,” *Phys. Lett.*, vol. B122, pp. 476–485, 1983.
- [66] S. Schael *et al.*, “Precision electroweak measurements on the Z resonance,” *Phys. Rept.*, vol. 427, pp. 257–454, 2006.
- [67] V. Fanti *et al.*, “A New measurement of direct CP violation in two pion decays of the neutral kaon,” *Phys. Lett.*, vol. B465, pp. 335–348, 1999.
- [68] G. Aad *et al.*, “Observation of a new particle in the search for the Standard Model Higgs boson with the ATLAS detector at the LHC,” *Phys. Lett.*, vol. B716, pp. 1–29, 2012.

- 
- [69] S. Chatrchyan *et al.*, “Observation of a new boson at a mass of 125 GeV with the CMS experiment at the LHC,” *Phys. Lett.*, vol. B716, pp. 30–61, 2012.
- [70] The ALICE Collaboration, “The ALICE experiment at the CERN LHC,” *Journal of Instrumentation*, vol. 3, no. 08, p. S08002, 2008.
- [71] The CMS Collaboration, “The CMS experiment at the CERN LHC,” *Journal of Instrumentation*, vol. 3, no. 08, p. S08004, 2008.
- [72] The LHCb Collaboration, “The LHCb Detector at the LHC,” *Journal of Instrumentation*, vol. 3, no. 08, p. S08005, 2008.
- [73] <https://cds.cern.ch/record/1095926>. [Accessed: 17-06-2016].
- [74] <https://cds.cern.ch/record/1095927>. [Accessed: 17-06-2016].
- [75] <http://cds.cern.ch/record/1095929>. [Accessed: 17-06-2016].
- [76] [https://twiki.cern.ch/twiki/bin/view/AtlasPublic/LuminosityPublicResultsRun2#Luminosity\\_summary\\_plots\\_for\\_AN1](https://twiki.cern.ch/twiki/bin/view/AtlasPublic/LuminosityPublicResultsRun2#Luminosity_summary_plots_for_AN1). [Accessed: 07-07-2016].
- [77] G. Duckeck, D. Barberis, R. Hawkings, R. Jones, N. McCubbin, G. Poulard, D. Quarrie, T. Wenaus, and E. Obreshkov, “ATLAS computing: Technical design report,” 2005.
- [78] <http://wlcg-public.web.cern.ch/tier-centres>. [Accessed: 10-07-2016].
- [79] J.-L. Agram, J. Andrea, E. Conte, B. Fuks, D. Gelé, and P. Lansonneur, “Probing top anomalous couplings at the LHC with trilepton signatures in the single top mode,” *Phys. Lett.*, vol. B725, pp. 123–126, 2013.
- [80] <https://ms2.physik.hu-berlin.de/~atlas/aplusplus/html/doc/>. A++ Reference Guide.

- [81] “2015 start-up trigger menu and initial performance assessment of the ATLAS trigger using Run-2 data,” Tech. Rep. ATL-DAQ-PUB-2016-001, CERN, Geneva, Mar 2016.
- [82] “Performance of the ATLAS muon trigger in 2011,” Tech. Rep. ATLAS-CONF-2012-099, CERN, Geneva, Jul 2012.
- [83] “Electron efficiency measurements with the ATLAS detector using the 2015 LHC proton-proton collision data,” Jun 2016.
- [84] “Muon reconstruction performance of the ATLAS detector in proton-proton collision data at 13 TeV,” *Eur. Phys. J. C*, vol. 76, p. 292. 45 p, Mar 2016.
- [85] M. Cacciari, G. P. Salam, and G. Soyez, “The Anti-k(t) jet clustering algorithm,” *JHEP*, vol. 04, p. 063, 2008.
- [86] M. Cacciari and G. P. Salam, “Dispelling the  $N^3$  myth for the  $k_t$  jet-finder,” *Phys. Lett.*, vol. B641, pp. 57–61, 2006.
- [87] M. Cacciari, G. P. Salam, and G. Soyez, “FastJet user manual,” *Eur. Phys. J. C*, vol. 72, p. 1896. 69 p, Nov 2011.
- [88] T. Barillari, E. Bergeaas Kuutmann, T. Carli, J. Erdmann, P. Giovannini, K. J. Grahn, C. Issever, A. Jantsch, A. Kiryunin, K. Lohwasser, A. Maslennikov, S. Menke, H. Oberlack, G. Pospelov, E. Rauter, P. Schacht, F. Spanó, P. Speckmayer, P. Stavina, and P. Strízenec, “Local Hadronic Calibration,” Tech. Rep. ATL-LARG-PUB-2009-001-2. ATL-COM-LARG-2008-006. ATL-LARG-PUB-2009-001, CERN, Geneva, Jun 2008. Due to a report-number conflict with another document, the report-number ATL-LARG-PUB-2009-001-2 has been assigned.
- [89] “Monte Carlo Calibration and Combination of In-situ Measurements of Jet Energy Scale, Jet Energy Resolution and Jet Mass in ATLAS,” Tech. Rep. ATLAS-CONF-2015-037, CERN, Geneva, Aug 2015.

- 
- [90] “Jet Calibration and Systematic Uncertainties for Jets Reconstructed in the ATLAS Detector at  $\sqrt{s} = 13$  TeV,” Tech. Rep. ATL-PHYS-PUB-2015-015, CERN, Geneva, Jul 2015.
- [91] “Expected performance of the ATLAS  $b$ -tagging algorithms in Run-2,” Tech. Rep. ATL-PHYS-PUB-2015-022, CERN, Geneva, Jul 2015.
- [92] [https://atlas.web.cern.ch/Atlas/GROUPS/PHYSICS/PUBNOTES/ATL-PHYS-PUB-2015-022/figaux\\_02a.png](https://atlas.web.cern.ch/Atlas/GROUPS/PHYSICS/PUBNOTES/ATL-PHYS-PUB-2015-022/figaux_02a.png). [Accessed: 02-08-2016].
- [93] [https://atlas.web.cern.ch/Atlas/GROUPS/PHYSICS/PUBNOTES/ATL-PHYS-PUB-2015-022/figaux\\_02b.png](https://atlas.web.cern.ch/Atlas/GROUPS/PHYSICS/PUBNOTES/ATL-PHYS-PUB-2015-022/figaux_02b.png). [Accessed: 02-08-2016].
- [94] J. Alwall, M. Herquet, F. Maltoni, O. Mattelaer, and T. Stelzer, “MadGraph 5 : Going Beyond,” *JHEP*, vol. 06, p. 128, 2011.
- [95] T. Sjostrand, S. Mrenna, and P. Z. Skands, “PYTHIA 6.4 Physics and Manual,” *JHEP*, vol. 05, p. 026, 2006.
- [96] Stefano Frixione and Paolo Nason and Carlo Oleari, “Matching NLO QCD computations with parton shower simulations: the POWHEG method,” *Journal of High Energy Physics*, vol. 2007, no. 11, p. 070, 2007.
- [97] “Jet Calibration and Systematic Uncertainties for Jets Reconstructed in the ATLAS Detector at  $\sqrt{s} = 13$  TeV,” Tech. Rep. ATL-PHYS-PUB-2015-015, CERN, Geneva, Jul 2015.
- [98] T. Junk, “Confidence level computation for combining searches with small statistics,” *Nucl. Instrum. Meth.*, vol. A434, pp. 435–443, 1999.
- [99] A. L. Read, “Presentation of search results: The CL(s) technique,” *J. Phys.*, vol. G28, pp. 2693–2704, 2002. [,11(2002)].
- [100] <https://atlas.web.cern.ch/Atlas/GROUPS/DATAPREPARATION/PublicPlots/2016/DataSummary/figs/intlumivsyyear.png>. [Accessed: 20-08-2016].